A STUDY OF FORMATION AND DISSOCIATION OF GAS HYDRATE

A Thesis

by

SADEGH BADAKHSHAN RAZ

Submitted to the Office of Graduate Studies of
Texas A&M University
in partial fulfillment of the requirements for the degree of

MASTER OF SCIENCE

May 2012

Major Subject: Petroleum Engineering

The Study of Formation and Dissociation of Gas Hydrate

A STUDY OF FORMATION AND DISSOCIATION OF GAS HYDRATE

A Thesis

by

SADEGH BADAKHSHAN RAZ

Submitted to the Office of Graduate Studies of
Texas A&M University
in partial fulfillment of the requirements for the degree of

MASTER OF SCIENCE

Approved by:

Chair of Committee,	Ahmad Ghassemi
Committee Members,	Walter Ayers
	Mahmoud El-Halwagi
Head of Department,	A. Daniel Hill

May 2012

Major Subject: Petroleum Engineering

ABSTRACT

A Study of Formation and Dissociation of Gas Hydrate.

(May 2012)

Sadegh Badakhshan Raz, B.S., Sahand University of Technology,

M.S., Sharif University of Technology

Chair of Advisory Committee: Dr. Ahmad Ghassemi

The estimation of gas hydrate volume in closed systems such as pipelines during shut-in time has a great industrial importance. A method is presented to estimate the volume of formed or decomposed gas hydrate in closed systems. The method was used to estimate the volume of formed gas hydrate in a gas hydrate crystallizer under different subcoolings of 0.2, 0.3, 0.6 and 4.6°C, and initial pressures of 2000 and 2500 psi. The rate of gas hydrate formation increased with increases in subcooling and initial pressure. The aim of the second part of the study was the evaluation of the formation of gas hydrate and ice phases in a super-cooled methane-water system under the cooling rates of 0.45 and 0.6°C/min, and the initial pressures of 1500, 2000 and 2500 psi, in pure and standard sea water-methane gas systems. The high cooling rate conditions are likely to be present in pipelines or around a wellbore producing from gas hydrate reservoir. Results showed that the initial pressure and the chemical composition of the water had little effect on the ice and gas hydrate formation temperatures, which were in the range

of -8±0.2°C in all the tests using the cooling rate of 0.45 °C/min. In contrast, the increase in the cooling rate from 0.45 to 0.6°C/min decreased the ice and gas hydrate formation temperatures from -8°C to -9°C. In all tests, ice formed immediately after the formation of gas hydrate with a time lag less than 2 seconds. Finally, an analytical solution was derived for estimating induced radial and tangential stresses around a wellbore in a gas hydrate reservoir during gas production. Gas production rates between 0.04 to 0.12 Kg of gas per second and production times between 0.33 to 8 years were considered. Increases in production time and production rate induced greater radial and tangential stresses around the wellbore.

DEDICATION

To my wife, Maryam Rajab Boloukat, for all of her sacrifices and kind help, my new born Angel, Mina Badakhshan Raz, for giving me a whole new direction in life and to my parents, Habib Badakhshan Raz and Batoul Hassan, for all of their dedication and sacrifices.

ACKNOWLEDGEMENTS

I would like to thank my committee chair, Dr. Ahmad Ghassemi, for his guidance and support throughout the course of this research and my committee members, Professor Walter Ayers and Professor Mahmoud EL-Halwagi, for their help.

I also thank Professor Yuri Makogon for his help during my experiments at Texas A&M University. Finally, I appreciate my dear wife Maryam Rajab Boloukat for her patience, support and love.

TABLE OF CONTENTS

Page

LIST OF FIGURES

Page

LIST OF TABLES

Page

1. INTRODUCTION

Gas hydrates are metastable crystalline materials consisting of one or more types of gas molecules inside a molecular cage made out of hydrogen bonded water molecules. Gas hydrates are considered clatherate substances. Clatherate comes from the Latin word *clathratus* which means encaged [1]. The term clatherate is used for materials like methane hydrate in which a host molecule like water surrounds a guest molecule like methane. The stability of gas hydrates is affected by parameters such as temperature, pressure, gas composition and even external electrical fields [2, 3].

The gas hydrates form because of the existence of hydrogen bonds between water molecules as well as Vander Waals' forces between water and gas molecules [1]. The existence of hydrogen bonds gives unusual behaviors, such as expansion during formation, to both ice and gas hydrates. The difference between gas hydrate and ice is that the ice forms from water in contrast to gas hydrate, which needs dissolved gas molecules in water in order to form [1].

The most common form of ice crystalline structure is hexagonal structure [1]. In ice structure, each water molecule is hydrogen bonded to four other water molecules. These five water molecules form a tetrahedron in which oxygen atoms position on the vertices of the tetrahedron with angle of 109.5˚. The position of water molecules in tetrahedron structure is shown in Fig. 1. The typical distance between oxygen nuclei in a tetrahedron's structure is 2.76 °A [4].

This thesis follows the style of Fuel.

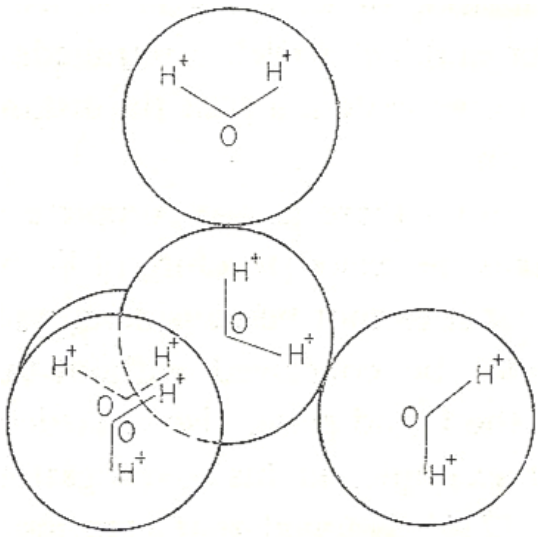

Fig. 1 Tetrahedron forms from water molecules in ice crystalline structure [4].

The most common types of gas hydrate crystalline structures are:

- **Structure I:** The structure is cubic in which the size of guest gas molecules is between 4.2˚A to 6˚A. The examples of these molecules are methane, ethane, hydrogen sulfide, and carbon dioxide [1].
- **Structure II:** The crystalline structure is cubic and forms from gas molecules with smaller or bigger sizes than the molecules which form structure I. For example, the structure could form from small gas molecules like hydrogen and nitrogen with sizes less than 4.2 ˚A or molecules such as propane and iso-butane with the size of 6˚A to 7˚A [1].
- **Structure H:** The structure is hexagonal, and the guest molecules have a size in the range of 7˚A to 9˚A. The examples of guest molecules are iso-pentane and neo-hexane (2, 2-dimethylbutane) [1].

The typical structure of a gas hydrate cage with a guest molecule is shown in Fig. 2.

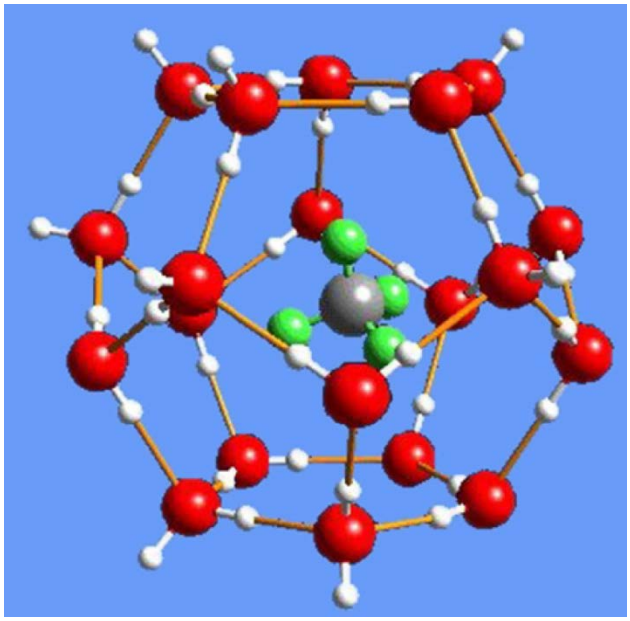

Fig. 2 The typical atomic structure of gas hydrate. The methane gas is inside the cage created by hydrogen bonded water molecules [5]

The space created by hydrogen bonded water molecules which accommodates the gas molecules in gas hydrate atomic lattice is called a cavity. Cavities in gas hydrates are in the shape of polyhedrons with different types of faces. Jefrry [6] suggested the nomenclature description of m^n for the representation of cavity types in a gas hydrate structure. In this representation, *m* is the number of edges in a particular polyhedron face and *n* is the number of that particular face in the polyhedron cavity. For example, the cavity type of 5^{12} means that the cavity consists of 12 pentagonal faces with equal edge lengths and equal angles. Similarly, the cavity $5^{12}6^2$ has 14 faces including 12

pentagonal and 2 hexagonal faces. Some common types of gas hydrate cavities are shown in Fig. 3.

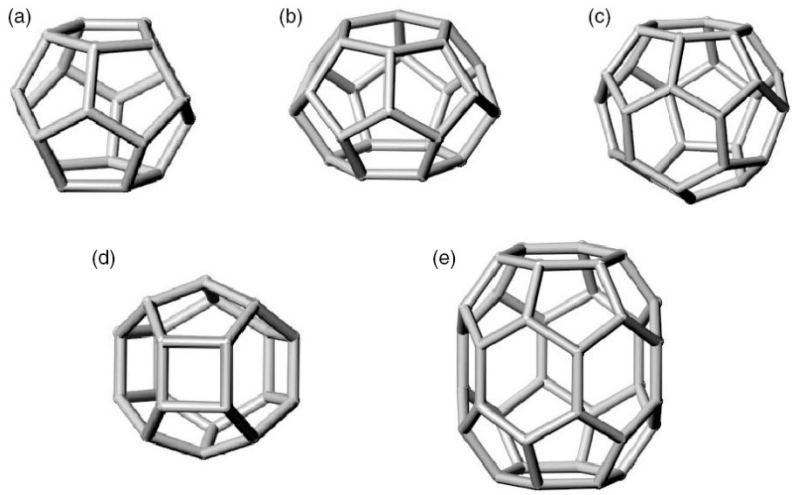

Fig. 3 Different types of cavities in gas hydrates structure, (a) pentagonal docehedron (5^{12}), (b) tetrakaidecahedron, ($5^{12}6^2$), (c) hexakaidecahedron ($5^{12}6^4$), (d) irregular docehedron ($4^3 5^6 6^3$) and (e) icosahedrons ($5^{12}6^8$) [1].

1.1. Gas Hydrates Resources in Nature

Gas hydrate deposits on earth are the biggest untapped resources of energy in the world. The estimated amount of organic carbon in the form of gas hydrate in the earth is 10,000 giga tones which contains 100,000 to 300,000,000 trillion cubic feet (Tcf) of gas [5, 7]. The significance of gas hydrate resources will be recognized when it is considered that the total amount of non-hydrate gas reserves in the world is just 13,000 Tcf [5]. In nature, gas hydrate forms in sedimentary rocks that are saturated with gas and water and maintain a suitable low temperature and high pressure conditions, which make the

formation of hydrate thermodynamically feasible. The deposits of gas hydrate in nature are located in permafrost and oceanic regions.

The permafrost is the area on earth where the ground temperature is zero or below zero degrees centigrade. Gas hydrate deposits in those areas occur in or below permafrost layers. The presence of gas flow from lower strata, low temperatures, and high pressure conditions in permafrost make it an ideal place for formation of gas hydrate. Currently, permafrost covers 34.5 million km^2 or 23% of total land on earth. For example, permafrost covers 100% of the South Pole, 75% of Alaska, 63% of Canada, and 62% of Russia [2, 3]. Current permafrost regions are shown in Fig. 4.

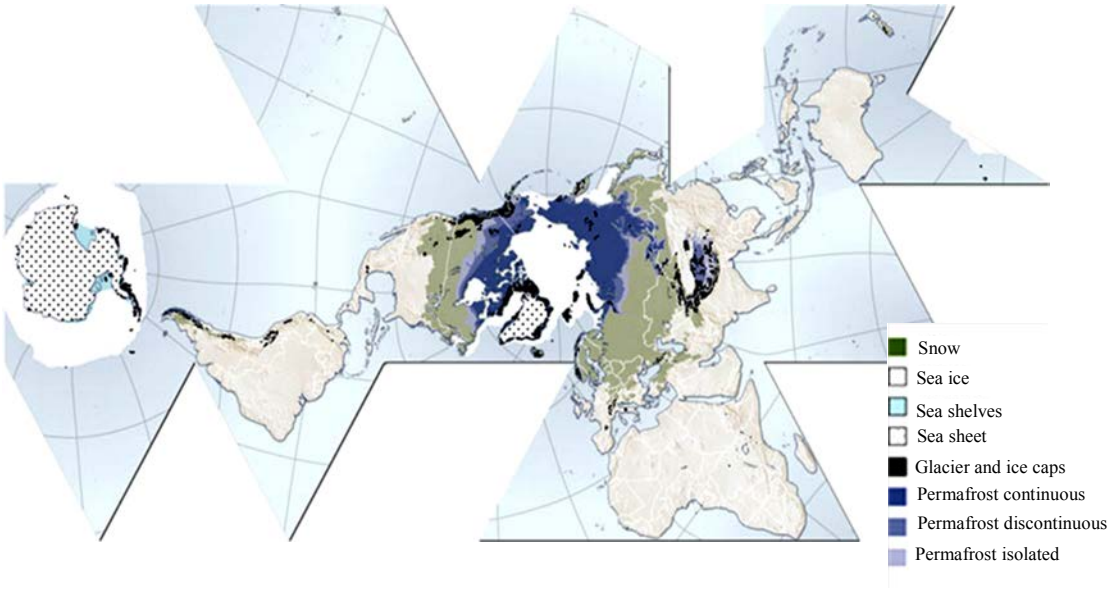

Fig. 4. Map of current permafrost regions of the earth [8].

The main factor that affects the formation of gas hydrates in land is the ground surface temperature. Because of the natural geothermal gradient, the temperature tends to increase with depth. With an increase of temperature beyond the gas hydrate stability envelope, the gas hydrate compounds become thermodynamically unstable and start to decompose. The depth at which the temperature exceeds the equilibrium temperature of gas hydrate formation is called the base of the gas hydrate stability zone. Consequently, gas hydrates do not form in areas of earth where permafrost is absent or very limited.

Gas hydrates may form in unconsolidated or semi-consolidated oceanic sediments. The majority of known gas hydrate resources are found in oceanic environments since the area of the earth covered by oceans is much greater than the area covered by permafrost. The oceanic gas hydrate is the most important potential energy resource, especially for those countries with poor conventional hydrocarbon resources like Japan and South Korea. A map of some proved or inferred resources of oceanic gas hydrate near the continental margin is shown in Fig. 5.

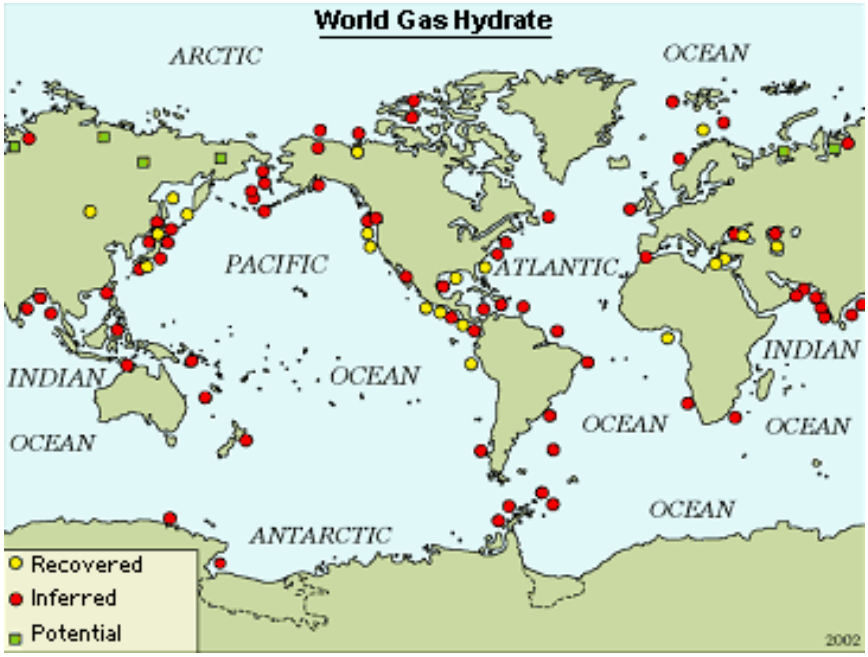

Fig. 5 Map of oceanic gas hydrate distribution near continental margin [9].

Similar to conditions in permafrost, the thermal gradients in both ocean water and sediments below the ocean floor play a very important role in the formation of gas hydrates in an oceanic environment. With increase in water depth, the water temperature decreases. Low temperature conditions on the sea floor in places where water depth is greater than 500 m create an appropriate thermal condition for gas hydrate formation [10]. With increasing depth below the sea floor, the temperature increases due to the geothermal gradient to the point that gas hydrates are not thermodynamically stable. This point will be the base of the gas hydrate stability zone.

1.2. Research Objectives

Three different subjects were studied in the current research. The research objective in the first part was the introduction of an efficient and accurate technique for calculating the volume of formed or decomposed gas hydrate in a closed system according to pressure and temperature data. The estimation of gas hydrate volume has great importance in flow assurance and industrial production of gas hydrates for gas storage and transportation purposes. In the second part of the research, the goal was the study of the formation of gas hydrates and ice phases under high cooling rate conditions to assess the effect of different parameters on the ice and gas hydrate formation temperatures.

Formation of gas hydrates and ice around a producing well is an issue in gas production from gas hydrate reservoirs. Rapid cooling rates due to the Joule-Thompson effect induced by high production rates cause formation of gas hydrates and ice around the wellbore which decreases or terminates gas production from the reservoir. In this part of the research, the formation of ice and gas hydrate phases under different initial pressures, cooling rates and water chemical compositions are studied.

Finally, in the last section of the research, the objective was the calculation of the amount of induced stress around a production well in a gas hydrate reservoir. The estimation of the induced stress around a producing well is a very important step in wellbore stability evaluation in gas hydrate reservoirs.

2. VOLUMETRIC CALCULATION OF FORMED OR DECOMPOSED GAS HYDRATE IN A BATCH CRYSTALLIZER

2.1. Introduction

The study of gas hydrate formation and decomposition under different temperature and pressure conditions has great technical importance in the oil and gas industry. The assessment of formation conditions of gas hydrate plugs in gas pipelines and secondary formation of gas hydrates near wellbores during gas production from gas hydrate-bearing reservoirs are examples with high industrial importance in which gas hydrate formation plays a main role. In scientific research, the calculation of the amount of gas that is consumed or generated during gas hydrate formation or decomposition is the basis of gas hydrate kinetic studies.

As mentioned by Darabonia *et al.* [11], the semi-batch stirrer crystallizer, introduced by Vysniauskas and Bishnoi [12] and latter modified by Bishnoi and his colleagues [13, 14], is commonly used in many kinetic studies [15, 16, 17, 18] and is a favorable setup in the oil and gas industry. The setup includes a semi-batch stirred tank reactor which is connected to pressure reservoirs of variable volumes for providing gas flow during experiments. The system also comprises different control flow valves to control the gas flow rates for providing the isobaric conditions. As pointed out by Englezos *et al.* [13], in gas hydrate kinetic experiments; the limited variation of pressure has a negligible effect on the calculated kinetic parameter. Therefore, the isobaric condition is not a necessity during gas hydrate kinetic experiments. Furthermore, the experiments that aimed to mimic practical situations like the formation of gas hydrates in

shut-in pipelines have to be done in non-isobaric conditions. The accessories like control flow valves and variable-volume reservoirs in the system designed by Bishnoi's group make the system more costly and more vulnerable to operational problems like gas leakage.

The current experimental setup and procedure designed by Makogon in the Department of Petroleum Engineering at Texas A&M University has eliminated all of the flow control systems as well as additional variable volume reservoirs. The cell needs a gas cylinder for providing the gas and pressurizing the system and a Ruska pump for fine adjustment of the pressure. According to the method that is explained in the following section, the moles of consumed gas as well as the volume of formed or dissociated gas hydrate were calculated in the cell based solely on the recorded temperature and pressure of the cell during experiments. The method described here could also be used for real-time monitoring of the volume of formed gas hydrate in the industrial size crystallizers.

The method is based on experimentally observed approximate linearity of change in pressure versus temperature during constant-rate cooling or heating of a water-gas system in the absence of gas hydrate formation or dissociation. Considering the negligible effect of small variations in the pressure on the intrinsic kinetic parameters of gas hydrate formation or decomposition [13], the method can be used in kinetic studies of gas hydrate formation and decomposition under isothermal conditions. The method also can be used in gas hydrate experiments under both static and dynamic conditions.

In the current study, the experimental data on the measurement of gas hydrate volume were obtained for a pure methane-pure water system. Subcooling temperatures from 0.2 to 4.6 $^{\circ}$C and initial pressures of 2000 and 2500 psi were used to form the gas hydrate. The pressure range was selected according to the maximum pressure capabilities in the laboratory. Also, it has been observed experimentally that whiskery gas hydrate could form at high cooling rates [3]. Therefore, the subcooling was chosen in a way to prevent whiskery gas hydrate formation. The crystallizer cell was maintained in an isothermal condition after the start of gas hydrate formation for a period of time with controlling the temperature using a refrigerator controller. The temperature of the system was then increased to a temperature above that of the equilibrium of gas hydrate formation to superheat the system for complete gas hydrate decomposition. The effect of different subcooling temperatures on the volume of the gas hydrate is also discussed. Because the method is a basis for the kinetic study of gas hydrate formation and decomposition, the kinetics of gas hydrates is explained in Appendix A.

2.2. Theoretical Method for Calculation of Gas Hydrate Volume

The basis of the current method used for the calculation of consumed or generated moles of gas during the formation or decomposition of gas hydrate lies in the experimentally observed phenomenon that under constant cooling rates, pressure changes approximately linearly versus temperature when there is no gas hydrate forming in the system.

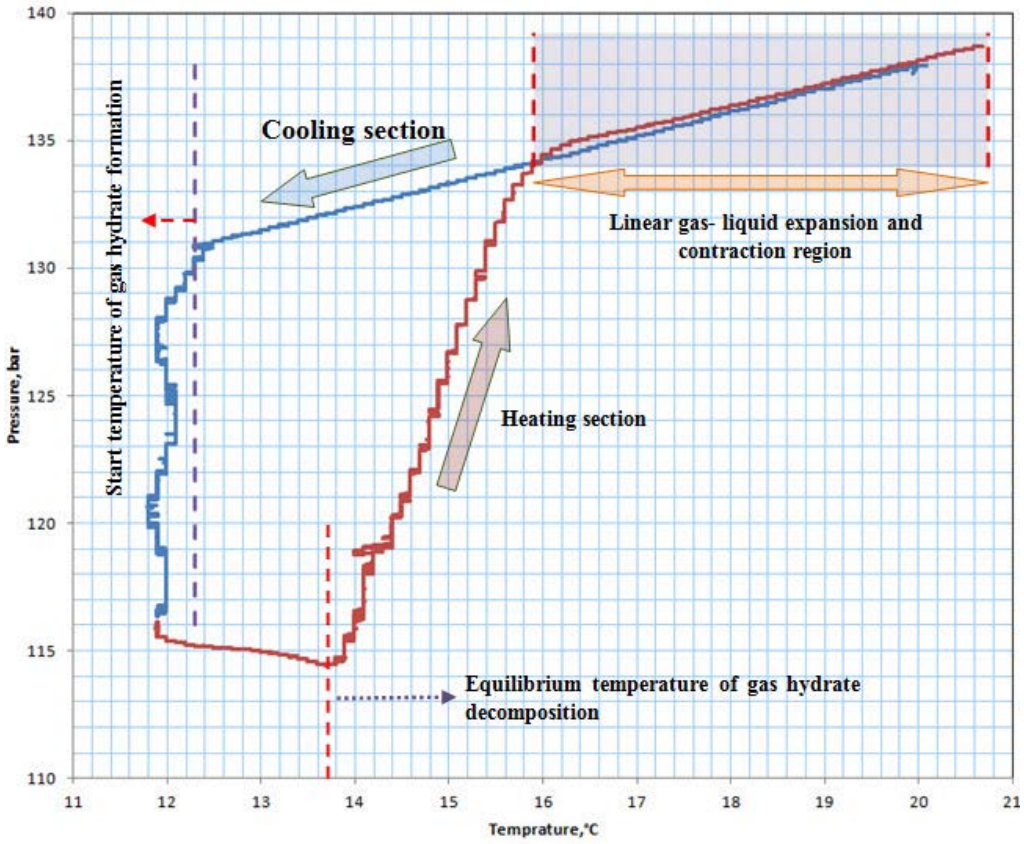

Fig. 6 Pressure-temperature curves for gas hydrate formation and decomposition.

This behavior is explained by the fact that without release or absorption of heat related to the formation or dissociation of gas hydrates, the system only experiences gas contraction or expansion during cooling or heating processes. The experimental results of gas hydrate formation and decomposition in a pure methane-pure water system (Fig. 5) show that the pressure versus temperature curve is approximately linear because it is solely related to gas expansion or contraction in the cell. For calculation of the volume of gas hydrate formed during the gas hydrate formation experiment, one needs to use the recorded pressure and temperature data acquired by the data acquisition system. For

calculation of the amount of gas consumed during gas hydrate formation, it is necessary to consider the pressure conditions of gas in the following two states:

- Line of real gas contraction or expansion without formation of gas hydrate.
- Real experimental data.

A schematic of a typical pressure-temperature curve during gas hydrate formation is shown in Fig. 6. For calculation of pressure along a hypothetical line, we need to use the equation of state for real gases at a given temperature T:

$$P = P_1 * \frac{V_i}{V} * \frac{n}{n_i} * \frac{Z}{Z_i} \tag{2.1}$$

where P is pressure in MPa and V, Z and n are gas volume, gas compressibility factor and the amount of methane gas gr-mole in the cell at the pressure P and temperature T. Also, P_i, V_i, Z_i and n_i are pressure, temperature, compressibility factor, and moles of gas in the chamber at the of the test, respectively. The gas under consideration is in a partially water-filed chamber. But since the solubility of gases like methane is very low in water (for example the solubility of methane in pure water is 0.000238 in molar fraction at 298.13K [19]), we assume that the number of moles of gas in the gas phase remains constant during the cooling and heating cycles. Therefore:

$$n = n_i \tag{2.2}$$

n_i could be calculated according to following relationship:

$$n_i = \frac{P_i V_i}{R T_i Z_i} \tag{2.3}$$

where R is the universal gas constant and is equal to 8.314472 $\frac{\text{MPa.cm}^3}{\text{mole.K}}$.

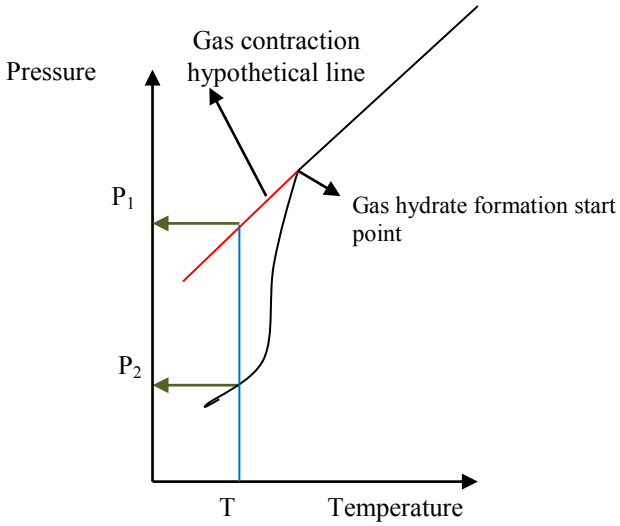

Fig. 7 Schematic of the experimental curve achieved in gas hydrate formation tests (black curve) and extrapolation of gas contraction line (red line).

After the formation of the gas hydrate (Fig. 5), the P-T curve deviates from a straight line due to gas consumption during gas hydrate formation. To calculate the volume of gas consumed at any given temperature, one needs to calculate the compressibility factor and the volume of gas at the standard condition. The lab temperature was around 21°C and the pressure at lab was around 1 atm. The temperature and pressure at the standard condition for gases are [20]:

- $T_{sc} = 0\ ^{\circ}C = 273.15\ K$
- $P_{sc} = 1\ atm = 1.01325\ bar$

The standard volume of gas is calculated under the following two conditions:

1. The number of moles of gas at standard condition, V_{sc1}, at any pressure (P_1) along the hypothetical contraction line (Fig. 6) occurs at the corresponding temperature T, shown.
2. The number of moles of gas (gas volume) at standard condition, V_{sc2}, hydrate forming experimental pressure (P_2) corresponds to temperature T.

The difference of these two volumes is the volume of consumed gas at the standard condition. Therefore, we have:

$$\Delta V_{g,sc} = V_{sc1} - V_{sc2} = V_1 * \frac{T_{sc}}{T} * \frac{P_1}{P_{sc}} * \frac{1}{Z_1} - V_2 * \frac{T_{sc}}{T} * \frac{P_2}{P_{sc}} * \frac{1}{Z_2} \quad (2.4)$$

Considering the value of T_{sc} in K and P_{sc} in bar, we obtain the following relationship.

$$\Delta V_{g,sc} = \frac{269.58}{T} * (\frac{V_1 * P_1}{Z_1} - \frac{V_2 * P_2}{Z_2}) \quad (2.5)$$

Where volumes V_1, V_2 and $\Delta V_{g,sc}$ are in cm^3, pressures P_1 and P_2 are in bar and temperature T is in K. Since, the expansion coefficient of fluids like water is very low and on the order of 10^{-4}, the change in water volume due to decrease in temperature is negligible. Therefore, we could consider the volume of water as well as the volume of gas constant during the test. So we will have:

$$V_1 = V_2 = V_{g,i} = V_{cell} - V_{w,i} \quad (2.6)$$

where $V_{g,i}$ is initial volume of gas in cm^3. So the formula (2.5) changes to:

$$\Delta V_{g,sc} = \frac{269.58 * V_{g,i}}{T} * (\frac{P_1}{Z_1} - \frac{P_2}{Z_2}) \quad (2.7)$$

The consumed moles of methane gas in the standard condition are (volume of 1 mole of gas at standard condition is 22414 cm^3):

$$n_{consumed} = \frac{\Delta V_{g,sc}}{22414} \tag{2.8}$$

Now, we can calculate the volume of the formed gas hydrate, with the assumption that the structure is type I, according to the following formula [21]

$$V_h = 0.000804 * \frac{N * \Delta V_{g,sc}}{\rho_h} \tag{2.9}$$

where V_h is the volume of formed gas hydrate in cm^3, N is the ratio of the number of water molecules to the number of gas molecules in gas hydrate unit cell, ρ_h is the gas hydrate density in $\frac{gr}{cm^3}$ and $\Delta V_{g,sc}$ is the volume of consumed gas in cm^3. From formulas (2.7) and (2.9), we will get:

$$V_h = 0.2167 \frac{N * V_{g,i}}{\rho_h * T} * (\frac{P_1}{Z_1} - \frac{P_2}{Z_2}) \tag{2.10}$$

Now, we need to calculate parameters N, z and ρ_h to get the volume of gas hydrate. For the calculation of parameter N, the gas hydrate structure is considered to be type I with 6 large cavities of $5^{12}6^2$ and 2 smaller cavities of 5^{12} in each unit cell. Each unit cell also contains 46 molecules of water [1]. Considering each cavity contains just one gas molecule, the ratio of the number of water molecules to the number of gas molecules in the gas hydrate unit cell, in the ideal case, with full occupancy would be:

$$N_{ideal} = \frac{46}{2+6} = 5.75 \tag{2.11}$$

However, in real conditions, there are always some cavities that contain no gas molecules and, therefore, the real N parameter is less than 5.75. In this case, N can be calculated according to the following formula [1, 21]

$$N = \frac{46}{2 * \theta_1 + 6 * \theta_2} \tag{2.12}$$

where θ_1 and θ_2 are the occupancy fraction of cavities type I and type II respectively. θ_i can be calculated by Langmuir adsorption relationship [22].

$$\theta_i = \frac{C_i \times f_i}{1 + \sum_{i=1}^{n} C_i \times f_i} \tag{2.13}$$

C_i is the Langmuir constant of guest molecule I in 1/bar. The following correlation [23] is used for the calculation of the Langmuir constant

$$C_i = 10^5 Exp(A + \frac{B}{T}) \tag{2.14}$$

where A and B are constants for methane hydrate and are given in Table 1.

Table 1 The parameters of Eq. (2.14) [23]

Parameter	Small cage	Large Cage
A	-24.027993	-22.683049
B	3134.7529	3080.3857

Also, f_i is the fugacity of gas molecule i in the gas hydrate phase in bar. In equilibrium, the fugacities of gas in all phases are equal and, therefore, the fugacity of gas in the gas hydrate lattice is equal to the fugacity of the gas molecule in the gas phase. In the case of methane hydrate, the vapor pressure of water in the gas phase is very low and, therefore, it could be assumed that the fugacity of methane in the gas phase is equal

to the fugacity of pure methane at same pressure and temperature conditions [24, 25]. The fugacity of pure methane is calculated by Duan's equation of state [26].

According to the definition of density, the density of gas hydrate can be defined as the ratio of mass in 1 mole of the unit cells of gas hydrate to 6.023×10^{23} times the volume of gas hydrate unit cell. Therefore, it could be written [1]:

$$\rho_h = \frac{46 * MW_{water} + (2 * \theta_1 + 6 * \theta_2) * MW_{gas}}{6.023 * 10^{23} * V_{unit\ cell}} \tag{2.15}$$

where $V_{\text{unit cell}}$ is the volume of one unit cell of gas hydrate in cm^3. If the type of former gas is methane, the type of gas hydrate crystal would be type I and the volume of a unit cell is equal to 1728×10^{-24} cm^3[1]. Considering the molecular weight of methane and water and after simplification of above relationship, the density is equal to:

$$\rho_h = 0.7956 + 0.03075 * \theta_1 + 0.0922 * \theta_2 \tag{2.16}$$

For the calculation of gas compressibility factor, the critical pressure and temperature of gas need to be calculated according to its chemical composition or its specific gravity. For this calculation, the method of Piper *et al.* [27] was used. For the calculation of gas compressibility factor through a non-iterative method, the method introduced by Batzle and Wang is used [28]. This method of the calculation of volume of formed gas hydrate was originally introduced by Makogon [2] with this assumption that gas compressibility factor is the same in the hypothetical line and experimental curve at any given temperature. In this research, this assumption is relaxed and a computer code was written to calculate the moles of consumed or generated gas as well as the volume of gas hydrate.

2.2.1. Correlation for Prediction of Gas Hydrate Equilibria

For the prediction of gas hydrate equilibrium formation pressures and temperatures, the method introduced by Ostergaad *et al.* [29] was used. According to the method, the equilibrium gas hydrate pressure at a given temperature for a system of pure water and different hydrocarbon gases is:

$$P = exp([c_1(\gamma + c_2)^{-3} + c_3F_m + c_4F_m^2 + c_5] * T + c_6(\gamma + c_7)^{-3} + c_8F_m + c_9F_m^2 + c_{10} \quad (2.17)$$

where P is gas hydrate equilibrium formation pressure in kPa, T is temperature in K, γ is the gas specific gravity of hydrate forming hydrocarbons and F_m is defined according to the following formula

$$F_m = \frac{f_{nh}}{f_h} \quad (2.18)$$

where f_h is the total molecular weight of hydrate forming hydrocarbons in the gas mixture, including methane, ethane, propane and butanes. Also, f_{nh} is the total molecular weight of non hydrate forming hydrocarbons in the gas mixture. The constants c_1 to c_{10} are mentioned in Table 2.

Table 2 The parameters used in formula (2.17) [29, 30]

Constant	Value
c_1	4.5134×10^{-3}
c_2	0.46852
c_3	$2.\ 18636\times10^{-2}$
c_4	$-8.\ 417\times10^{-4}$
c_5	0.129622
c_6	$3.\ 6625\times10^{-4}$
c_7	-0.485054
c_8	-5.44376
c_9	$3.\ 89\times10^{-3}$
c_{10}	-29.9351

2.2.2. The Effect of Salts on Gas Hydrate Equilibrium Pressure

The presence of salts in solution causes shift in equilibrium pressures and temperatures. For the calculation of this shift, the concept of NaCl equivalent weight percent was used [31, 32]. The procedure for the calculation of NaCl equivalent weight percent is discussed in references 84 and 85. After the calculation of NaCl equivalent, the shift in gas hydrate equilibrium temperature could be calculated according to the following formula [31].

$$\Delta T = (c1W + c2W2 + c3W3) \times (c4\,Ln(P) + c5) \times (c6\,(P0 - 1000) + 1) \quad (2.19)$$

where W is NaCl equivalent weight percent, P is pressure in KPa and P_0 is the equilibrium pressure of gas hydrate formation for a water-gas system without any salt. Also the coefficients C_1 to C_6 are given in Table 3.

Table 3 The constants of formula (2.19) [31]

Constant	Value
c_1	3.534×10^{-1}
c_2	1.375×10^{-3}
c_3	2.433×10^{-4}
c_4	4.056×10^{-4}
c_5	7.994×10^{-1}
c_6	2.250×10^{-5}

2.2.3. Gas Hydrate Formation below Ice Formation Temperature

Formation of gas hydrate below and above zero degree centigrade does not follow the same formation pattern because of the potential for ice formation in subzero temperatures. A model proposed by Østergaard and Tohidi [33] accounts for formation of ice which happens after the formation of gas hydrate. According to the model, the equilibrium formation pressures of gas hydrate below zero degrees centigrade obey following power law expression.

$$P = aT^b \tag{2.20}$$

where P is gas hydrate equilibrium formation pressure in kPa and T is temperature in K. Also a and b are constants given by the following formula.

$$a = a_0 \times exp(a_1 \times p_0) \tag{2.21}$$

where $a_0 = 5.0715\times10^{-28}$, $a_1 = 3.8207\times10^{-3}$ and p_0 is the equilibrium temperature of the formation of gas hydrate at zero degree C (273.15 K). The constant b is also defined by the following formula.

$$b = \frac{ln(P_0) - ln(a)}{ln(T_0)} \tag{2.22}$$

where a is the constant given in formula (2.21) and T_0=273.15 K.

2.3. Experimental Setup and Procedure

All the gas hydrate formation and decomposition tests were done in a six-sided cell designed by Makogon for gas hydrate formation and decomposition experiments under high pressure and low temperature conditions. The internal volume of the cell is 900 cm^3 and its maximum working pressure is 200 bars. The picture of the cell during a gas hydrate formation experiment is shown in Fig. 7.

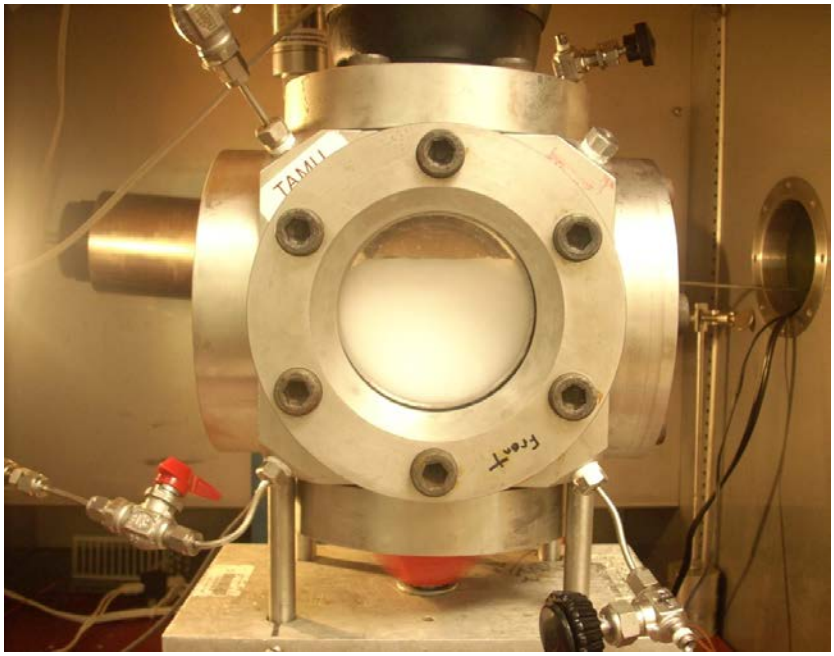

Fig. 8 High pressure cell with six windows used for the formation and decomposition of gas hydrate.

The reactor is constructed from stainless steel type 316 and has a cubic shape with windows in all faces. For being able to see the content of the cell, the windows are chosen from transparent materials. The transparent materials could be chosen from polycarbonate, silica, or sapphire. The polycarbonate could be used for low to medium range of temperatures and silica and sapphire glasses are for higher range of temperatures. For methane hydrate formation, polycarbonate windows were used. Omega PX 906-7.54 KGV pressure transducer and OL-703 thermistor were used for the measurement of pressure and temperature. The readouts from pressure and temperature sensors were acquired and converted to digital signals by National Instrument NI-9219

data acquisition system. A LabVIEW code was written to record and condition digital data from the data acquisition system and record them into spreadsheet files.

Simultaneous to pressure and temperature data acquisition, a video stream from inside the cell was captured by a top camera and recorded by the LabVIEW code. Turbulence and agitation inside the cell was created by a magnetic stirring system on which a magnet inside the cell coupled to a U shape magnet outside the cell. The U shape magnet is mounted on the top of Camfero electrical stirrer equipped with digital controller for rpm control. The high pressure cell setup is placed inside of Thermoteron S-16C refrigerator. The refrigerator is equipped with a digital programmable controller for setting cooling and heating cycles.

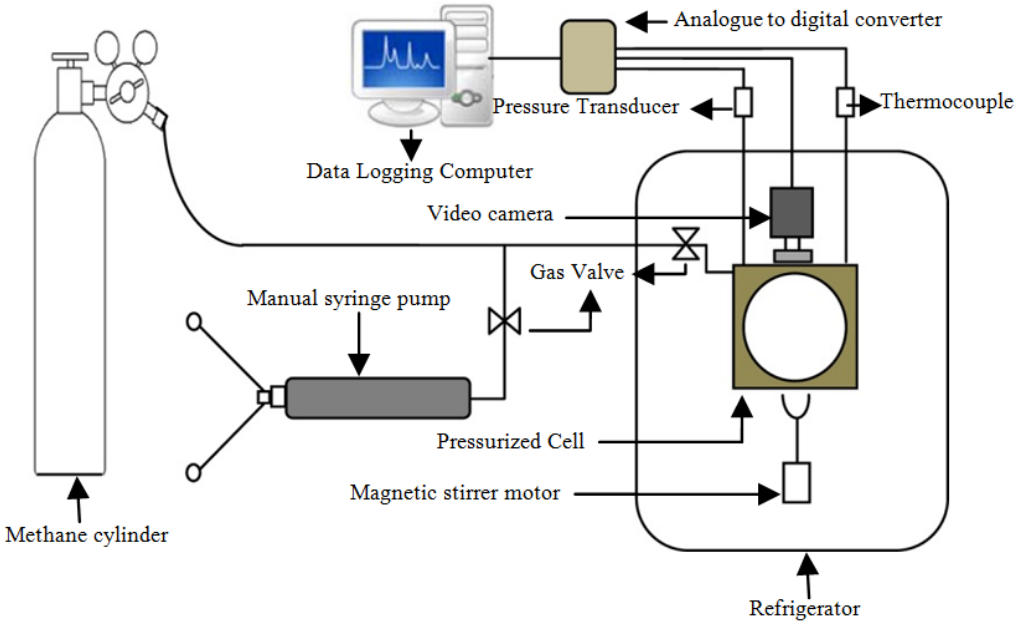

Fig. 9 The schematic of experimental apparatus.

A methane gas cylinder was used to provide methane and pressurize the system. A manual Ruska syringe pump was used to accurately set the pressure to a desirable level. The schematic of setup is shown in Fig. 8.

2.3.1. Experimental Procedure

Prior to all experiments, the cell was washed with distilled water and was cleaned and dried using lens cleaning tissue papers to prevent introducing tissue residuals in the cell. Then, the open cell was blown with inert nitrogen gas to remove all the remaining dust that could act as nucleation sites during gas hydrate formation. The cell then was filled to half of its volume with 557 cm^3 of distilled water. After closing the cell, the air was evacuated with a syringe and then purged with methane gas several times to replace air with methane gas. Then the system was pressurized with pure methane. The refrigerator was turned on to lower the setup temperature to 20°C. The pressure in the cell was aligned to a desirable pressure by a manual Ruska pump, then a magnetic stirrer was turned on and set to 500 rpm. The creation of turbulence in the system by the magnetic stirrer is crucial for the kinetic study of gas hydrate formation or dissociation because it suppresses the mass and heat transfer effects so the test results arise solely from the gas hydrate formation and dissociation kinetics [13]. In the absence of turbulence, the process of gas hydrate formation involves heat and mass transfer as well as the kinetics of gas hydrate formation [1, 3]. The cooling cycle was started after allowing the system to reach a stable and desirable pressure at 20°C. A schematic of the cooling and heating cycle is shown in Fig. 9.

At the beginning, the cell temperature was kept at 20°C for the period of time t_1, so the system would reach a desirable pressure. Once the pressure was stabilized in the cell, a recording of the data was started using LabView software. The system was then cooled down to a temperature below the equilibrium of gas hydrate formation and kept at this temperature for period of time t_2. During this period of time, the gas hydrate started to form and the cell pressure started to decrease.

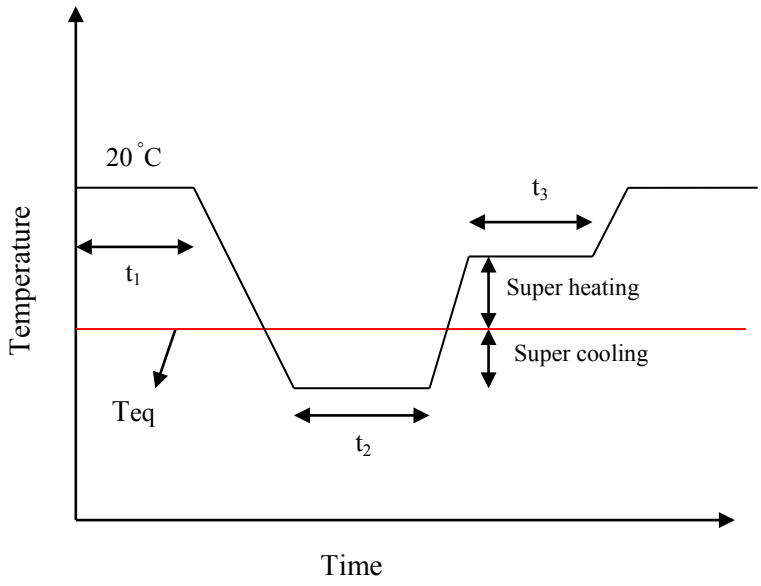

Fig. 10 A schematic of the heating and cooling cycle for formation and dissociation of gas hydrate.

After the system pressure decreased to a certain level, the heating cycle was started. The cell temperature increased to a certain temperature above the equilibrium temperature of gas hydrate decomposition to create a desirable super-heating. The cell

was kept in this isothermal condition until all the gas hydrate crystals decomposed in the cell and no visual sign of gas hydrate remained in the system. The temperature was then raised to 20°C and data acquisition was stopped and all the acquired data were saved.

2.3.2. Experimental Results

The results of the cooling and heating tests for formation and dissociation of gas hydrate are explained in this section. The initial temperature and pressure were 20°C and 2000 psi respectively. Methane gas with purity of 99.99 wt% and double distilled pure water were used for the formation of the gas hydrate. The cell was cooled down continuously until gas hydrate started to form in the cell. The temperature at which gas hydrate started to form was 0.6 °C lower than the equilibrium gas hydrate formation temperature, therefore, the subcooling was equal to 0.6 °C. The equilibrium temperature of gas hydrate formation could be defined by the temperature at which the gas hydrate equilibrium curve and experimental curve intersect.

The gas hydrate equilibrium formation temperature was 13°C in this experiment. The amount of subcooling in the test with respect to the equilibrium gas hydrate formation temperature, i.e. the intersection of the equilibrium and experimental pressure-temperature curves, are shown in Fig. 10. After the onset of gas hydrate formation, the system was kept in an isothermal condition by maintaining a near-constant temperature.

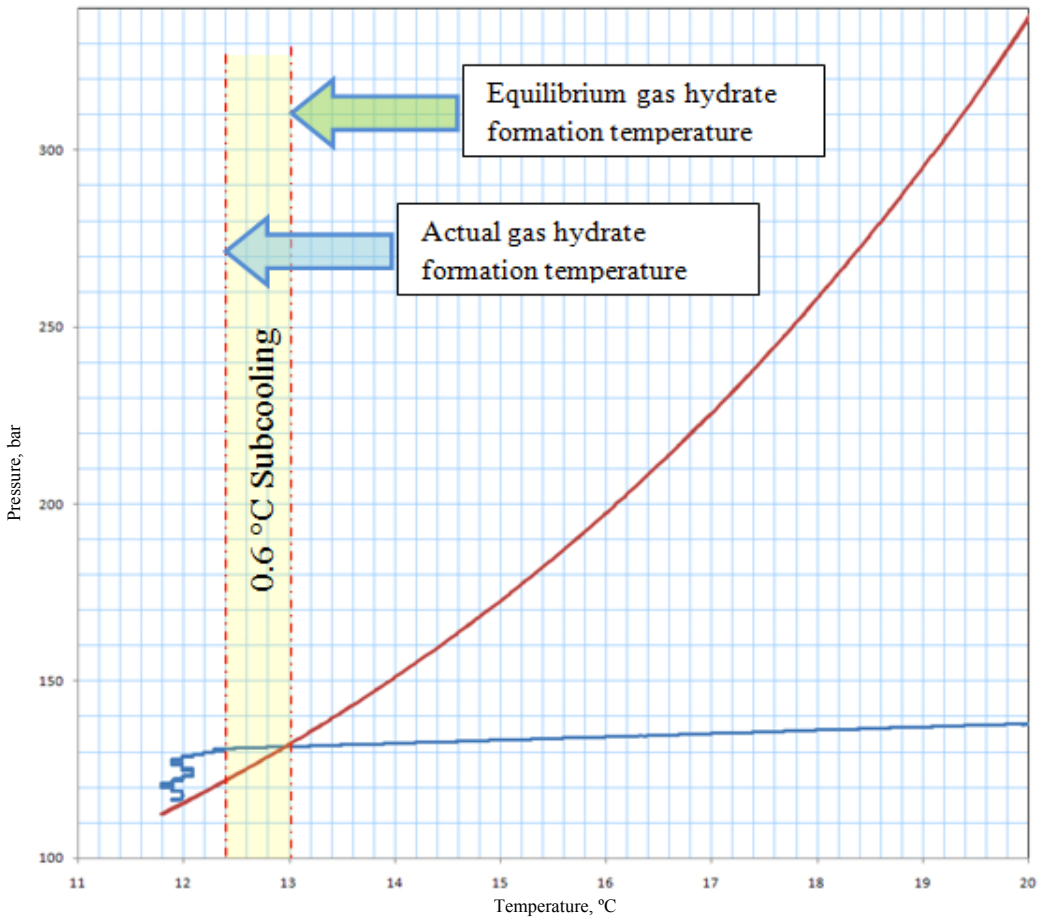

Fig. 11 Equilibrium and experimental pressure-temperature curves. The subcooling for this experiment is 0.6°C. The red and blue curves show the equilibrium gas hydrate formation curve and experimental curve respectively.

As shown in Fig. 10, the equilibrium gas hydrate formation temperature was 13°C, but the gas hydrate started to form at the temperature of 12.4°C under experimental conditions, and consequently, the super cooling temperature was 0.6°C. In Fig. 11, the

experimental pressure-temperature curve and the hypothetical line used for calculation of consumed gas and formed gas hydrate volume are shown.

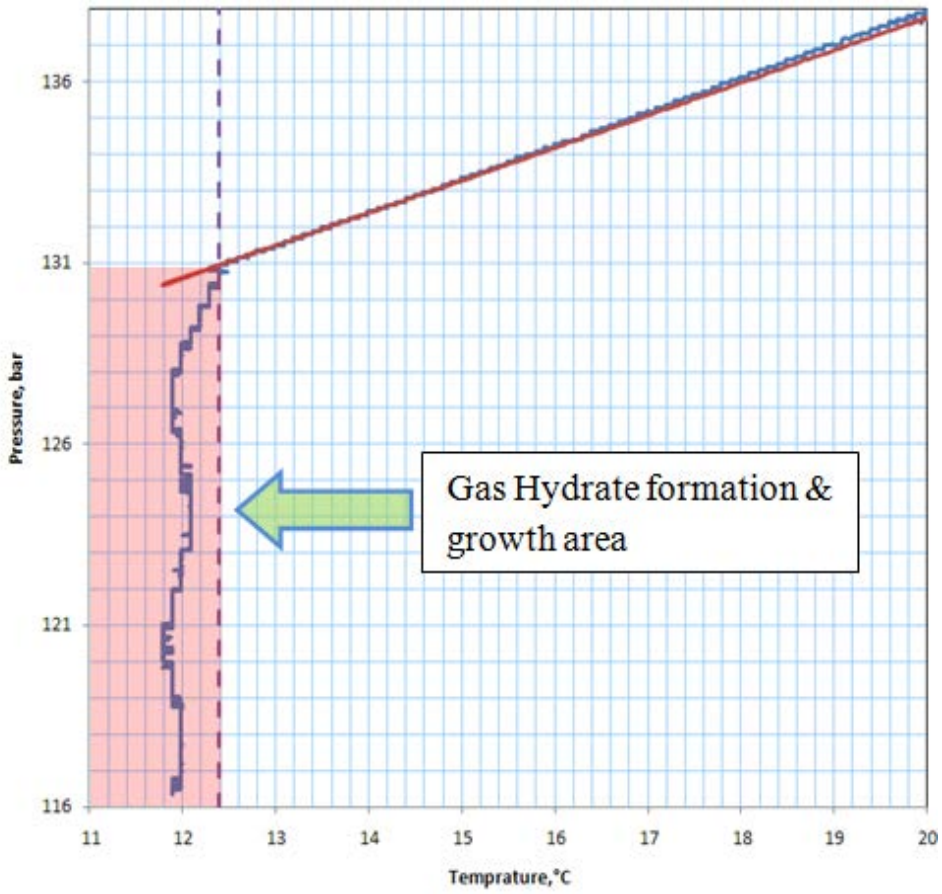

Fig. 12 Experimental pressure-temperature curve (blue color) with hypothetical fit line (red).

An effort was made to maintain the gas hydrate growth under an isothermal condition at 12°C. As shown in the graph, the temperature variation around 12°C is ±0.1°C, which shows a good isothermal condition considering the system temperature control capabilities. Another observation that could be highlighted from Fig. 11 is that the pressure changes linearly versus temperature before the formation of gas hydrate, which justifies the validity of the method used in this research for calculation of the moles of consumed methane gas.

According to the method mentioned in the previous section, the moles of consumed methane gas during gas hydrate formation were calculated and plotted versus time as shown in Fig. 12. The dashed line in the graph shows the start temperature of gas hydrate formation. Also, the graph of calculated volume of formed gas hydrate on the basis of the moles of consumed gas is shown in Fig. 13.

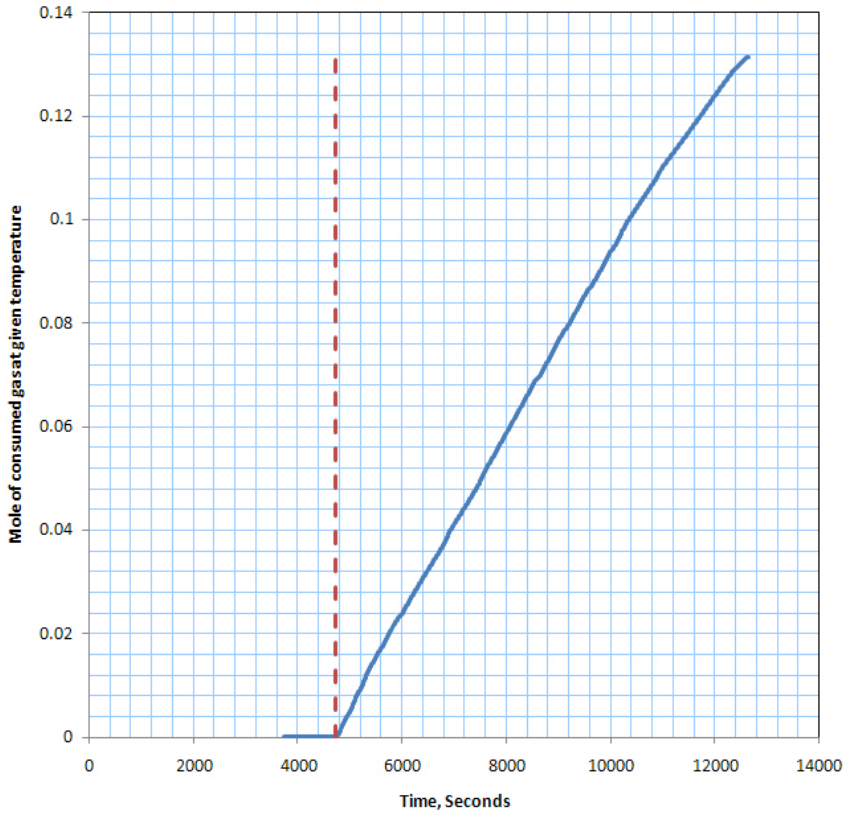

Fig. 13 The graph of consumed gas versus time during hydrate formation and growth process.

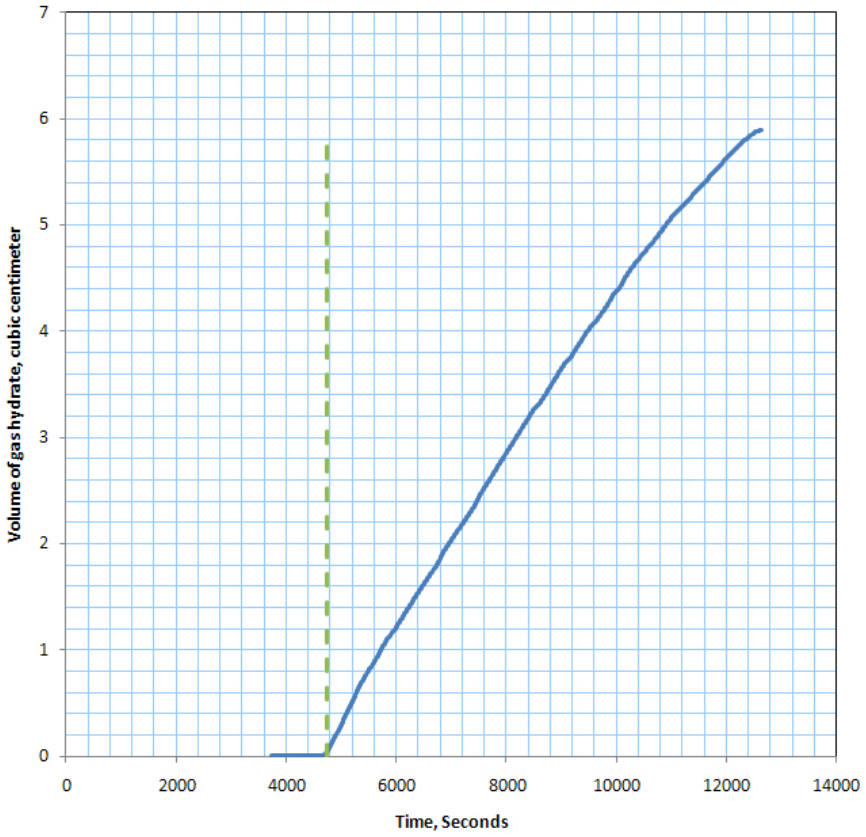

Fig. 14 The graph of formed gas hydrate volume versus time during hydrate formation and growth process.

For decomposition of the gas hydrate formed in the cell, the system was heated continuously to decompose the formed gas hydrate completely. The pressure-temperature curve during the heating process is shown in Fig. 14. As shown in Fig. 14, the pressure–temperature curve is approximately linear after the complete decomposition of gas hydrate, which shows the expansion of methane gas during this period.

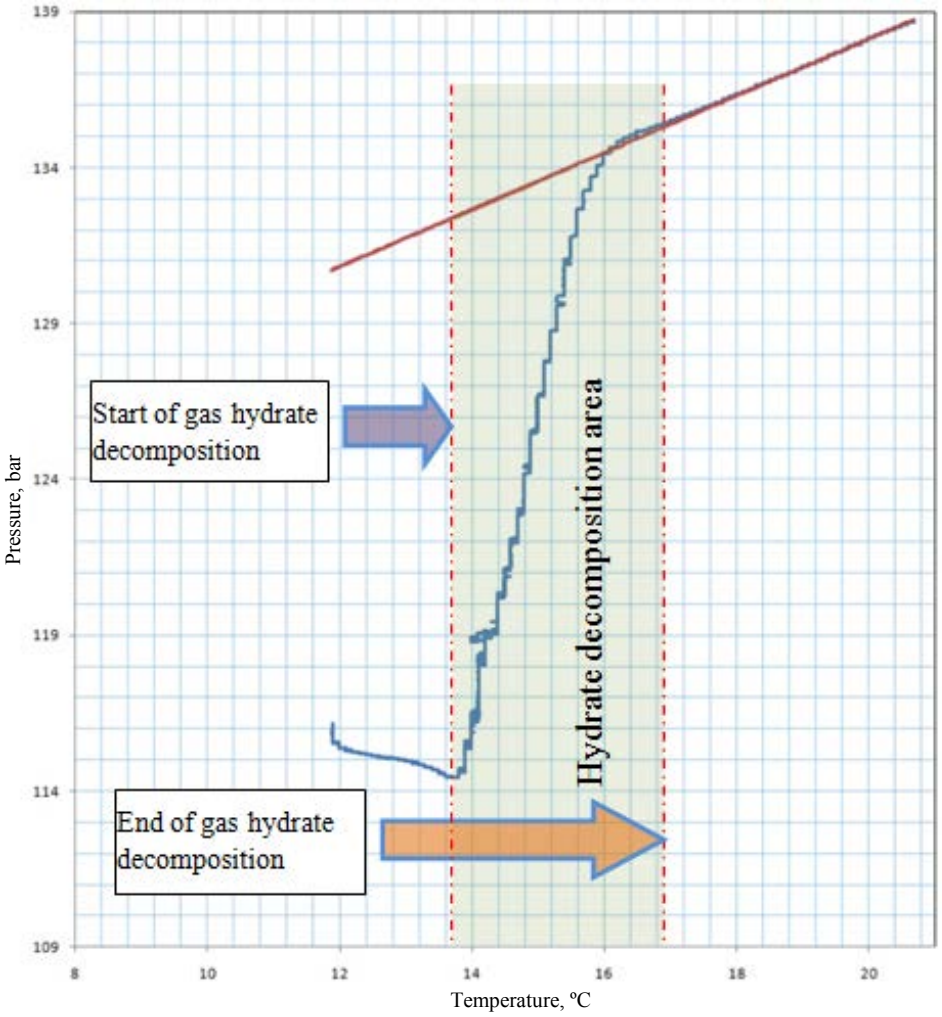

Fig. 15 Experimental pressure-temperature curve during heating period.

Similar to the cooling period, the moles of generated gas during gas hydrate decomposition are calculated and shown in Fig. 15. Also, the graph of the volume of gas hydrate in the cell versus time is shown in Fig. 16.

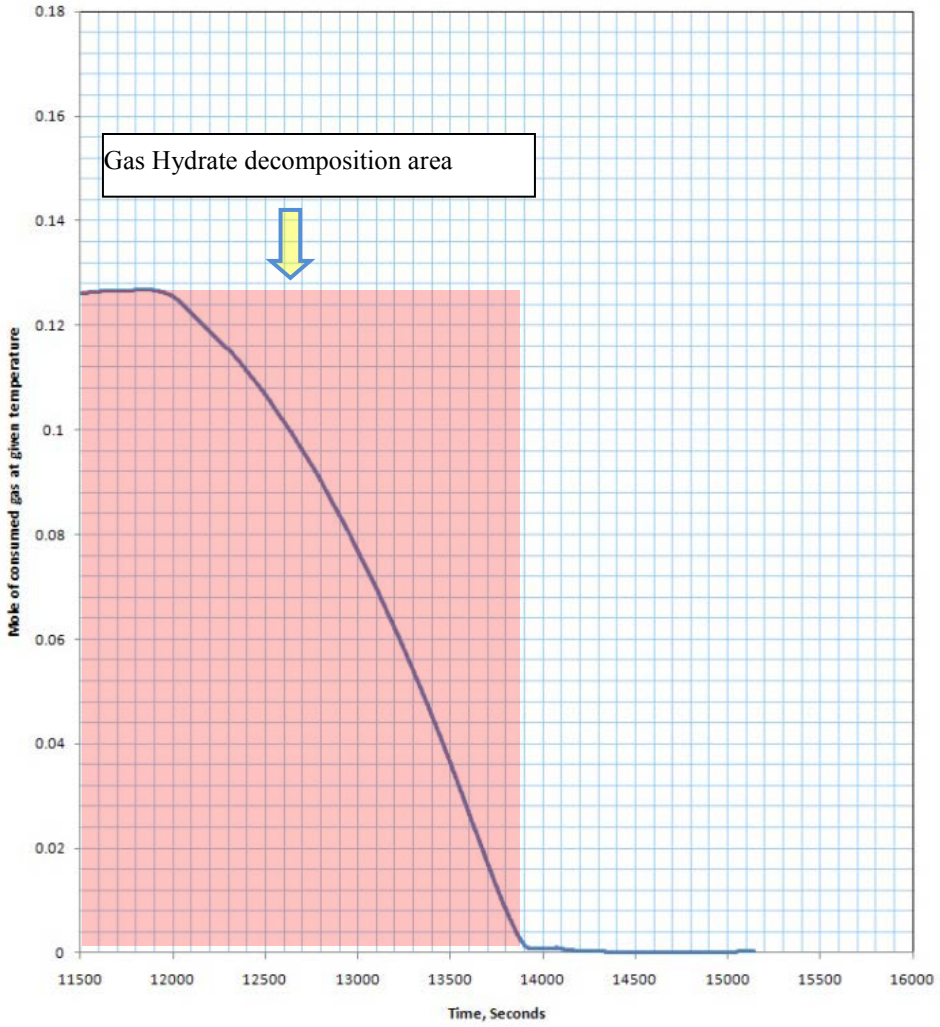

Fig. 16 The volume of consumed gas during heating process.

As shown in Fig. 15, the moles of methane gas in the gas hydrate phase decreases with time because of gas hydrate decomposition. Similarly, the volume of gas hydrate decreases with time, as can be seen in Fig. 16. The decrease in gas hydrate volume shows the continuation of the gas hydrate decomposition process.

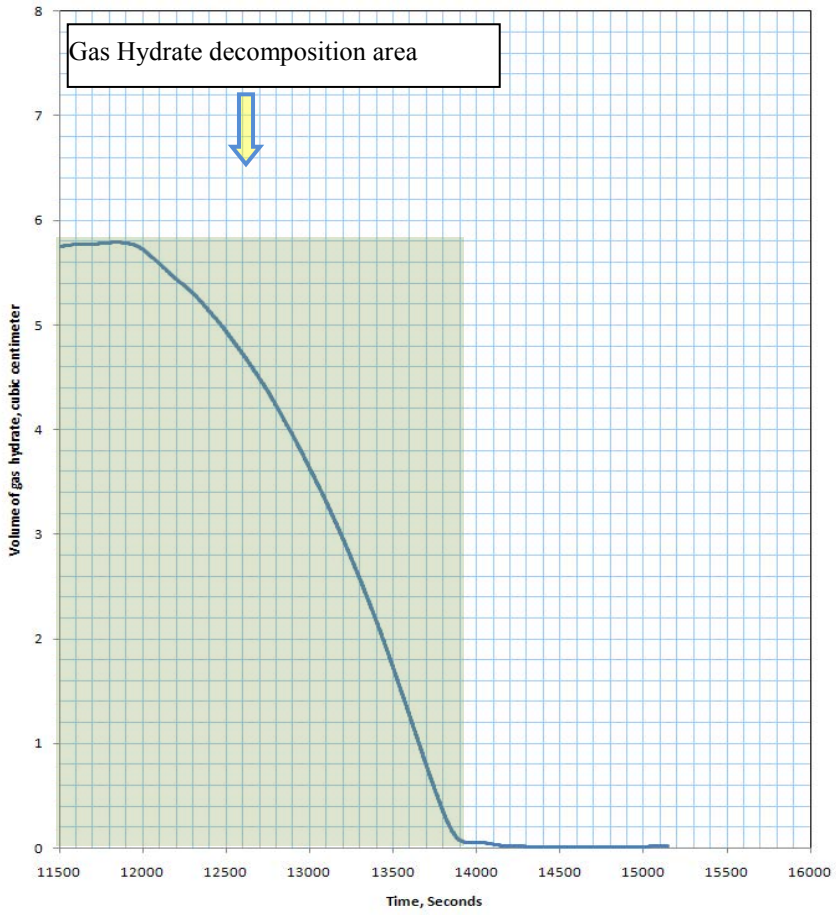

Fig. 17 The volume of gas hydrate during heating period.

For comparison of the effect of different subcoolings on the amount of consumed moles of methane gas during gas hydrate formation, the experiments have been carried out with subcooling temperatures of 0.2, 0.3, 0.6 and 4.6°C and initial pressures of 2000 and 2500 psi. All the results of experiments are plotted on the same graph. The start time of gas hydrate formation is considered as a time zero in the graph. The results are shown in Fig. 17.

As shown in the plot, with increase in initial pressure and subcooling temperatures, the amount of consumed gas is increased. This result indicates that there is a higher driving force for gas hydrate formation when initial pressure and subcooling temperature is increased. The results of these experiments support those obtained by Englezos *et al.*, which show that gas hydrate forms faster at higher pressures [13].

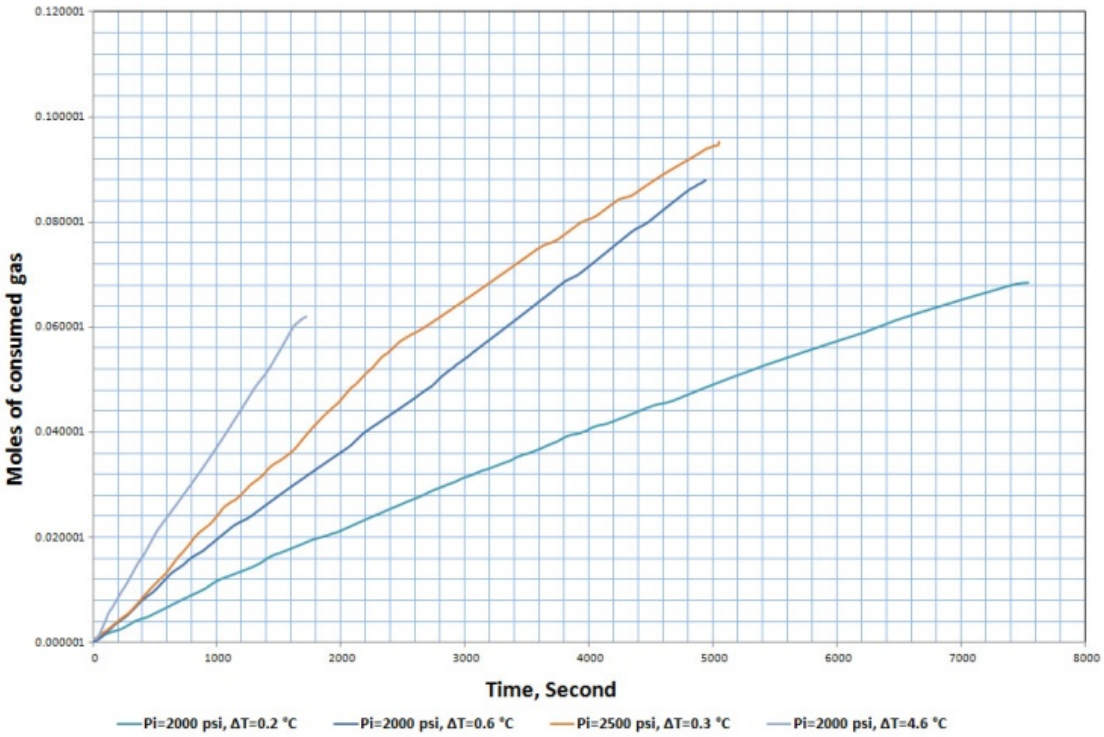

Fig. 18 The plots of consumed moles of methane gas during formation of gas hydrate versus time under different subcooling and initial pressure conditions.

3. FORMATION OF ICE AND GAS HYDRATE UNDER HIGH COOLING RATES

3.1. Introduction

Production of gas hydrate by the depressurization method is the most favorable method among three methods of gas production from gas hydrate bearing sediments because of its simplicity, technical and economic advantages over the thermal and chemical stimulation methods [34]. The results of past research show a high rate of gas production from gas hydrate reservoirs could be obtained by lowering wellbore pressure to make an appropriate drawdown pressure. The results of gas production simulation from gas hydrate deposits in Prudhoe Bay L-Pad in the arctic region of north Alaska showed the maximum sustained production rate of 100,000 m^3/day (3.5 MMscf/day) could be obtained by lowering the downhole pressure from the initial pressure of 7.3 MPa to 2.7 MPa [35, 36]. Makogon reported the gas production rate as high as 130000 m^3/day (4.59 MMscf/day) in the production wells completed 100% in the Mesoyakha type I hydrate bearing strata in Siberia, Russia [37].

Kurihara *et al.* showed the maximum gas production rate of 170000 m^3/day could be obtained from the hydrate bearing sediments of Nankai Trough in offshore Japan [38]. These high production rates are necessary for making the production from gas hydrate reservoirs economically feasible. One of the consequences of high rate gas production from a hydrate bearing reservoir is high gas velocities and pressure drops near the wellbore. The high amount of pressure drops near the wellbore cause a considerable cooling effect because of the Joule-Thompson effect [39].

As pointed out by Alp et al., the cooling effect near the wellbore could cause secondary hydrate formation [40]. Shahbazi *et al.*, furthermore, showed the endothermic nature of gas hydrate dissociation and the Joule-Thompson cooling effect could decrease reservoir temperature near the wellbore area to a subzero temperature and cause ice formation [41, 42]. The formation of ice and gas hydrate could considerably reduce effective permeability near the wellbore and in severe cases plug the area around the wellbore and cause gas flow termination [43].

In the current study, the formation of gas hydrate and ice are suppressed by high cooling rates of 0.6 and 0.45 °C/min to create supercooled water. This suppression of hydrate formation temperature brings the nucleation phenomena with a probabilistic nature to its deterministic boundary and caused spontaneous nucleation and growth of ice and gas hydrate phases at subzero temperatures. Two types of pure water and standard sea water were used in this study with the initial pressures of 1500, 2000 and 2500 psi and the initial temperature of 20°C. After the formation of gas hydrate and ice in the cell, the system is heated up again to melt ice and dissociated gas hydrate. The process of formation and dissociation of gas hydrate and ice are repeated several times to study the effect of the memory phenomenon [1, 2] on the start temperatures of ice formation.

3.2. Experimental Section

3.2.1. Experimental Setup

The high cooling rate, gas hydrate and ice formation tests have been done in a homemade stainless steel cell designed by Makogon at the Department of Petroleum Engineering at Texas A&M University. The experiments were started by cooling down the cell to a desirable temperature by circulating refrigerator fluid provided by a VWR Scientific 1157 external refrigerator. The refrigerator was equipped with a digital programmable controller for setting cooling and heating cycles. The internal volume of the cell was 161.5 cm^3, and its maximum working pressure was 200 bars. The picture of the cell during a gas hydrate-ice formation experiment is shown in Fig. 18.

Fig. 19 High pressure stainless steel cell used for formation and decomposition of gas hydrates.

The reactor has a cylindrical shape with two windows in both of its ends. In order to be able to see the content of the cell, the windows of the cell were chosen from polycarbonate transparent materials. The Omega PX 906-5 KGV pressure transducer and OL-703 thermistor were used for measuring pressure and temperature, respectively. National Instrument NI-9219 data acquisition system was used for data acquisition purposes. A LabVIEW code was written to process pressure, temperature and video data and save them into files. The methane gas for experiments was provided by a pressurized methane cylinder, and a manual Ruska pump was used for fine pressure alignment. The schematic of the experiment's setup is shown in Fig. 19.

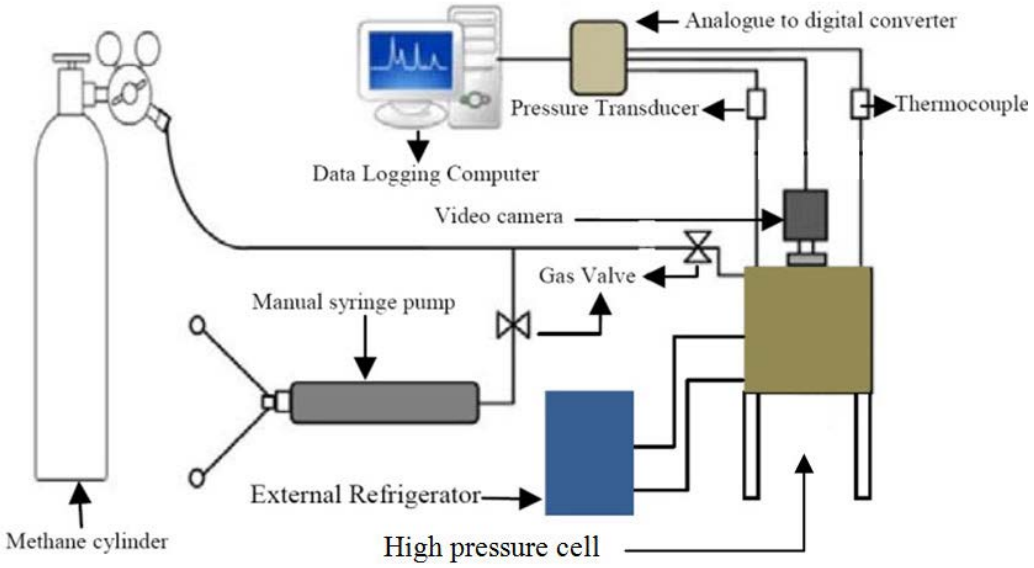

Fig. 20 The schematic of the experimental apparatus.

3.2.2. Experimental Procedure

Prior to any experiment, the cell was washed with distilled water and then dried by lens cleaning papers. Then the cell was blown by nitrogen gas to remove all the remaining dust and paper residuals. The cell then was filled to half of its volume with distilled water. After closing the cell and to replace the air with methane gas, the air was sucked by a syringe and then purged by methane gas several times. Then, the system was pressurized by the pure methane gas cylinder, and the refrigerator was turned on to lower the setup temperature to 20 $^{\circ}$C.

After temperature was stabilized, the pressure was aligned to a desirable pressure by a manual Ruska pump. Afterward, the cooling process and data recording by LabView software were started simultaneously. The system was cooled down to a temperature below 0 $^{\circ}$C, or the freezing point of water, and kept at this temperature for a period of time, t_2. During this period, usually a very thin layer of gas hydrate forms, followed by a sudden formation of a thick layer ice. After the completion of ice formation in the system, the heating cycle was started and the system temperature was increased continuously to 20 $^{\circ}$C. In 0°C, the ice started to melt followed by gas hydrate decomposition in higher temperatures. Data acquisition from the cell was stopped by reaching 20 $^{\circ}$C, and all of the acquired data were saved to a file for post-processing. The schematic of the cooling and heating cycles are shown in Fig. 20.

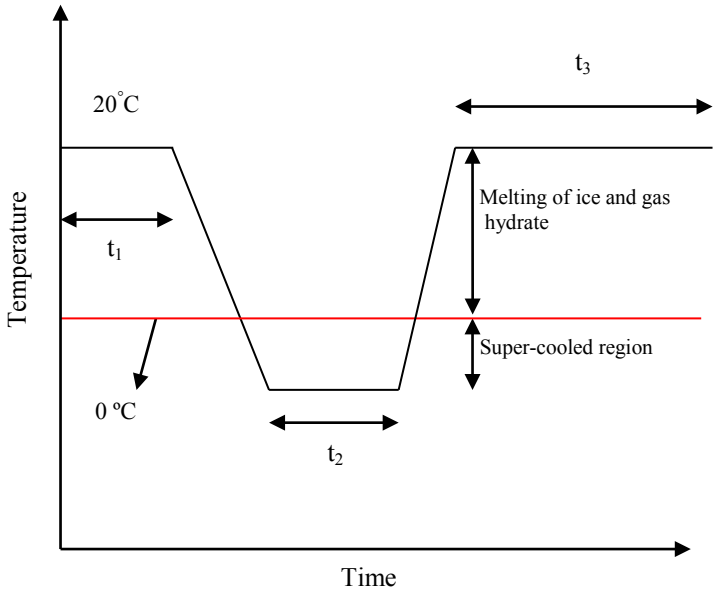

Fig. 21 The schematic of heating and cooling cycles for the formation and dissociation of gas hydrate.

A VBA code was developed to post-process raw data saved by LabView and then plot them in the form of different graphs in Excel. After recording the data, the tests were repeated three times to study the effect of residual ice and gas hydrate structures in water at the ice formation temperatures.

3.3. Results and Discussion

The experiments were started at 20 ±0.5°C, and the gas hydrate formation cell was cooled with the fastest available cooling rate. The high cooling rates suppressed gas hydrate and ice formation temperatures to temperatures below 0°C and created supercooled water. Decreasing water temperature to subzero temperatures increase the probability of thermodynamically stable nucleation [1] until the temperature reaches a point that the nucleation is not a random process anymore and stable nuclei become available and grow spontaneously.

In the current study, the temperature of the cell decreased continuously until the spontaneous nucleation and growth of gas hydrate and/or ice phases happened in the system. After the formation of gas hydrate and ice phases, the temperature in the cell was lowered until all of the available liquid water converted to ice. The results of a typical cooling test are shown in Fig. 20. The initial temperature, initial pressure and the volume of water in the cell were 20.01°C, 1502.45 psi and 80.3 ml, respectively. The experimental pressure-temperature results of the test as well as calculated equilibrium curve are shown in Fig. 21. The crossover of two curves shows the equilibrium pressure and temperature of methane hydrate formation in the system.

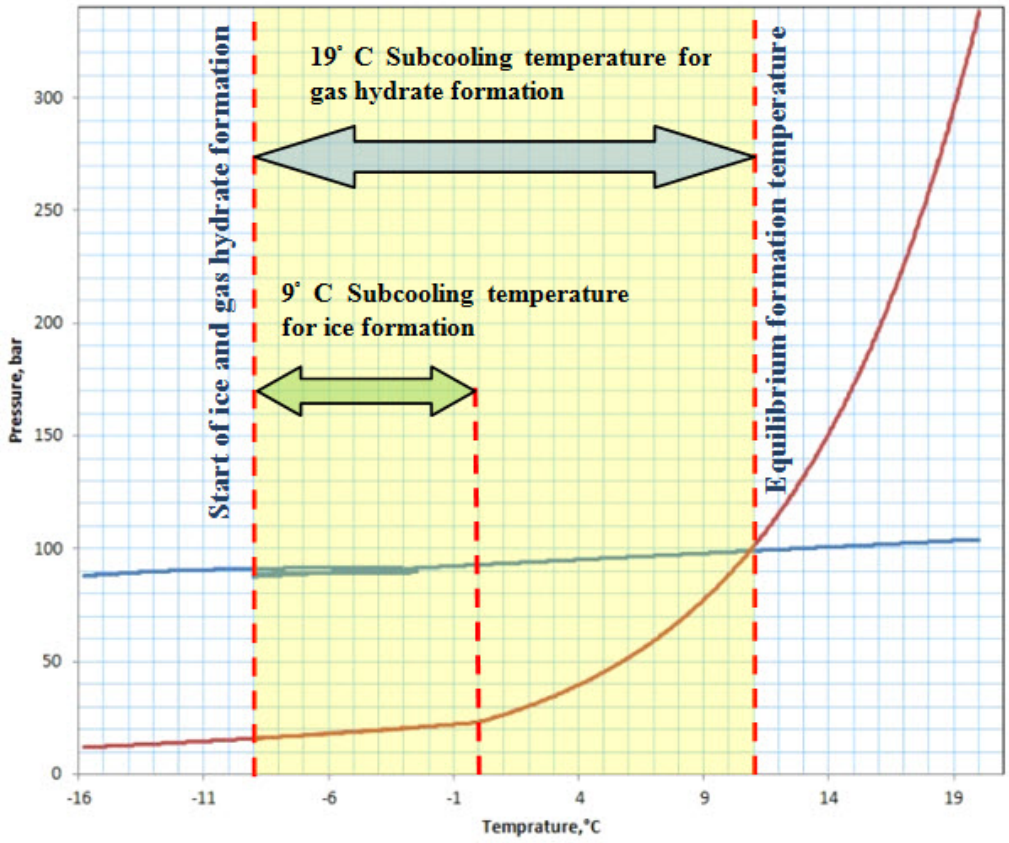

Fig. 22 Equilibrium (red curve) and experimental curve (blue curve) for the methane hydrate formation test. The amounts of subcooling temperature for ice and gas hydrate formation are shown in the graph.

Any temperature lower than the equilibrium temperature creates subcooling for gas hydrate formation. The equilibrium formation temperature of ice is 0°C, and any subzero temperatures provide subcooling for ice formation. As shown in Fig. 21, there is a high degree of supercooling equal to 19 °C for gas hydrate formation. After decreasing temperature to -9 °C by continues cooling, a very thin layer of gas hydrate started to form

and grow on the water-gas interface. The picture of a formed layer of gas hydrate is shown in Fig. 22.

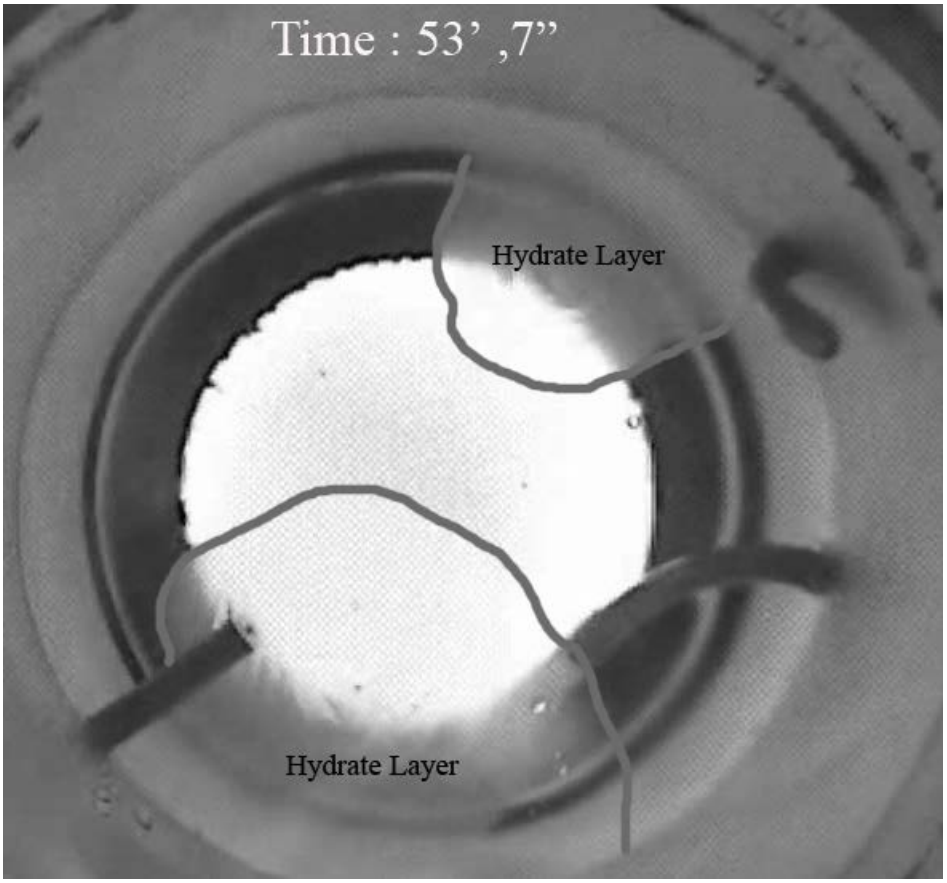

Fig. 23 The thin layer of gas hydrate formed in the water-gas interface.

Immediately after the formation of gas hydrate layer and with a delay of 1 second, a thick layer of ice started to form. On the basis of laboratory observations and videos recording during ice and gas hydrate formation period, the growth rate of ice was

much higher than gas hydrate growth rate. A thick layer of ice covered the entire water surface in less than 1 second and caused a big jump in cell pressure and temperature.

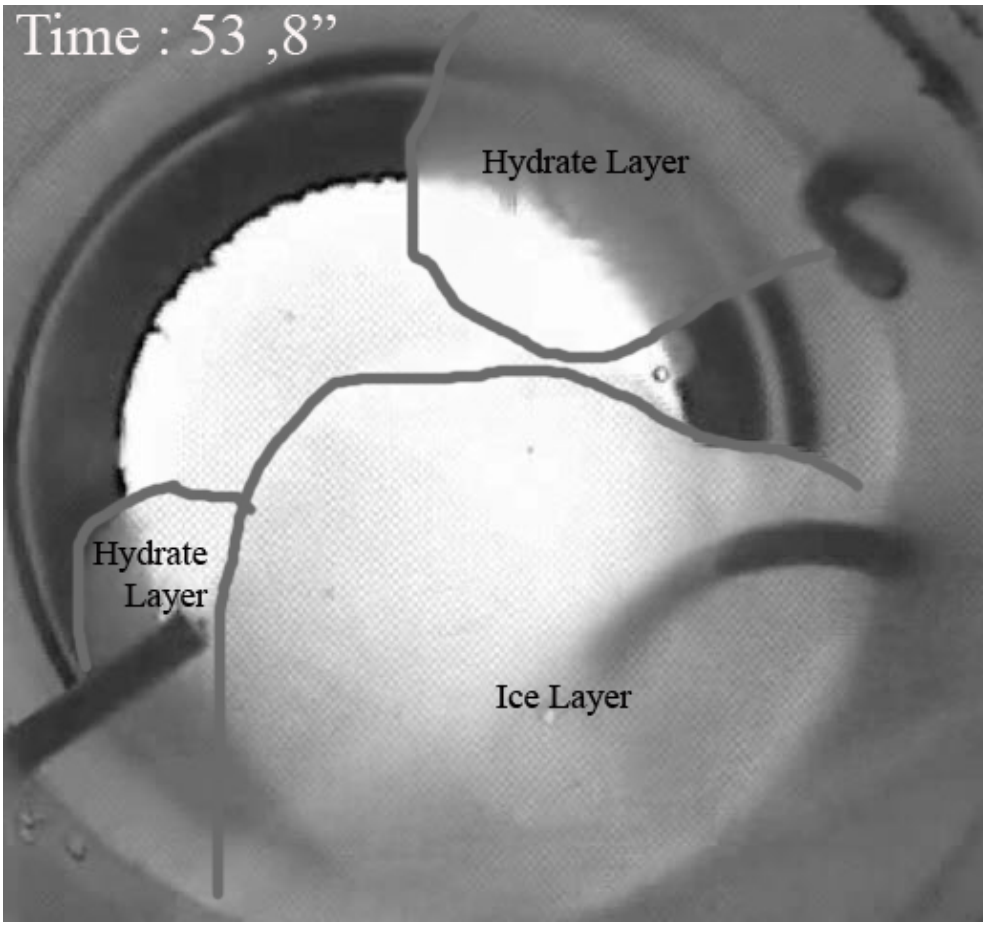

Fig. 24 A thick layer of ice formed and grew with a very high rate and covered the entire water-gas interface. Gas hydrate and ice layers are shown in above picture.

The picture of ice and gas hydrate layer is shown in Fig. 23. In the picture, the thin gas hydrate layer could be recognized from the thick ice layer by being more transparent. Considering the exothermic nature of ice formation and its volume expansion, there is a sudden increase in cell pressure and temperature due to the very fast growth rate of the ice phase. The amount of observed jump in cell temperature was 3.1 $^{\circ}$C. The graph of temperature versus time is shown in Fig. 24. It should be noted that no observable changes in pressure and temperature happened after gas hydrate formation because of the very small amount of formed methane hydrate.

Another reason for the negligible observed effect of gas hydrate formation on pressure and temperature data is that the formation of gas hydrate happened immediately before ice formation under high cooling rate conditions and its effect was masked by the formation of the large amount of ice. Also, as shown in Fig. 24, the cooling rate of water in the cell decreased from 0.6 $^{\circ}$C/min to 0.4 $^{\circ}$C/min by entering the subzero temperature range. The change in water cooling rate happened in spite of the fact that the refrigerator cooling rate was kept constant.

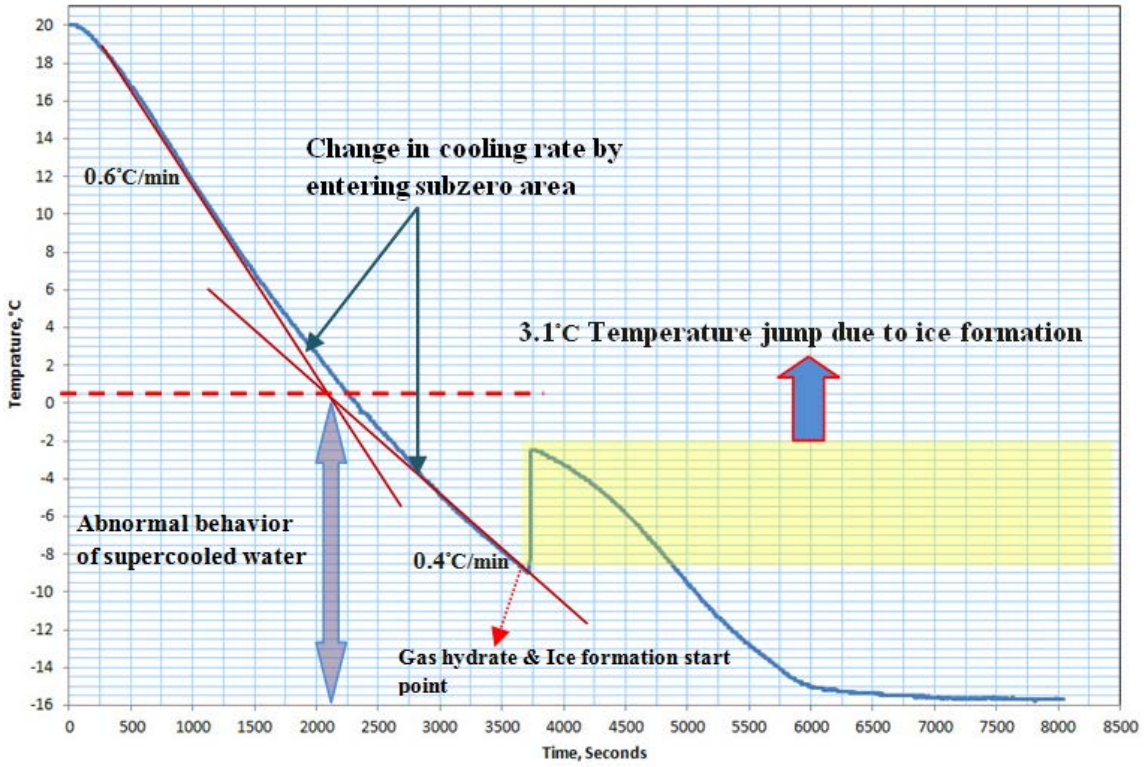

Fig. 25 Experimental temperature versus time curve for pure water-pure methane system. The cooling rates above and below 0 °C as well as the jump in temperature due to ice formation is shown.

The lower cooling rate in subzero temperatures can be explained by the abnormal properties of supercooled water. The study of Angel *et al.* [44] and Speedy [45] showed that the heat capacity of water increases when the temperature decreases to subzero temperatures. By increasing the amount of water heat capacity and considering the fact that cooling power generated by the refrigerator was constant, water in the cell experienced lower cooling rates.

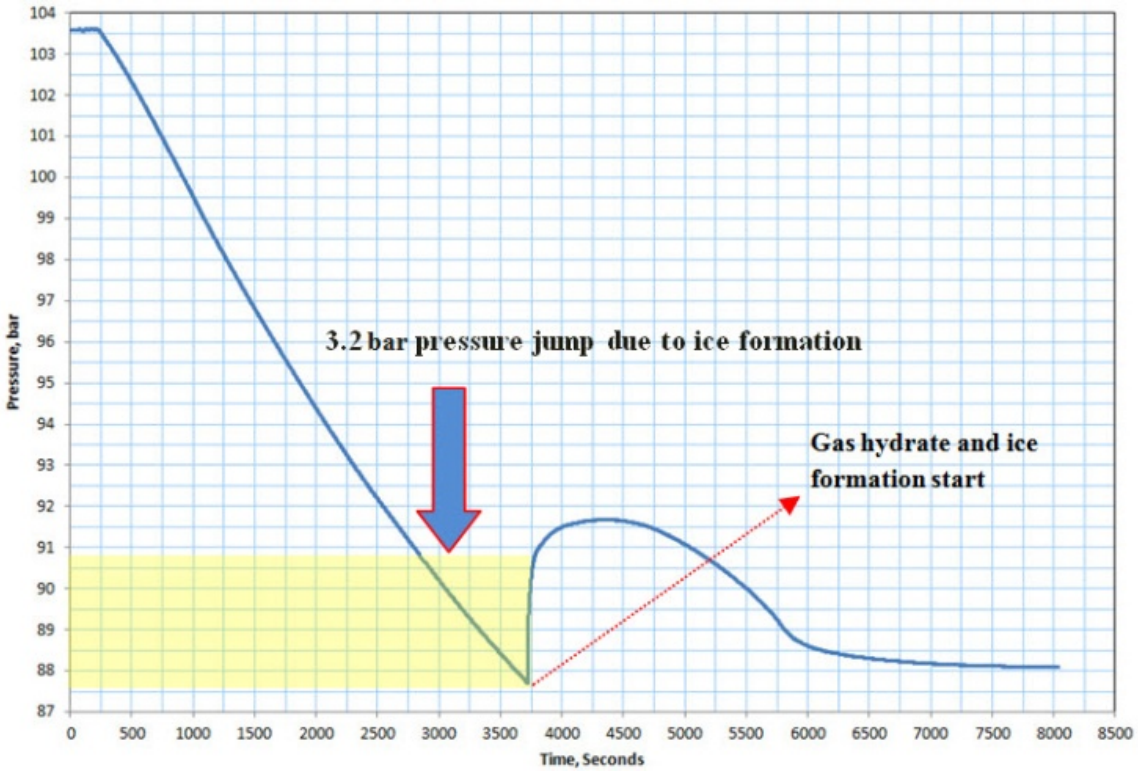

Fig. 26 The experimental results of pressure versus time for pure water-pure methane system. A 3.2 bar jump in pressure was observed in the system due to volume increase related to ice formation.

Another phenomenon observed during ice formation was a sudden increase in pressure. As shown in Fig. 25, there was a sudden pressure increase in the cell equal to 3.2 bar immediately after ice formation. The fast increase in pressure was caused by volume expansion during the water to ice phase transition. In addition, the graph of experimental pressure versus temperature is shown in Fig. 26. As observed in the graph, the pressure versus time curve is linear before ice formation. This section shows a

decrease in pressure because of gas contraction. After formation of ice there is a sudden increase in pressure and temperature in the cell. However, the sensation of pressure and temperature by thermistor and pressure transducer sensors did not happen in the cell at the same time.

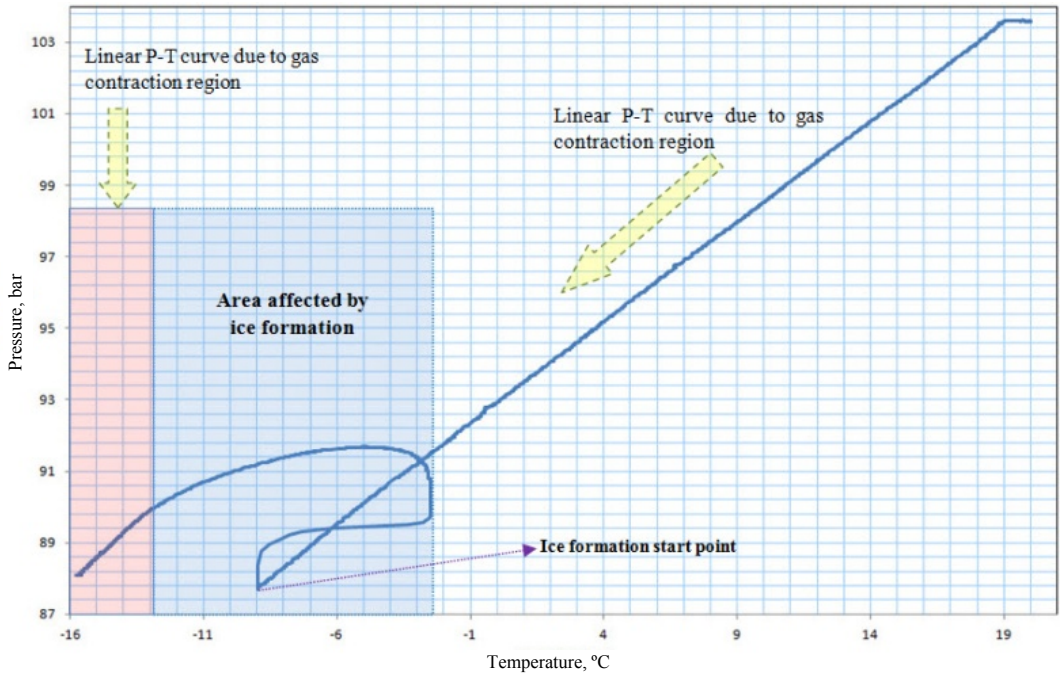

Fig. 27 The graph of pressure versus temperature for pure water-pure methane system.

The increase in the pressure was sensed immediately by the pressure transducer. The jump in temperature, however, was delayed since a short time was needed for heat transfer from the surrounding media to the tip of the thermistor. Consequently, a shift in pressure jump was observed because of the delay in temperature measurement caused by heat transfer. This shift can be seen in Fig. 26. The area affected by the ice formation is

highlighted with a red box. After the formation of ice in the system, the temperature was lowered to eliminate the ice formation perturbation effect on the cell pressure and temperature. Once the formation of ice was completed, a linear section was again observed in the curve, which corresponds to the pressure decrease caused by gas contraction in the gas-ice system. This area is highlighted in red.

As seen in Fig. 24 and Fig.26, the ice and gas hydrate were formed at -9 $^{\circ}$C instead of their equilibrium formation temperatures. The comprehensive results of the experiments with different initial pressures and two types of pure water and standard sea water solutions are shown in Fig. 26. The initial pressures used in the study were 1500, 2000 and 2500 psi. The pure water was double distilled and the sea water was the standard sea water solution with the composition mentioned in reference 46 and 47.

As shown in Fig. 27, the initial pressures and water chemical composition do not have a considerable effect on the formation temperatures of gas hydrate and ice in the cell. Beside the red curve which has a different cooling rate, all the other tests with similar cooling rates of 0.45 $^{\circ}$C/min showed very close gas hydrate and ice formation temperatures. In the case of the red temperature-time cooling curve, the system experienced a higher cooling rate of 0.6 $^{\circ}$C/min.

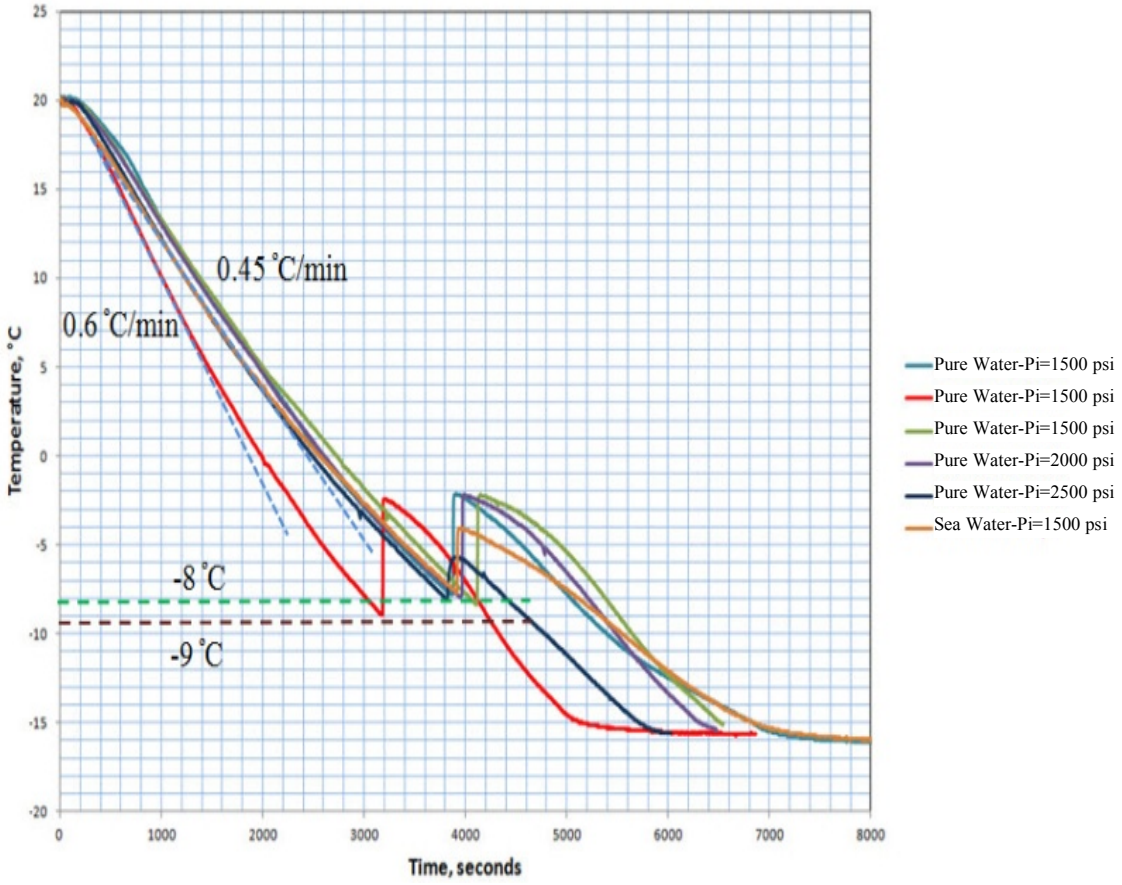

Fig. 28 Temperature-time curves for gas hydrate and ice formation using pure water-pure methane and sea water-pure methane solutions.

The higher cooling rate caused more suppression in gas hydrate and ice formation temperatures. The observed parameters of the curves shown in Fig. 27 are mentioned in Table 4. As seen from Table 4, initial pressure and water composition do not affect the ice and gas hydrate formation temperatures greatly. However, by the change in cooling rate from 0.45 ˚C/min to 0.6 ˚C/min , the temperatures on which ice and gas hydrate phases started to form were changed considerably from -8 ºC to -9 ºC.

Table 4 The test parameters for the water-pure methane system with different initial pressures, cooling rates and liquid chemical compositions.

Initial pressure, psi	Cooling rate, °C/min	Liquid composition	Ice & gas hydrate start temperature, °C	Temperature jump, °C
1500	0.4	Pure water	-8.2	6
1500	0.4	Pure water	-7.9	5.9
1500	0.6	Pure water	-9	6.5
1500	0.4	Standard sea water	-7.8	3.9
2000	0.4	Pure water	-8	5.8
2500	0.4	Pure water	-8.1	2.3

After the formation of gas hydrate and ice in the cell, the temperature was increased to melt ice and decompose gas hydrate phases. The experiments were then repeated several times to study the effect of consecutive heating and cooling cycles on the formation temperatures of ice and gas hydrate. The result of the experiment for the pure water-pure methane system with the initial pressure of 1500 psi is shown in Fig. 28. The results showed that , in the repeated tests, the temperatures at which the gas hydrate and ice phases started to form are higher than the temperature of gas hydrate and ice formation in the initial fresh water test. In the fresh water, ice started to form at -9 °C. However, in the first and second repeated tests, ice formed at higher temperatures of

-6.6 °C and -7.25 °C, respectively. The cooling rates were constant during all the experiments. Pressure-temperature curves of the experiments are shown in Fig. 29.

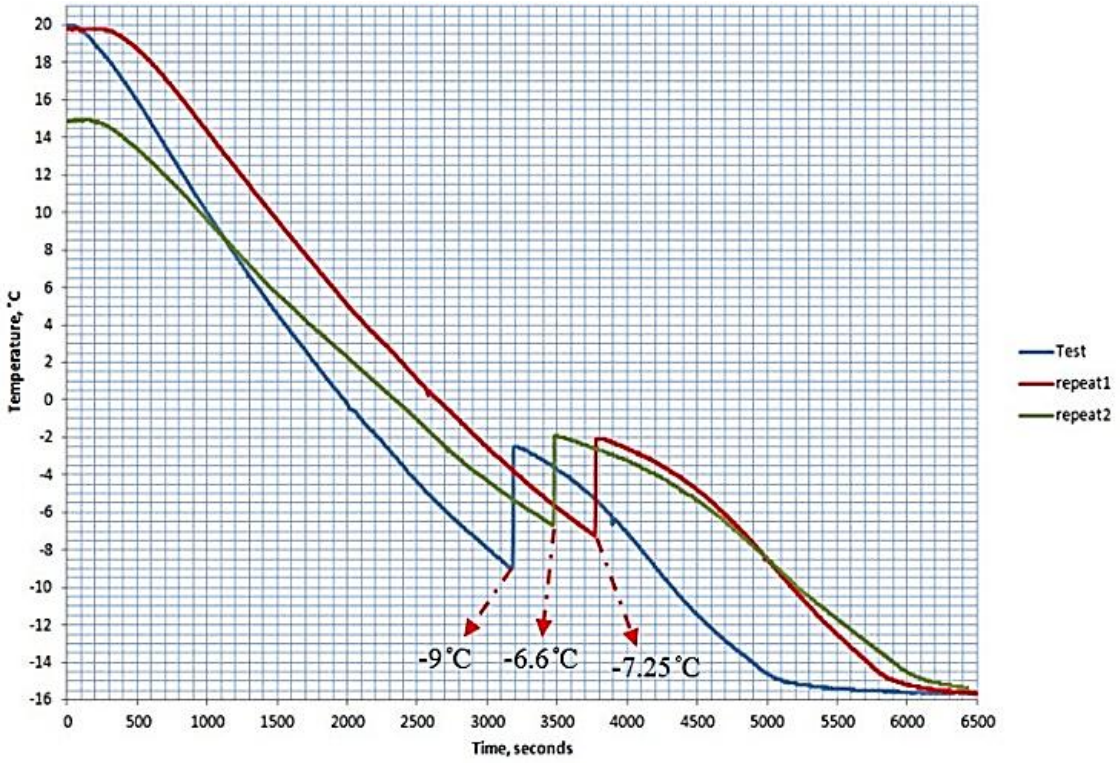

Fig. 29 The graphs of temperature versus time for a pure water-pure methane system with initial pressure of 1500 psi.

The only parameter that played a role in the increase of ice formation temperatures was the existence of residual structure in the water that facilitated the formation of ice in the cell [1, 3].

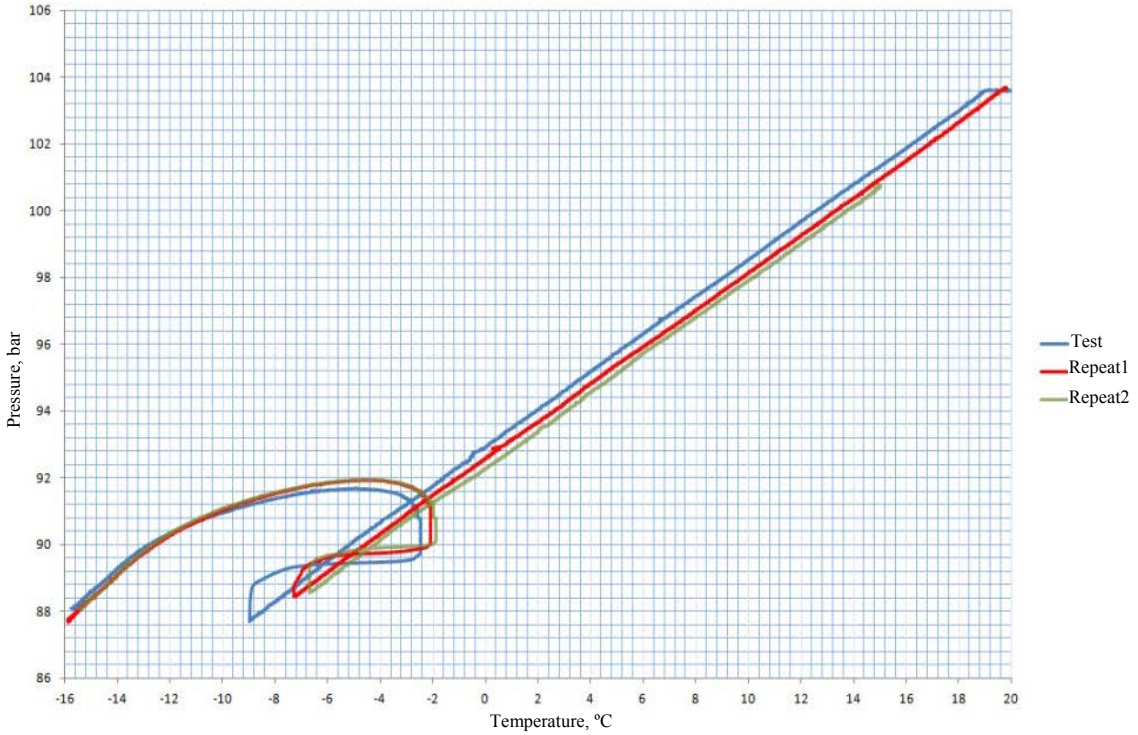

Fig. 30 Pressure-temperature curve of the cooling experiments in the pure water-pure gas system with the initial pressure of 1500 psi.

These residual structures provided heterogamous nucleation sites for the ice formation. The experiments were repeated in pure water-pure methane systems with a higher initial pressure of 2000 psi. The graphs of the temperature-time are shown in Fig. 30. Similar to the results of the tests in 1500 psi, the start temperature of ice formation in the initial fresh water test was lower than those temperatures for the repeated tests. In the case of fresh water, the ice phase started to from at -8 $^{\circ}$C. However in the first, second and third repeats of the test, the ice phase begun to form at -5.2 $^{\circ}$C, -4.2 $^{\circ}$C and -5 $^{\circ}$C, respectively. This increase in ice formation temperature happened in the condition that

cooling rates were almost constant. This fact is shown in the pressure-temperature graphs in Fig. 31. The results showed that ice formed at higher temperatures when the experiments were repeated several times.

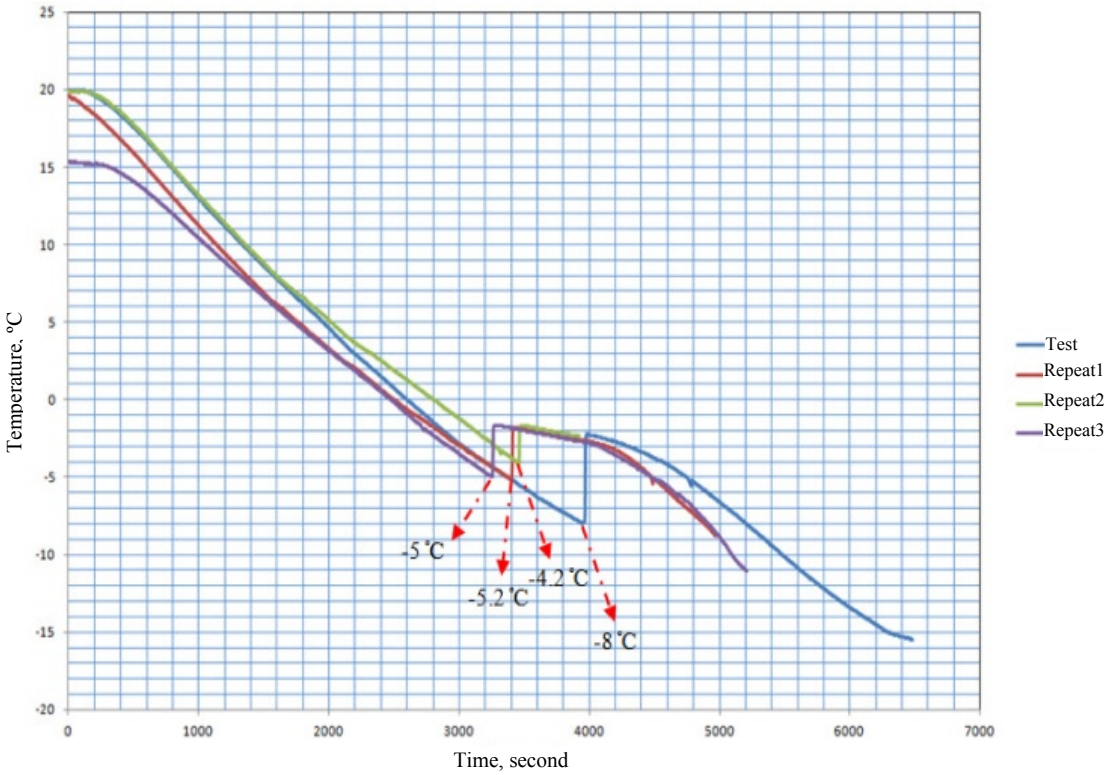

Fig. 31 The graphs of temperature versus time for the pure water-pure methane system with the initial pressure of 2000 psi.

This concept is especially important in the study of the formation of ice and gas hydrate in pipelines as well as around a wellbore in gas hydrate bearing sediments [42, 43, 44, 46, 47]. The temperature changes could cause the ice and gas hydrate to melt and

form several times in those conditions. This repetitive formation and melting of ice and gas hydrate could create a condition in which ice and gas hydrate form at even higher temperatures and lower pressure conditions.

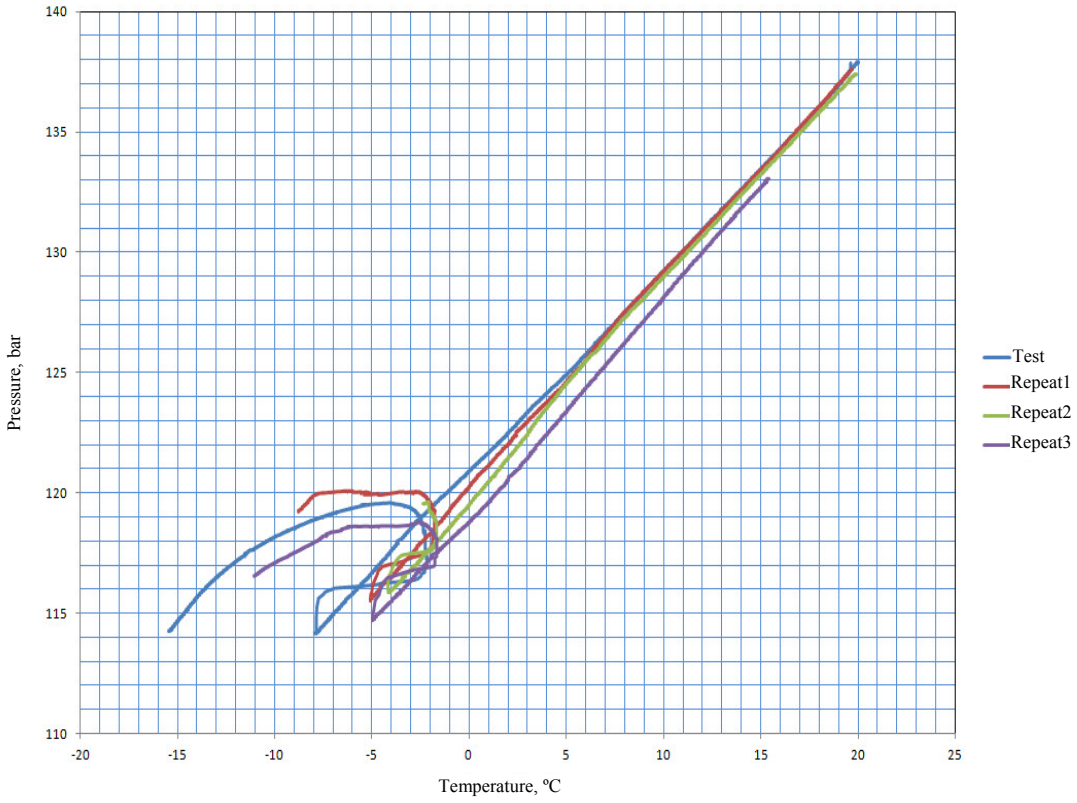

Fig. 32 The graphs of temperature versus time for pure water-pure methane system with the initial pressure of 2000 psi.

After the formation of gas hydrate and ice in the cell, the temperature was increased with a constant rate to melt both gas hydrate and ice phases. Typical heating curves for the ice and gas hydrate melting experiments in the pure gas-pure water system

with the initial pressure of 1500 psi are shown in Fig. 32. As seen in Fig. 32, the heating curve in the ice and gas hydrate melting experiments can be divided into the three following areas. The first area is the linear section related to the expansion of ice, gas hydrate and gas phases.

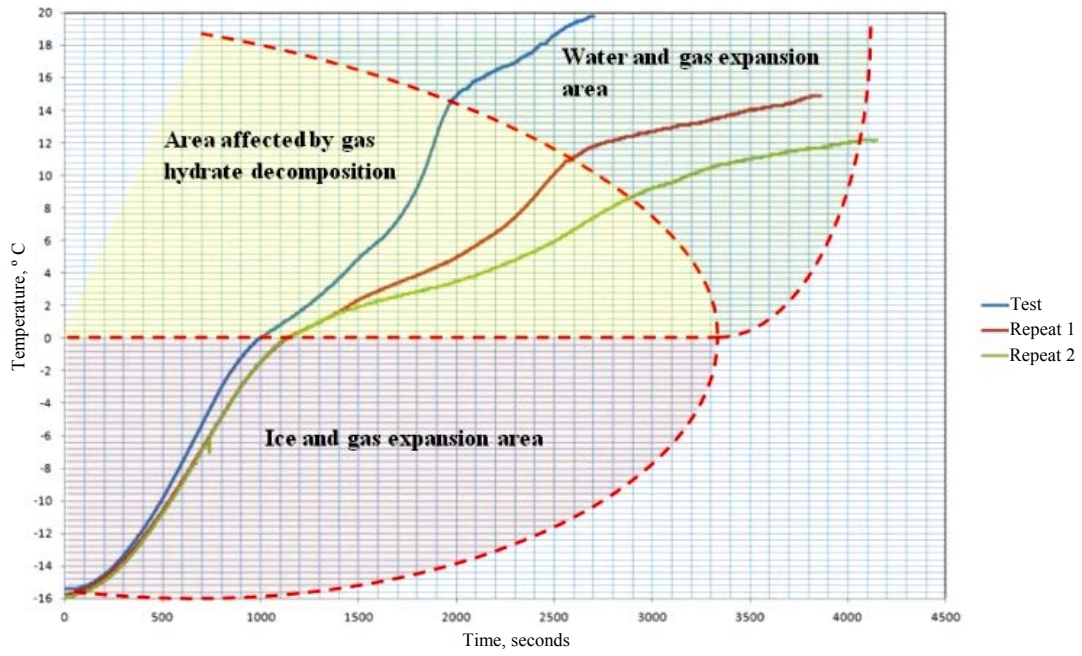

Fig. 33 Temperature-time curves for heating experiments in pure water-pure gas system. The different sections of heating curve are highlighted in the graph.

This area was a subzero temperature region, there was no phase transformation, and the heating power of the refrigerator was constant. Consequently, the temperature increased linearly with time. The second area is the area affected by ice and gas hydrate decomposition. This region started at 0 °C at which of ice begins to melt. With an

increase in temperature, the gas hydrate phase started to decompose and adsorb heat from its surrounding environment because of the endothermic nature of gas hydrate decomposition. The temperature-time curve is nonlinear in this area due to phase transformation. The third section is the linear area, which is related to the water and gas expansion**.** After the decomposition of gas hydrate phase, the cell contained only water and methane gas. Therefore, with increase in temperature, water and methane gas expanded and showed a linear increase in temperature versus time.

As seen in Fig. 32, the temperature increase rate in the experiments with fresh water is greater than the temperature increase rate in the repeated tests. A possible explanation is that after several decompositions of gas hydrate, some residual gas hydrate structures remain in the water, which cause additional formation of gas hydrate in the cell when the tests were repeated. This process is called memory effect in gas hydrate formation [3]. Therefore, in each repeat of the test more gas hydrate forms and gas hydrate volume increases during the decomposition process. The higher volume of gas hydrate causes more heat absorption during the decomposition process and bends the heating curve downward, as is seen in Fig. 32.

4. STRESSES AROUND A PRODUCTION WELL IN GAS HYDRATE-BEARING FORMATION

4.1. Introduction

The knowledge of stress and strain distribution around the wellbore during production is needed to assess the problems like wellbore stability and potential for sand production. Different researchers addressed the problem of stress and strain distribution around wellbore with different approaches. Freij-Ayoub *et al.* [48] used FLAC to numerically calculate stress and strain distribution around the wellbore induced drilling through gas hydrate bearing strata. Rutqvist *et al.* [49] used TOUGH+HYDRATE to numerically simulate pressure and temperature distribution around the wellbore induced by different thermal and mechanical conditions during gas hydrate dissociation. Then, FLAC3D was used to calculate stress distribution around the wellbore. Kimoto *et al.* [50], on the other hand, treated hydrate bearing reservoir as a chemo–thermo–mechanical material and used an elasto–viscoplastic model to address plastic deformations in the soil during gas hydrate production. However, the selection of appropriate model to simulate the condition of stress and strain around the wellbore is greatly affected by the geology of reservoir as well as the condition of production from the reservoir. Waite *et al.* [51] pointed out that gas hydrate accumulations in coarse grain sands are more prone to plastic deformation and sand production during production period than fine grain hydrate sediments.

The selection between a poroelastic or poroplastic model is related to the gas production rate and whether the gas hydrates bear loads in the reservoir or merely fill the

voids in the pore space. In this paper, it is assumed that the reservoir remains elastic during gas production period. In addition, the intrinsic permeability of rock remains the same despite the change in gas effective permeability in non-decomposed and decomposed zones. It is assumed that the fluid flow is single phase flow i.e. gas flow, and water remains stagnant in the reservoir [3]. A poroelstic model is used as a semi-analytical method to calculate the induced total stress in gas hydrate reservoir during gas production.

4.2. Mathematical Models

For calculation of induced stress and strain in gas hydrate reservoir during production, we need to know the pressure and temperature distribution in the reservoir during decomposition of hydrate layer. For this purpose, we utilize and expand the approach described in [3]. The area around a wellbore can be viewed as two parts, one corresponding to the decomposed region and the other the non-decomposed gas hydrate layers. The schematic of these layers is shown in Fig. 33.

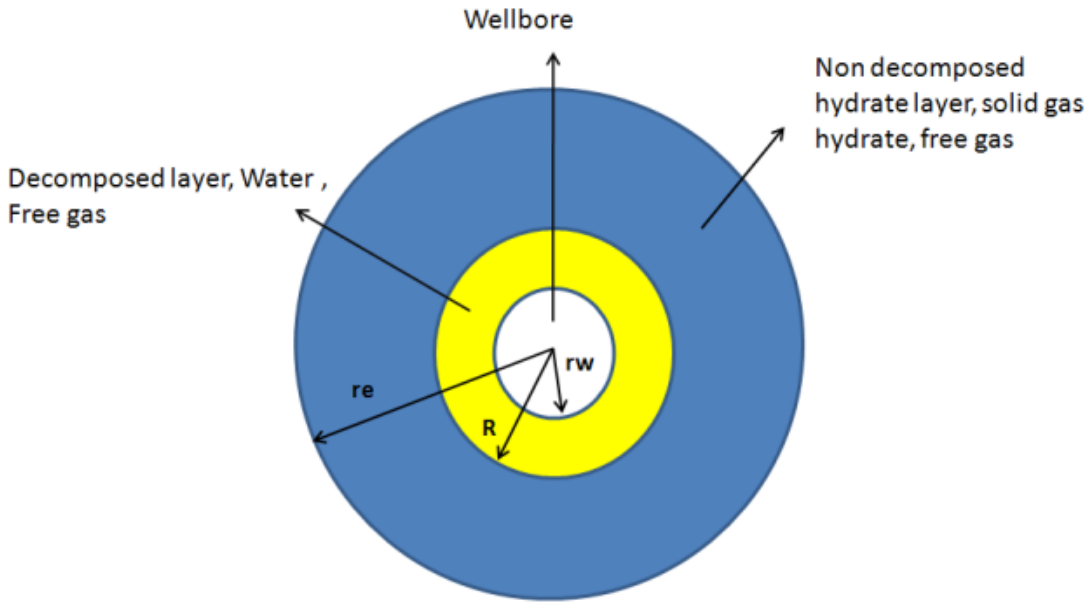

Fig. 34 Different zones during gas production, r_w is wellbore radius, R is the radius of gas hydrate decomposing front and re is reservoir radius.

During gas production, the diameter of decomposed layer, R, will grow with time. The movement of the boundary between the two areas introduces a physical problem with free moving boundary condition which is called Stefan problem named after Jožef Stefan, the Slovene physicist who studied the problems of ice formation around 1890 [52]. Stefan's problems include at least two differential equations with their own boundary conditions which are related together through Stefan's condition. The mathematical model of gas hydrate production as well as the resulted strain and stress field around the wellbore are discussed in following sections. In the following section,

we elaborate on the method introduced by Makogon *et al.* [3] to calculate temperature and pressure distribution during gas production from gas hydrate bearing reservoir.

4.2.1. Pressure Distribution

The governing equation for pressure distribution around the wellbore during gas hydrate production is gas diffusivity equation in polar coordinates [3, 53]:

$$\frac{k_n}{2m_n\mu}\left(\frac{\partial^2 P_n^2}{\partial r^2}+\frac{1}{r}\frac{\partial P_n^2}{\partial r}\right)=\frac{\partial P_n}{\partial t} \tag{4.1}$$

where *n* is equals 1 for decomposed gas hydrate layer zone and is 2 for non-decomposed zone. Also P is the pore pressure and k is permeability to gas, μ is gas viscosity, s is water saturation, β is hydrate saturation, phi is porosity in both decomposed and non-decomposed layer.

In addition,

$$m_1=(1-s)\times m \tag{4.2}$$

$$m_2=(1-\beta)\times m \tag{4.3}$$

The above equation is nonlinear and can be linearized with respect to P in order to be solved analytically. For the linearization of gas diffusivity equation, we consider following approximations [3, 53].

$$\frac{1}{2P_D}\frac{\partial^2 P_1^2}{\partial t}=\frac{\partial P_1}{\partial t} \tag{4.4}$$

$$\frac{1}{2P_e}\frac{\partial^2 P_2^2}{\partial t}=\frac{\partial P_2}{\partial t} \tag{4.5}$$

where P_e is the reservoir initial pressure in MPa and P_D, MPa, is equilibrium pressure at the interface between decomposed and non-decomposed layers. After linearization, we will obtain the following equations:

$$(\frac{\partial^2 P_n^2}{\partial r^2} + \frac{1}{r}\frac{\partial P_n^2}{\partial r}) = \frac{1}{\chi_n}\frac{\partial P_n^2}{\partial t} \tag{4.6}$$

where

$$\chi_1 = \frac{k_1 P_D}{\mu\, m_1} \tag{4.7}$$

$$\chi_2 = \frac{k_2 P_e}{\mu\, m_2} \tag{4.8}$$

The boundary conditions for diffusivity equations are:

- Constant production rate, Q
- $P_2(r, 0) = P_2(\infty, t) = P_e$
- $P_1(R(t), t) = P_2(R(t), t) = P_D$

where r_w is wellbore radius in meter, P_W is wellbore pressure, R(t) is the radius of the interface between the decomposed and un-decomposed layer. The solutions of linearized gas diffusivity equation are [3, 53]:

$$P_1^2 = P_D^2 - \frac{Q\mu P_0}{\pi k_1 h \rho_0}[Ei\left(-\lambda_1^2\right) - Ei(-\alpha_1^2)] \tag{4.9}$$

$$P_2^2 = P_e^2 + (P_D^2 - P_e^2)[\frac{Ei(-\lambda_1^2)}{Ei(-\alpha_1^2)}] \tag{4.10}$$

The functions and coefficients in Eq. (4.9) and (4.10) are [3]:

$$Ei(-\alpha) = -\int_{\alpha}^{\infty} \frac{e^{-u}}{u} du, \;\; \alpha > 0 \tag{4.11}$$

$$\lambda_1^2 = \frac{r^2}{4t\chi_1} \tag{4.12}$$

$$\lambda_2^2 = \frac{r^2}{4t\chi_2} \tag{4.13}$$

$$\alpha_1^2 = \frac{\gamma}{4\chi_1} \tag{4.14}$$

$$\alpha_2^2 = \frac{\gamma}{4\chi_2} \tag{4.15}$$

In Eq. (4.9) to (4.15), we have:

- Q: production rate of methane gas per unit length of well
- $\rho_{0:}$ density of methane gas at atmospheric pressure P_0 and temperature T_0. (0.706 kg/m3)
- P_0 : atmospheric pressure (0.101 MPa)
- h: is unit length of pay zone(1 m)
- γ: constant which determines movement velocity of dissociation front (m^2/s)
- T_e :reservoir temperature at initial time (K)

4.2.2. Temperature Distribution

To consider the effect of temperature changes on induced stress in a gas hydrate reservoir, heat transfer equation need to be considered. The governing equation for heat transfer in the reservoir is considered to be conductive-convective heat transfer equation which could be written as [3, 53]:

$$\frac{a_n}{r}\frac{\partial}{\partial r}\left(r\frac{\partial T_n}{\partial r}\right)=\frac{\partial T_n}{\partial t}-\frac{c_v k_n}{c_n \mu}\frac{\partial P_n}{\partial r}\left(\frac{\partial T_n}{\partial r}-\delta\frac{\partial P_n}{\partial r}\right)-\eta\frac{m_n c_v}{c_n}\frac{\partial P_n}{\partial t} \quad (4.16)$$

where:

- n=1 and 2 for decomposed and non-decomposed layer respectfully
- T_1: Temperature in decomposed layer (K)
- T_2: Temperature in non-decomposed layer (K)
- a_n: thermal conductivity of zones 1 and 2 (m^2/s)
- c_v: volume heat capacity of gas (J/K.kg)
- c_1: heat capacity of zone 1 (J/K.kg)
- c_2: heat capacity of zone 2 (J/K.kg)
- η: adiabatic coefficient of gas (K/Pa)
- δ: throttling coefficient of gas (K/Pa)

Note that the Joule-Thompson cooling process is considered in the above equations. In order to solve the problem analytically, we assume conduction heat transfer is negligible in gas hydrate reservoir in comparison to convection heat transfer. So we let:

$a_n = 0$

and obtain:

$$\frac{\partial T_n}{\partial t}=\frac{c_v k_n}{c_n \mu}\frac{\partial P_n}{\partial r}\left(\frac{\partial T_n}{\partial r}-\delta\frac{\partial P_n}{\partial r}\right)+\eta\frac{m_n c_v}{c_n}\frac{\partial P_n}{\partial t} \quad (4.17)$$

In addition to mentioned pressure boundary and initial conditions, the following boundary conditions for Eq. (104):

- $T_1(r, 0) = T_2(r, 0) = T_2(\infty, t) = T_e$
- $T_1(R(t), t) = T_2(R(t), t) = T_D$

The solutions of above conductive-convective heat transfer equations are [3]:

$$T_1 = T_D + A_1[Ei(-\lambda_1^2) + (1+Q_1)Ei\left(-\lambda_1^2 - B_1 e^{-\lambda_1^2}\right) - Ei(-\alpha_1^2) - (1+Q_1)Ei\left(-\alpha_1^2 - B_1 e^{-\alpha_1^2}\right)] \quad (4.18)$$

$$T_2 = T_e + A_2[Ei(-\lambda_2^2) + (1+Q_2)Ei\left(-\lambda_2^2 - B_2 e^{-\lambda_2^2}\right)] \quad (4.19)$$

where

$$A_1 = \frac{Q\mu\delta P_0}{2\pi h k_1 P_D \rho_0} \quad (4.20)$$

$$A_2 = \frac{\delta(P_D^2 - P_e^2)}{2P_D Ei(-\alpha_1^2)} \quad (4.21)$$

$$B_1 = \frac{Q}{\pi h \chi_1}\frac{c_v}{c_1} \quad (4.22)$$

$$B_2 = \frac{k_2}{\mu\chi_2}\frac{c_v}{P_0 c_2}\frac{(P_D^2 - P_e^2)}{Ei(-\alpha_2^2)} \quad (4.23)$$

$$Q_1 = \frac{\eta}{\delta}\frac{m_1 c_v}{c_1}\frac{P_D}{P_0} \quad (4.24)$$

$$Q_2 = \frac{\eta}{\delta}\frac{m_2 c_v}{c_2}\frac{P_D}{P_0} \quad (4.25)$$

In the pressure and temperature solutions, the temperature at the gas hydrate decomposition front, T_D, the pressure at the interface, P_D, and the boundary velocity constant, γ, are unknown. They should be solved in order to find the pressure and temperature solutions around the wellbore. Noting that the T_D satisfies Eq. (4.18) and (4.19), we replace T_2 by T_D in Eq. (4.18) and obtain:

$$T_D = T_e + A_2[Ei(-\alpha_2^2) + (1 + Q_2) \times Ei\left(-\alpha_2^2 - B_2 e^{-\alpha_2^2}\right)] \quad (4.26)$$

Furthermore, if T_D is substituted into Eq. (4.19), we get $T_D = T_D$ which is not useful. Similarly, if P_D is put instead P_1 and P_2 in Eq. (4.9) and (4.10), it results in $P_D = P_D$. Therefore, we need to use the Stan's condition to have a second equation to solve for T_D, P_D and γ. If mass and energy conservation are considered at the interface of decomposed and intact zones, we get following equation [3]:

$$k_1 \frac{\partial P_1(R,t)}{\partial t} - k_2 \frac{\partial P_2(R,t)}{\partial t} = \left[\epsilon\beta z \frac{\rho_3}{\rho_0}\frac{T_D}{T_0}\frac{P_0}{P_D} - (\beta - \sigma)\right] m\mu \frac{dR}{dt} \quad (4.27)$$

where z is the compressibility factor of gas, and ρ_3 is the density of hydrate. R is the radius of decomposing front in meter which could be calculated according to following equation:

$$R = \sqrt{\gamma t} \quad (4.28)$$

where, t is time (sec). Now, if pressure boundary conditions are substituted into Eq. (4.27), after derivations and simplification, we will get following equation:

$$\frac{Q\mu P_0}{\pi h \rho_0} e^{-\alpha_1^2} + k_2(P_e^2 - P_D^2)\frac{e^{-\alpha_2^2}}{Ei(-\alpha_2^2)} = (\beta\epsilon \frac{\rho_3}{\rho_0}\frac{T_D}{T_0} P_0 z - (\beta - \sigma)P_D)\, \chi_1 \mu m \alpha_1 \quad (4.29)$$

The third equation is an empirical correlation between equilibrium temperature and pressure of methane hydrate formation is [3, 53].

$$\log_{10} P_D = a(T_D - T_0) + b(T_D - T_0)^2 + c \quad (4.30)$$

where:

- a = 0.0342 K^{-1}
- b = 0.0005 K^{-2}

- c = 6.4804

For finding the unknowns, we need to solve the system of nonlinear Eq. of (4.27), (4.29) and (4.30). After finding T_D, P_D and γ, we use them in pressure and temperature solutions to find the pressure and temperature solutions around the wellbore.

4.2.3. Induced Stress Distribution

On the basis of linear coupled thermo-poroelasticity theory, the strain distribution around the wellbore caused by changes in pore pressure and temperature can be calculated by the following expression (e.g., Tao and Ghassemi [54, 55])

$$\sigma_{rr} = -\frac{2\eta}{r^2}\int_{r_w}^{r} Prdr - \frac{2\eta K\alpha_m}{\alpha r^2}\int_{r_w}^{r} Trdr \tag{4.17}$$

Also the tangential strain is given

$$\sigma_{\theta\theta} = \frac{2\eta}{r^2}\int_{r_w}^{r} Prdr + \frac{2\eta K\alpha_m}{r^2\alpha}\int_{r_w}^{r} Trdr - 2\eta P - \frac{2\eta K\alpha_m}{\alpha}T \tag{4.32}$$

where η is the poroelastic stress coefficient and is equal to:

$$\eta = \frac{(1-2\nu)\alpha}{2(\nu-1)} \tag{4.33}$$

Where:

α: Biot's coefficient

ν: Poisson's ratio

G: Shear modulus, MPa

K: Bulk modulus, MPa

α_m: The thermal expansion coefficient of rock, K^{-1}

Also, P and T are changes in pressures and temperatures from their initial state and are defined by:

$$P = Pe - Pi \tag{4.34}$$

$$T = Te - Ti \tag{4.35}$$

The strains can then be used in the constitutive equations to calculate the stresses. As it is shown in Fig. 3, the maximum temperature change during production is 4.3 K. The amount of induced stress in reservoir caused by this temperature change is small in comparison with induced stress by pressure change and is therefore, neglected. In this way, the assumption of formation homogeneity can be maintained. Ignoring the temperature terms, Eq. (4.31) and (4.32) are used to find the stresses:

$$\sigma_{rr} = -\frac{2\eta}{r^2}\int_{r_w}^{r} Prdr \tag{4.36}$$

and the tangential stress is:

$$\sigma_{\theta\theta} = \frac{2\eta}{r^2}\int_{r_w}^{r} Prdr - 2\eta \times P \tag{4.37}$$

The sign convention is tension positive. Now, by substituting the pressure functions into Eq. (4.36) and (4.37) the induced stress around the wellbore can be calculated. Since there is no analytical way to calculate the $\int_{r_w}^{r} Prdr$ integral, they are calculated numerically. In this section the results for the calculation of pressure and

temperature distribution as well as related induced stress and strain in the gas hydrate reservoir are presented. The main assumption in this study is that the gas production rate is constant.

4.3. Results and Discussion

In this section the results for the calculation of pressure and temperature distribution as well as related induced stress and strain in the gas hydrate reservoir are presented. The main assumption in this study is that the gas production rate is constant. Other assumption is that mechanical behavior of reservoir remains elastic. For coefficients and mentioned parameters in the paper, a hypothetical case of gas hydrate reservoir is considered with the parameters same as those in Ji *et al.* [53] and Freji-Ayoub [48]. These parameters are mentioned in Table 5. In this study, the effect of production time and gas production rate on pressure, temperature, strain and stress distribution in reservoir were investigated. The wellbore radius, r_w, is assumed to be 0.13 m. For all the calculations, the initial reservoir pressure, P_i, and initial reservoir temperature, T_i, are considered to be 15 MPa and 287 K, respectively. Also, the permeability in decomposed layer is $k_1= 5.2\times10^{-15}$ m^2 (5.2 md) and in the non-decomposed hydrate layer is $k_2= 0.4\times10^{-15}$ m^2 (0.4 md). Other gas properties like viscosity and permeability are assumed to be constant. This seems to be reasonable assumption for low temperature and fairly low pressure gas hydrate reservoirs. A Mathematica code was written to do all the necessary calculation.

Table 5 The parameters for the calculation of stresses around the producing wellbore.

Parameter	Value	Ref.
α: Biot's coefficient	1	90
α_m: The thermal expansion coefficient of rock, K^{-1}	7.7×10^{-5}	90
β: hydrate saturation, %	0.15	95
δ: throttling coefficient of gas (K/Pa)	8×10^{-7}	95
η: adiabatic coefficient of gas (K/Pa)	3.2×10^{-6}	95
μ: gas viscosity, Pa.s	1.5×10^{-5}	95
ν: Poisson's ratio	0.45	90
σ: water saturation, %	0.15	95
c_1: heat capacity of zone 1 (J/K.kg)	2400.2	95
c_2: heat capacity of zone 2 (J/K.kg)	1030.2	95
c_v: volume heat capacity of gas (J/K.kg)	3000	95
$\rho_{0:}$ density of methane gas at P_0 and T_0, kg/m3	0.706	95
$\rho_{3:}$density of hydrate, kg/m3	0.91×10^3	95
$\rho_{w:}$ density of water, kg/m3	1×10^3	95
G: Shear modulus, MPa	650	90
k_1: gas permeability in zone 1, md	5.2	95
K_2: gas permeability in zone 2, md	0.4	95

Table 5 Continued.

K: Bulk modulus, MPa	7000	90
P_0 : atmospheric pressure, MPa	0.101	95
T_0 : atmospheric temperature,	273.15	95
m: porosity, %	0.19	95
z: compressibility of gas	0.88	95
Cohesion, c, MPa	1.8	90
Angle of internal friction, φ, °	35	90

4.4.1. The Effect of Production Time

Consider the constant gas production rate of 0.04 kg/second, production times are considered to be 120, 365, 100 and 730, 1460 and 2920 days (0.33, 1, 2, 4 and 8 years, respectively). The effect of production time on pressure and temperature around the wellbore are shown in Fig. 34 and 35. As shown in Fig. 34, there are two different zones of pressure in the gas hydrate on either sides of gas hydrate decomposing front.

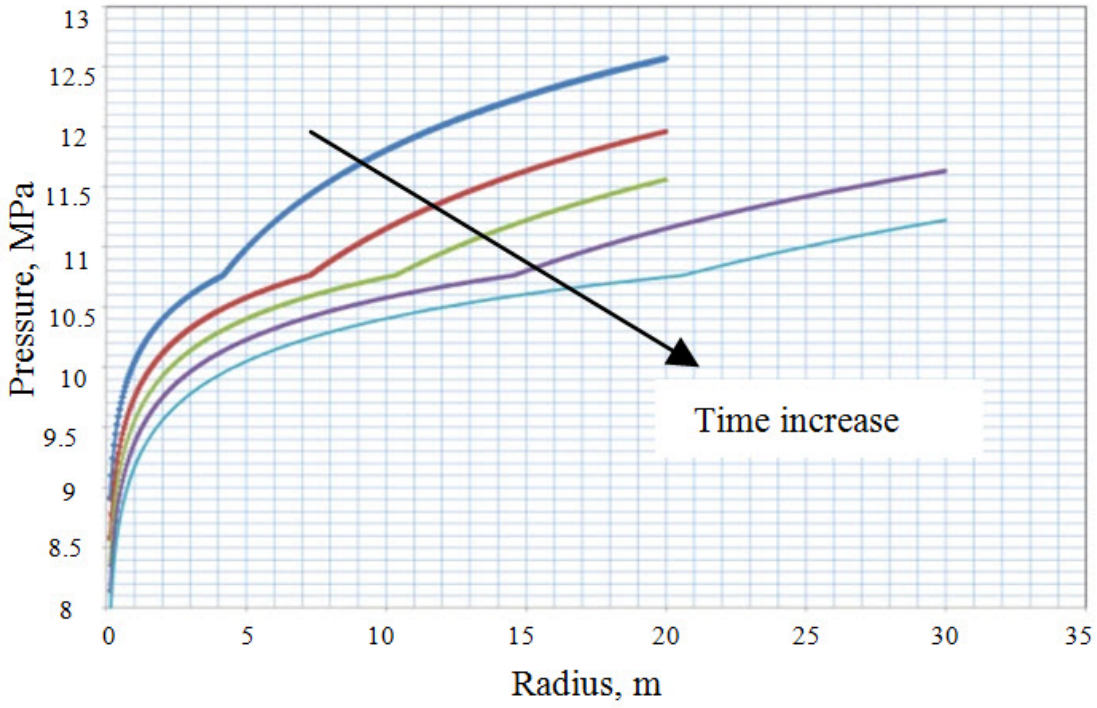

Fig. 35 The effect of production time on pressure distribution around the wellbore.

The position of the decomposition front coincides with a bump in pressure and temperature graphs. The bump is caused by considerable permeability difference on either sides of the front. The lower effective permeability in the non-decomposed gas hydrate layer corresponds to less pressure drop at constant production rate. In contrast, the considerable higher effective gas permeability in the decomposed layer caused sharper pressure drop. Fig. 35 shows the temperature distribution in the reservoir in different production times. Like pressure graphs in Fig. 34, there is a temperature bump at the location of decomposition front because of this fact that two different partial differential equations stated at Eq. (4.17) represents the physics of problem at either

sides of the front. In the decomposed layer near the wellbore, there is more pressure drops and therefore higher velocity which causes higher temperature decrease due to higher convective heat transfer and stronger cooling Joule-Thompson effect. Also, similar to the effect of production time on pressure distribution, the overall temperature in the reservoir decreases with increase in production time.

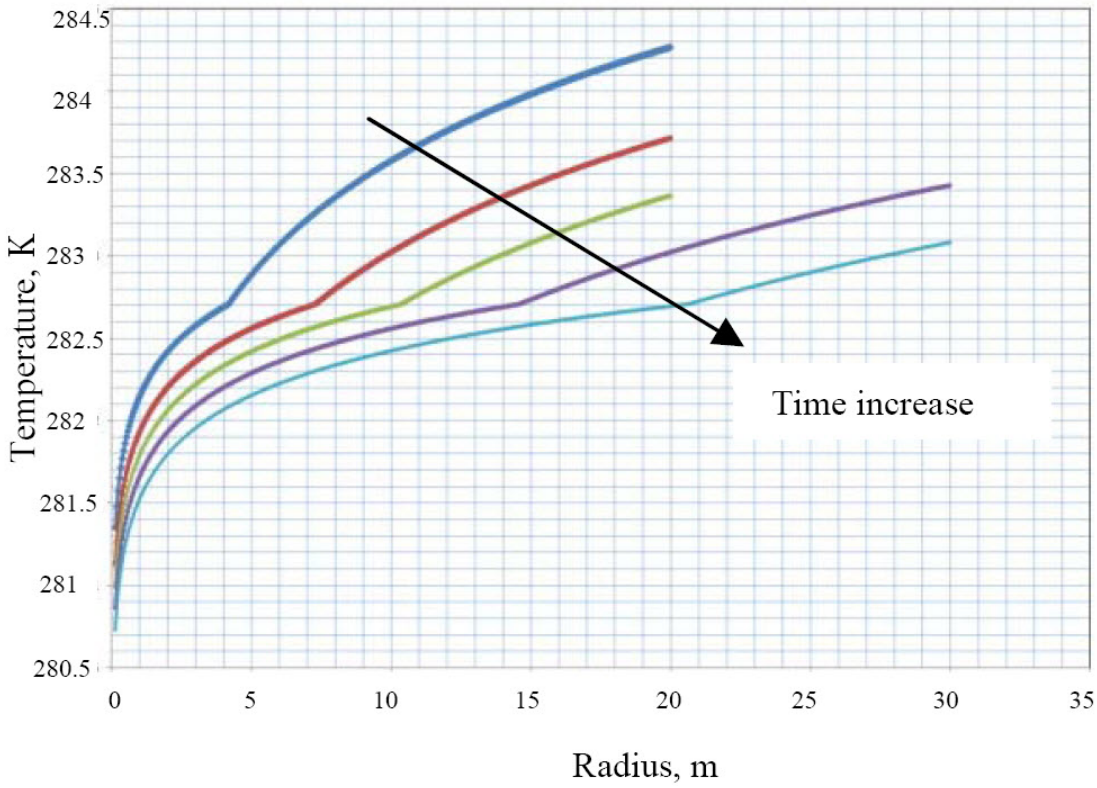

Fig. 36 The effect of production time on temperature distribution around the wellbore.

The effect of production time on radial stress is shown in Fig. 36. The type of induced stress here is tensional stress. As shown in the Fig. 36, the radial stress is zero at the wellbore radius and then increases to a maximum near the wellbore. The induced radial tensile stress increases with increase in time due to increase in induced pressure and temperature.

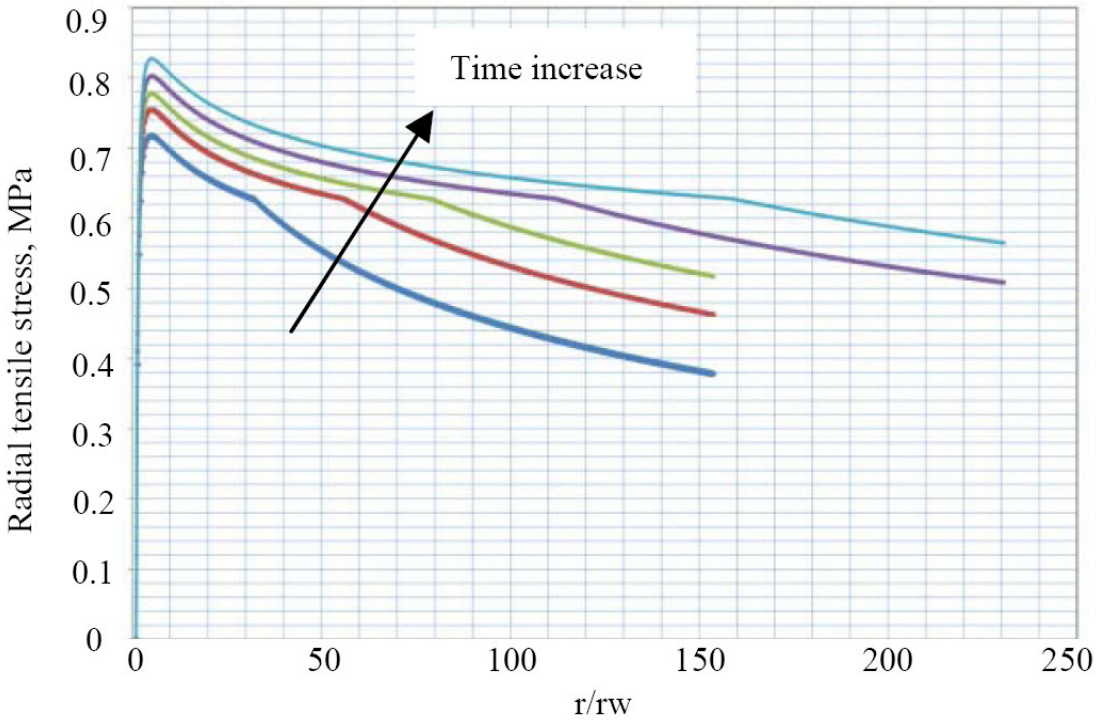

Fig. 37 The effect of production time on induced radial stress field, σ_{rr}, around the wellbore.

Also, the effect of production time on tangential stress is shown in Fig. 37. The type of induced tangential stress here is compressive stress. The maximum of induced tangential stress occurs in the wellbore wall and then decreases with increase in radius. Like induced radial stress, tangential stress increase with increase in production time.

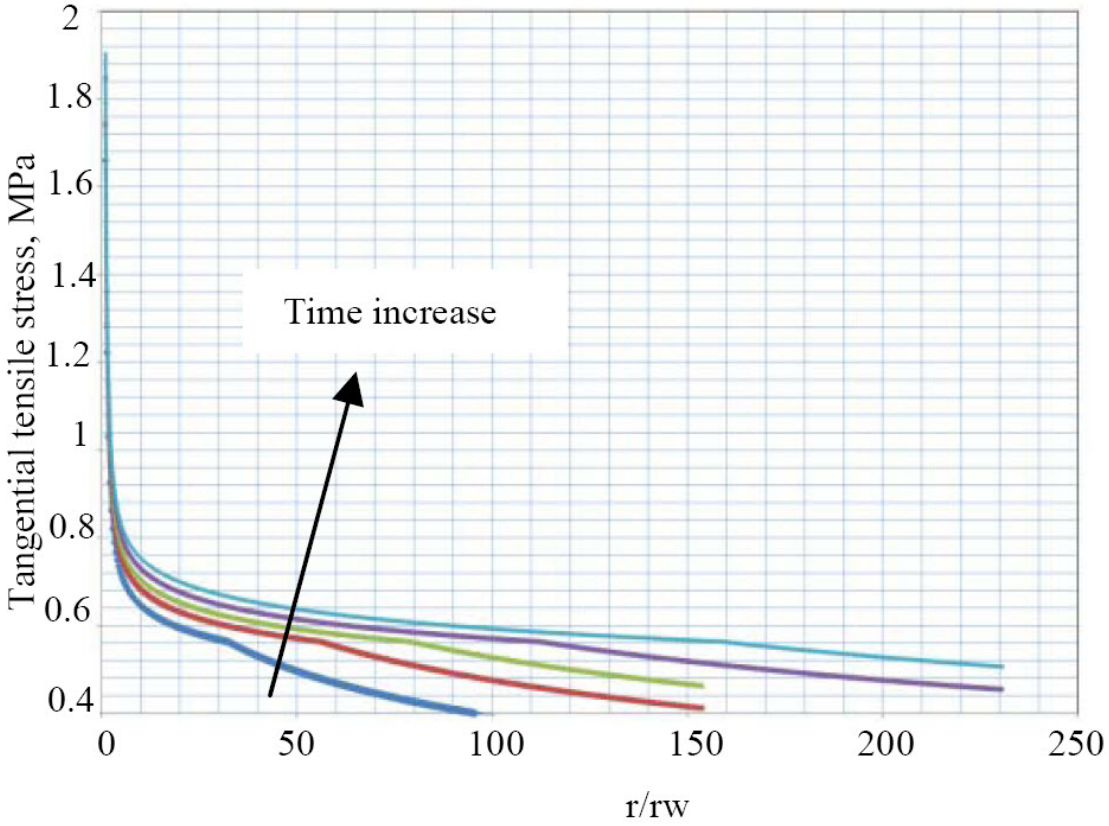

Fig. 38 The effect of production time on induced tangential stress field, $\sigma_{\Theta\Theta}$, around the wellbore.

4.4.2. The Effect of Production Rate

The effect of gas production rate on induced stress distribution in the reservoir during production period is studied at a time of 365 days. Different production rates of 0.04, 0.06, 0.08, 0.1 and 0.12 Kg of gas per second are considered. Fig. 38, shows the effect of production rate on induced radial stress in the reservoir. The type of radial strain is tensional strain. As shown in Fig. 38, increase in production rate causes the increase of induced radial stress due to increase in induced pressure and temperature in reservoir. The effect of increase in production rate on induced radial stress is shown in Fig. 37. The type stress here is compressional stress.

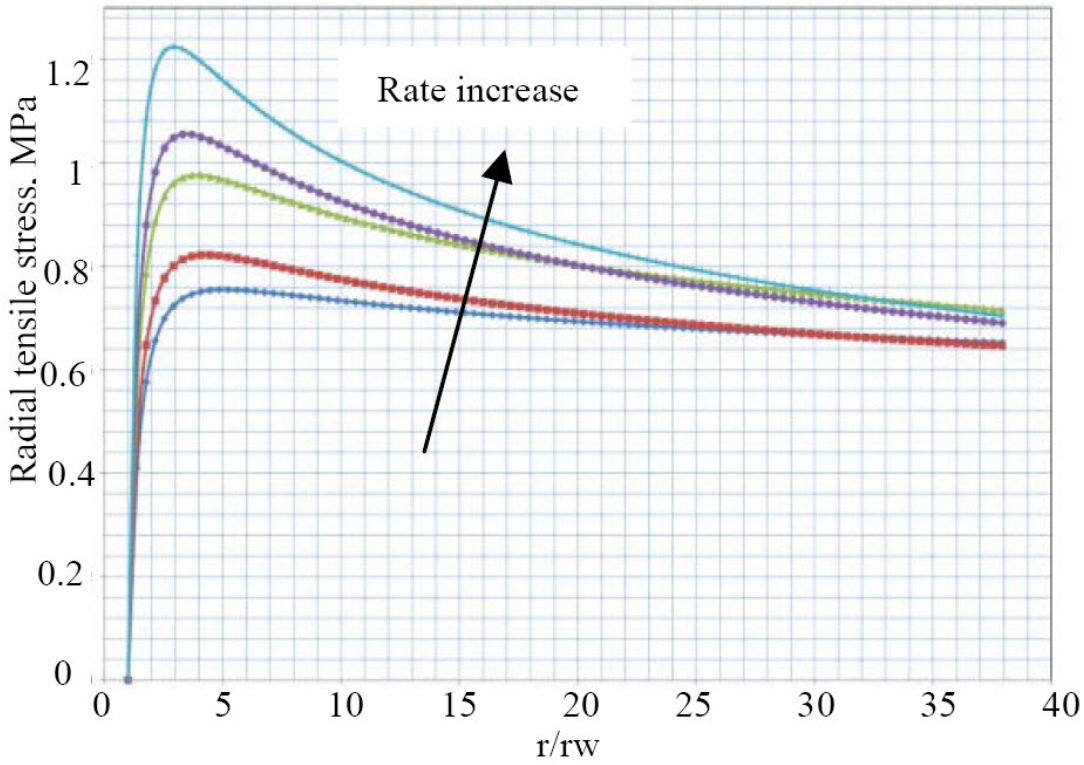

Fig. 39 The effect of gas production rate on induced radial stress field, σ_{rr}, around the wellbore.

The induced radial stress is zero in the wellbore and then increases to a maximum near the wellbore. The induced radial stress vanishes with increase in radius. Finally as it is shown in Fig. 38, the increase in production rate causes increase in induced tangential stress in the reservoir. As observed from the radial and tangential stress results, the highest amount of stresses is induced around the wellbore. The induced tangential stresses are maximum at the wellbore wall and radial stress reaches the maximum value near the wellbore because there is the maximum pressure drop around

the wellbore. Consequently, the area near the wellbore is the most prone to failure during gas production.

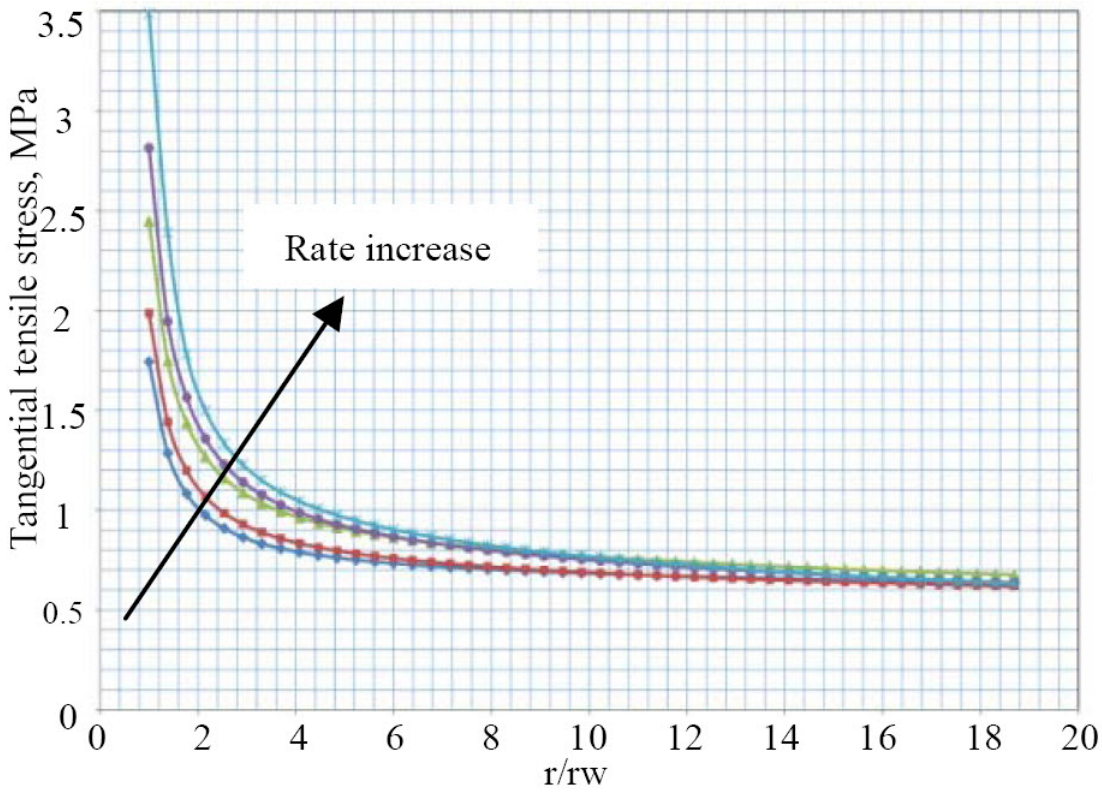

Fig. 40 The effect of gas production rate on induced tangential stress field, $\sigma_{\Theta\Theta}$, around the wellbore.

We consider an offshore gas hydrate deposit at 1450 m depth from the ocean surface (1000 m of water and 450 m of rock). With hydrostatic pressure gradient equal to 0.01035 psi/ft, the pore pressure is 15 MPa which is set to the initial reservoir pressure. The vertical stress in the reservoir is 20.53 MPa considering the geostatic pressure gradient of 0.022633 MPa/m. The horizontal stress is calculated using:

$$\sigma_H = \frac{\vartheta}{1-\vartheta}(\sigma_V - \alpha \times p) + \alpha \times p \tag{4.38}$$

Where σ_H is horizontal stress, σ_V is vertical stress, α is Biot's effective stress coefficient, ϑ is Poisson's ratio and p is pore pressure. Because of the absence of tectonic stresses, the horizontal stresses in all direction are the same. Assuming a Poisson's ratio of 0.45 and α of 1, the horizontal stress in the gas hydrate deposit equals 19.52 MPa. For understanding the wellbore stability situation in the hydrate bearing reservoir, the stress state around the wellbore needs to be considered. The stress situation around the wellbore could be found by adding the stresses caused by the far-field mean stress, the pore pressure change and the far field deviatoric stress. The stress induced by pore pressure is already calculated by formulas 36 and 37. Since $\sigma_h = \sigma_H$, the mean stress is equal to the horizontal stress or 19.52 MPa. The wellbore pressure, P_w, is equal to 1.32 MPa. Therefore at the wellbore periphery, we have a $\sigma_{\theta\theta} = -18.2$ MPa caused by the pore pressure loading.

The maximum observed induced tangential tensile stress at wellbore periphery during gas production is 3.45 MPa at the production rate of 0.12 Kg of gas per second. Therefore, the total stress situation at the wellbore is $\sigma_{rr}^{Total} = P_W = -1.32$ MPa and $\sigma_{\theta\theta}^{Total} = -34.25$ MPa. Then, the Mohr-Coulomb failure criterion is used to assess the failure condition around the well. Assuming a cohesion of c= 1.8 MPa and a fraction angle φ= 35°, the maximum allowable stress level is -6.92 MPa and failure is predicted.

5. CONCLUSION

1. A model was developed to calculate the moles of consumed or generated gas, and the volume of gas hydrate in a closed cell during gas hydrate formation and decomposition experiments.
2. The gas hydrate formation experiments showed that the increase of the subcooling from 0.2°C to 4.6°C and the initial pressure from 2000 psi to 2500 psi caused gas hydrate formation at higher rates.
3. In all ice and gas hydrate formation experiments using a cooling rate of 0.45 °C/min, the ice and gas hydrate started to form at temperatures in the range of -8±0.2°C, indicating that neither initial pressure nor chemical composition of water has a considerable effect on the ice and gas hydrate formation temperatures. However, a change in cooling rate from 0.45 to 0.6°C/min decreased ice and gas hydrate formation temperature from -8°C to -9°C.
4. In ice and gas hydrate formation experiments using a constant cooling rate of 0.45 °C/min, the formation temperature increased from -8°C to a range of temperature between -4.2°C to -5.2°C during consecutive gas hydrate and ice forming and melting cycles.
5. A semi-analytical model was derived for the calculation of induced stresses around a producing well in a gas hydrate reservoir. Gas production rates between 0.04 to 0.12 Kg of gas per second and production times between 0.33 to 8 years were considered. The results of the modeling showed that increases in production time and production rate induced greater radial and tangential stresses around the wellbore.

REFERENCES

[1] Sloan E D, Koh C A. Clathrate hydrates of natural gas. 3rd ed. CRC Press. Boca Raton. FL; 2009.

[2] Makogon Y F, Holditch S A. Gas solubility in water, kinetics and morphology of gas hydrate. Annual Report for Arco Exploration and Production Technology. Texas A&M University; 1998.

[3] Makogon Yuri F. Hydrates of hydrocarbons. Pennwell Books. Tulsa. OK; 1997.

[4] Berecz E, Balla-Aches M. Gas hydrates, studies in inorganic chemistry. Akademia Kiado, Budapest; 1983.

[5] Editorial. An introduction to natural gas hydrate/clatherate: the major organic carbon reserve on earth. Journal of Petroleum Science and Engineering 2007;56: 1–8.

[6] Jeffrey G A. Inclusion compounds. Academic Press. London; 1984.

[7] Milkov Alexei V. Global estimates of hydrate-bound gas in marine sediments: how much is really out there. Earth-Science Reviews 2004; 66:183–197.

[8] Nordpil. http://nordpil.com/go/portfolio/mapsgraphics/cryosphere/; 2009.

[9] USGS. http://geology.usgs.gov/connections/mms/joint_projects/methane.htm; 2009.

[10] Max Michael D. Johnson Arthur H., Dillon William P. Economic geology of gas hydrate. Springer, Berlin; 2006.

[11] Daraboina N, Linga P, Ripmeester J, Walker Virginia K, and Englezos P. Natural gas hydrate formation and decomposition in the presence of kinetic inhibitors. 2. stirred reactor experiments. Energy & Fuel; 2011: A-H.

[12] Vysniauskas A, Bishnoi P R, A kinetic study of methane hydrate formation. Chemical Engineering Science 1983; 38:1061-1072.

[13] Englezos P, Kalogerakis N, Dholabhai P D, Bishnoi P R. Kinetics of formation of methane and ethane gas hydrates. Chem Eng Sci 1987; 42: 2647–2658.

[14] Englezos P, Kalogerakis N, Dholabhai P D, Bishnoi P R. Kinetics of gas hydrate formation from mixtures of methane and ethane. Chem Eng Sci 1987; 42: 2659–2666.

[15] Dholabhai P D, Kalogerakis N E, Bishnoi P R. Kinetics of methane hydrate formation in aqueous electrolyte solutions. Canadian Journal of Chemical Engineering 1993; 71: 68–74.

[16] Malegaonkar M B, Dholabhai P D, Bishnoi P R. Kinetics of carbon dioxide and methane hydrate formation, Canadian Journal of Chemical Engineering 1997; 75:1090–1099.

[17] Hashemi S, Macchi A, Servio P. Gas hydrate growth model in a semibatch stirred tank reactor. Ind Eng Chem Res 2007; 46: 5907-5912.

[18] Bergeron S, Servio P. Reaction rate constant of propane hydrate formation. Fluid Phase Equilibria 2008; 265: 30–36.

[19] Chapoy A, Mohammadi A H, Richon D, Tohidi B. Gas solubility measurement and modeling for methane–water and methane–ethane–n-butane–water systems at low temperature conditions. Fluid Phase Equilibria 20042;20;113–121

[20] McNaught A D, Wilkinson A. Compendium of chemical terminology, The Gold Book. 2nd ed. Blackwell Science. Malden. MA; 1997

[21] Makogon Y F. Gas hydrates: prevention of gas hydrate formation and their utilization. Moscow, Nedra; 1985, translated by Tolwinski A. CSM. Golden. CO; 1989.

[22] Handa Y P. Effect of hydrostatic pressure and salinity on the stability of gas hydrate. J Chem 1990; 94:2652-2657.

[23] Sun R, Duan Z. An accurate model to predict the thermodynamic stability of methane hydrate and methane solubility in marine environments. Chemical Geology 2007; 244: 248-262.

[24] Zhenhao D, Ding L, Yali C, Rui S. The influence of temperature, pressure, salinity and capillary force on the formation of methane hydrate. Geoscience Frontiers 2011; 2:125-135.

[25] Klauda Jeffery B, Sandler Stanley I. A fugacity model for gas hydrate phase equilibria. Ind Eng Chem Res 2000; 39:3377-3386.

[26] Duan Z, Moller N, Weare J H. An equation of state for CH_4-CO_2-H_2O I: pure systems from 0 to 1000 ℃ and from 0 to 8000 bar. Geochimica et Cosmochimica Acta 1992; 56:2605-2617.

[27] Piper L D, McCain W D, Correder J H. Compressibility factor for naturally occurring petroleum gases, gas reservoir engineering. In: 68th annual technical conference and exhibition of SPE. Houston; 1993.

[28] Batzle M, Wang Z. Seismic properties of pore fluids. Geophysics 1992; 57: 1396-1408.

[29] Østergaard K K, Tohidi B, Danesh A, Todd A C, Burgass R W. A general correlation for predicting the hydrate-free zone of reservoir fluids, SPE Production & Facilities 2000; 15:228-233.

[30] Gas hydrates in offshore production and drilling. Progress Report. Institute of Petroleum Engineering, Heriot-Watt University, Edinburgh; 1990-2002.

[31] Schlumberger log interpretation charts. Schlumberger Well Services. Houston. TX; 1986.

[32] Desai K P, Moore E J. Equivalent NaCl concentration from ionic concentration. The Log Analyst 1969.

[33] Østergaard K K, Tohidi B. A correlation for prediction the hydrate stability zone in the presence of ice. In: Fourth international conference on gas hydrates. Yokohama; 2003.

[34] Uddin M, Coombe D, Law D, Gunter B. Numerical studies of gas hydrate formation and decomposition in a geological reservoir. J Energy Resource Technology 2008; 130:032501-14.

[35] Collett T S, Boswell R, Lee M W, Anderson B J, Rose K, Lewis K A, Evaluation of long term gas hydrate production testing locations on the Alaska North Slope, In: Arctic Technology Conference. Houston; 2011.

[36] Moridis G J, Reagan M T, Boyle K, Zhang K, Evaluation of a deposit at the PBU L-106 site, North Slope, Alaska, for a potential long-term test of gas production from hydrates. In: SPE Western Regional Meeting. Anaheim, USA; 2010.

[37] Makogon Y F, Holditch S A, Makogon T Y. Russian field illustrates gas hydrate production. Oil and Gas Journal 2005;103: 43-47.

[38] Kurihara M, Sato A, Ouchi H, Narita H, Ebinuma T, Suzuki K, Masuda Y, Saeki T, Yamamoto K, Fujii T, Gas hydrate: prediction of production test performances in eastern Nankai-Trough methane hydrate reservoirs using 3D reservoir model. In: Offshore Technology Conference. Houston; 2010.

[39] Badakhshan Raz Sadegh, Ghassemi Ahmad, Stresses around a production well in gas hydrate-bearing formation. In: 45th US Rock Mechanics-Geomechanics Symposium. San Francisco; 2011.

[40] Alp D, Parlaktuna M, Moridis G J, Gas production by depressurization from hypothetical class 1G and class 1W hydrate reservoir, Energy Conversion Management 2007; 48:1864-1879.

[41] Shahbazi A, Pooladi-Darvish M. Ice formation during gas hydrate decomposition. In: Canadian International Petroleum Conference. Calgary; 2009.

[42] Shahbazi A, Pooladi-Darvish M. Modeling of ice formation in gas hydrate reservoir. In: Frontier +Innovation, CSPG CSEG CWLS Convention. Calgary; 2009.

[43] Shahbazi A. Mathematical modeling of gas production from gas hydrate reservoirs, PhD dissertation, University of Calgary, Canada, 2010.

[44] Angel C A, Shuppert J, Tucker J C. Anomalous properties of supercooled water, heat capacity, expansivity and proton magnetic resonance chemical shift from 0 to -38°C. The Journal of Physical Chemistry 1973; 77: 3092-3099.

[45] Speedy R J. Thermodynamic properties of supercooled water at 1 atm. Journal of Physical Chemistry 1987; 77: 3354-3358.

[46] Makogon Y F, and Ghassemi A. Effects of self-preservation of natural gas-hydrates. In: 44th US Rock Mechanics Symposium and 5th U.S.-Canada Rock Mechanics Symposium. Salt Lake City; 2010.

[47] Dickens G R, Quinby-Hunt M S, Methane hydrate stability in pore water: a simple theoretical approach for geophysical applications. Journal of Geophysical Research1997; 102:773-783.

[48] Freij-Ayoub R, Tan C, Clennell B, Tohidi B, Yang J. A wellbore stability model for hydrate bearing sediments. Journal of Petroleum Science and Engineering 2007;57:209–220.

[49] Rutqvist J, Moridis G. J. Numerical studies on the geomechanical stability of hydrate-bearing sediments. In: Offshore Technology Conference. Houston; 2007.

[50] Kimoto S, Oka F, Fushita T. A chemo–thermo–mechanically coupled analysis of ground deformation induced by gas hydrate dissociation. International Journal of Mechanical Sciences 2010; 52:365–376.

[51] Waite W F, Santamarina J C, Cortes D D, Dugan B, Espinoza D N, Germaine J, Jang J, Jung J W, Kneafsey T J, Shin H, Soga K, Winters W J, Yun T S. Physical properties of hydrate-bearing sediments. Reviews of Geophysics 2009; 47:1-38

[52] L.I. Rubinstein. The Stefan problem. American Mathematical Society. Providence. RI; 1971.

[53] Ji C, Ahmadi G, Smith D. Constant rate natural gas production from a well in a hydrate reservoir. Energy Conversion & Management 2003; 44:2403-2423.

[54] Ghassemi A, Tao Q, Diek A. Influence of coupled chemo-poro-thermoelastic processes on pore pressure and stress distributions around a wellbore in swelling shale. Journal of Petroleum Science and Engineering 2009; 67:57–64.

[55] Tao Q. Wellbore Stability in water sensitive shales. MS Thesis. University of North Dakota; 2006.

[56] Koh C, Sloan D, Sum A. Natural gas hydrates in flow assurance. Gulf Professional Publishing. Houston. TX; 2011.

[57] Sloan E D. Fundamental principles and applications of natural gas hydrates. Nature 2003; 426: 353-359.

[58] Barrer R M, Edge A V J. gas hydrate containing argon, krypton and xenon: kinetics and energies of formation and equilibria. Proc R Soc Lon A 1967; 300: 1-24.

[59] Makogon Y F, Cieslewicz W J. Hydrates of natural gases. PennWell Publishing Company. Tulsa. OK; 1981.

[60] Englezos P, A model for the formation kinetics of gas hydrates from methane, ethane and their mixtures. MS Thesis. University of Calgary. Canada;1986

[61] Bischoff K B, Froment G F. Chemical reactor design. Wiley Publication. New York. NY; 1979

[62] Englezos P, Kalogerakis N, Dholabhai P D, Bishnoi P R. Kinetic of formation from mixture of methane and ethane. Chemical Engineering Science 1987; 42:2659-2666.

[63] Sloan E D. Clatherate hydrates of natural gases, 2nd ed., Marcel Dekker. New York. NY;1998

[64] Wilder J W, Smith D H. Simple predictive relations, fugacities and enthalpies of dissociation for single guest clathrate hydrates in porous media. Chemical Engineering Science 2004; 59: 3945–3954.

[65] Chen L T, Sun C Y, Chen G J, Nei Y Q. Thermodynamics model of predicting gas hydrate in porous media based on reaction-adsorption, two-step formation mechanism. Ind Eng Chem Res 2010; 49: 3936-3943.

[66] Van der Waals J H. the statistical mechanics of clathrate compounds, Trans Faraday Soc 1955; 52:184-193.

[67] Palin D E, Powel H M. The structure of molecular compounds. part V. the clathrate compound of quinol and methanol. Journal of the Chemical Society 1948; 2:571-574.

[68] Barrer R M, Stuart W I. Non-stoicheiometric clathrate compounds of water. Proc R Soc Lond A 1957;243:172-189

[69] Van der Waals J H. The clathrate solutions. Advances in Chemical Physics 1959; 1-57.

[70] Holder G D, Corbin G, Papadopouos D. Thermodynamic and molecular properties of gas hydrates from mixture containing methane, argon and krypton. Ind Eng Chem Fund 1980;19:282-286.

[71] Handa Y.P. Effect of hydrostatic pressure and salinity on the stability of gas hydrate. J Chem 1990; 94: 2652-2657.

[72] Sun R, Duan Z. An accurate model to predict the thermodynamic stability of methane hydrate and methane solubility in marine environments. Chemical Geology 2007; 244: 248-262.

[73] Zhenhao D, Ding L, Yali C, Rui S. The influence of temperature, pressure, salinity and capillary force on the formation of methane hydrate. Geoscience Frontiers 2011; 2:125-135.

[74] Hashemi S, Macchi A, Bergeron S, Servio P. Prediction of methane and carbon dioxide solubility in water in the present of hydrate, Fluid Phase Equilibria 2006; 246:131-13.

[75] Pitzer K S, Kim Janice J. Thermodynamics of electrolytes. IV. activity and osmotic coefficients for mixed electrolytes. Journal of the American Chemical Society 1974; 96:5701-5707.

[76] Pitzer C. A thermodynamic model for aqueous solutions of liquid like density. Reviews in Mineralogy 1987; 17:97-142.

[77] Harvie E C, Møller M N, Weare J H. The prediction of mineral solubilities in natural waters: The Na-K-Mg-Ca-H-CI-SO_4-OH-HCO_3-CO_3-CO_2-H_2O system to high ionic strengths at 25°C. Geochimica et Cosmochimica Acta 1984; 48:723-751.

[78] Spencer R J, Møller N, Weare J H. The prediction of mineral solubilities in natural waters: a chemical equilibrium model for the Na-K-Ca-Mg-Cl-SO_4-H_2O system at temperatures below 25°C. Geochim Cosmochim Acta 1990; 54: 575–590.

[79] Christov C. Isopiestic investigation of the osmotic coefficients of $MgBr_2$(aq) and study of bromide salts solubility in the (m_1KBr + m_2MgBr_2)(aq) system at T=323.15 K. Thermodynamic model of solution behavior and (solid + liquid) equilibria in the $MgBr_2$(aq), and (m_1KBr + m_2MgBr_2)(aq) systems to high concentration and temperature. The Journal of Chemical Thermodynamics 2011; 43:344–353,

[80] Christov C. Isopiestic investigation of the osmotic coefficients of aqueous $CaBr_2$ and study of bromide salt solubility in the NaBr–$CaBr_2$–H_2O system at 50 °C: thermodynamic model of solution behavior and solid–liquid equilibria in the $CaBr_2$–H_2O, and NaBr–$CaBr_2$–H_2O systems to high concentration and temperature.

CALPHAD: Computer Coupling of Phase Diagrams and Thermochemistry 2011; 35:42–53.

[81] Marion G M, Kargel J S. Cold aqueous planetary geochemistry with FREZCHEM: from modeling to the search for life at the limits. Springer. Berlin; 2008

[82] Sun R, Duan Z. An accurate model to predict the thermodynamic stability of methane hydrate and methane solubility in marine environments. Chemical Geology 2007;244: 248–262

APPENDIX A

KINETICS OF GAS HYDRATES

Production of gas hydrates from a gas hydrate-bearing reservoir involves the following dissociation reaction.

$$G.(H_2O)_N \quad \rightarrow \quad G + N.H_2O \tag{A.1}$$

The knowledge of the rate on which the above dissociation reaction takes place is called kinetics. Considering the kinetics of gas hydrate dissociation is a crucial step in evaluation of gas production from a gas hydrate reservoir. In addition to parameters like drawdown pressure and reservoir temperature, the kinetics also dictate how fast the gas production could be.

The gas hydrate production sometimes involves secondary gas hydrate formation near the wellbore due to high production rate and the Joule-Thompson cooling effect [40]. The knowledge of gas hydrate formation kinetics is also important for the evaluation of gas hydrate plug formation in pipelines, surface facilities, and submerged gas pipelines [56, 3]. Gas hydrate transportation is another important concept for which the kinetics of gas hydrate formation plays a main role [1]. A historic background about the evolution of the study of gas hydrate kinetics is given in the following section.

A.1 Evolution of Gas Hydrate Kinetics Models

It is well known that the formation of gas hydrates is a crystallization-type process which involves nucleation and growth [57]. The nucleation is the process of

formation of nuclei with critical sizes which are thermodynamically stable for growth. In this phase, the atoms join the critical nuclei from surrounding liquid and cause growth of nuclei. The first published study related to the kinetics of gas hydrate formation and dissociation was the work of Barrer and Edge in 1967 [58]. They studied gas hydrate formation kinetics by purging inert gases of argon, krypton, and xenon into a chamber containing ice particles to form gas hydrates. Later in 1981, Makogon [59] gave a thermodynamic formulation for the calculation of critical nuclei size. The first attempt to address the formation kinetics of gas hydrate from a liquid solution was the work of Vysniauskas and Bishnoi (1983) [12]. They reported data on methane hydrate formation kinetics parameters by correlating a semi-empirical model with the rate of methane consumption per unit of surface area. The main drawbacks of the Vysniauskas model were the lack of a driving force term in their model, as well as the lack of a solid theoretical basis for their model. Englezos *et al.* [60] found the Vysniauskas and Bishnoi model inadequate to fully describe the formation kinetics, and proposed their pioneering kinetic model on the basis of the two- film theory [61].

In their theory, the gas hydrate growth is divided into two steps in series for the diffusion of gas through a liquid film layer around a gas hydrate particle, and then the chemical reaction for gas hydrate formation [13]. The driving force in their model was the difference between the gas fugacity in the gas phase in the cell and the equilibrium gas fugacity in the three-phase state. According to their model:

$$\frac{dn}{dt} = KA(f_g^v - f_{eq}) \tag{A.2}$$

where n is the moles of consumed gas, K is the global rate constant, A is the reaction surface area, and f_g^v and f_{eq} are the fugacity of the gas. K is a global rate constant that can be written as:

$$\frac{1}{K} = \frac{1}{k_m} + \frac{1}{k_r} \tag{A.3}$$

where k_m is the mass transfer coefficient and k_r is the intrinsic reaction rate constant. Englezos *et al.* [13] used a semi-batch high pressure cell equipped with a magnetic stirrer to calculate the moles of gas consumed during the gas hydrate formation period. Utilizing agitation in their system, they increased the mass transfer constant to a level where:

$$k_m \gg k_r \tag{A.4}$$

Therefore:

$$\frac{1}{K} = \frac{1}{k_r} \tag{A.5}$$

As shown in Eq. (A.5), by suppressing the mass transfer rate with severe agitation, the global rate calculated from experimental results is approximately equal to the reaction kinetic constant. This is the method used by Englezos *et al.* [13] to calculate this constant. They then fitted their kinetics model to the experimental data to find the

approaches an asymptote, whereby an increase in rpm does not have any additional effect on k_r. They concluded that the high turbulence in the cell that occurs over high cell stirring speeds causes the elimination of the mass transfer effect and renders the chemical reaction kinetics as the controlling step of gas hydrate growth. Therefore, their achieved parameter, K, is essentially the rate reaction constant [13].

Subsequently, Enzlezos *et al.* extended their theory to consider the mixture of methane and ethane gases [62]. Dholabhai *et al.* (1993) used the Enzlezos *et al.* model to describe the kinetics of methane hydrate formation from aqueous NaCl, KCl, and NaCl-KCl solutions [15]. A modification to the Englezos theory was made by Malegaonkar (1997) for considering the relative high solubility of CO_2 gas in aqueous solutions [16]. Hashemi *et al.* (2007) modified the Englezos model [17] with consideration for the concentration instead of the fugacity as a driving force. They reasoned that the concentration difference is usually considered as a mass transfer driving force. They stated that the fugacity difference, which is based on pressure and temperature, should not be considered as a driving force since the pressure gradient would cause a force imbalance between different phases in the system [63]. This being impossible, they proposed the following kinetic equation for gas hydrate formation [17].

$$\frac{dn}{dt} = KA(C - C_{eq}) \tag{A.6}$$

where C is the gas concentration in the liquid phase in mole/m^3 and C_{eq} is the concentration of gas in the equilibrium state. Like the Englezos model, in the Hashemi *et*

where C is the gas concentration in the liquid phase in mole/m^3 and C_{eq} is the concentration of gas in the equilibrium state. Like the Englezos model, in the Hashemi *et al.* model, the global reaction rate, K, is defined based on mass transfer and the intrinsic kinetic coefficients. Consequently, in high agitation conditions for which the mass transfer effect is negligible, the calculated global kinetic parameter, K, will be equal to the intrinsic reaction rate kinetic constant. Hashemi *et al.* also considered the heat transfer in the cell due to the exothermic nature of gas hydrate formation [17]. Bergeron *et al.* (2008) slightly modified the Hashemi *et al.* work by considering the gas mole fraction in the liquid phase instead of the gas molar concentration [18, 19]. Bergeron's model offers a simple yet complete model to describe the kinetics of gas hydrate formation in its growth phase. In this study, this model is used as a base model for gas hydrate formation kinetics. The model is elaborated and reformulated in the following section.

A.2. The Growth Model Used in the Current Research

Considering the evolutionary path of the kinetic models of gas hydrate growth, the Bergeron *et al.* model has been chosen as a base kinetic model for the current study because of its simplicity and overall completeness. The model then was slightly reformulated to find a final form for a relationship between the moles of consumed gas as a function of time. According to the Bergeron model:

$$\frac{dn}{dt} = \frac{V_L \rho_w}{MW_w} \frac{(x^l - x^{H-l})}{\frac{1}{\pi \mu_2(t) k_r}} \tag{A.7}$$

where n is the moles of consumed gas, t is time in seconds, V_L is the volume of water in the cell in cm^3, ρ_w is the density of water in gr/cm^3, MW_w is the molecular weight of water in gr/mole, x^l is the mole fraction of dissolved gas in experimental pressure and temperature, and x^{H-l} is the equilibrium solubility of gas under hydrate-liquid-gas equilibrium conditions at experimental pressure and temperature. x^l is the parameter that should be measured at a hydrate formation experimental condition and x^{H-l} is the equilibrium gas solubility that needs to be calculated by a thermodynamic model.

The method of calculation of x^{H-l} is discussed in Appendix B. Also, k_r is the reaction rate constant in m/sec and $\mu_2(t)$ is the second moment of particle size distribution in 1/m. The goal of this research is the calculation of the reaction rate constant, k_r. $\mu_2(t)$, which can be defined according to the following relationship.

$$\mu_2(t) = \mu_0^0 G^2 t^2 + 2\mu_1^0 G t + \mu_2^0 \tag{A.8}$$

where μ_0^0 is the initial zeroth moment of particle size distribution which is equal to the initial number of gas hydrate particles in the liquid phase and is defined as:

$$\mu_0^0 = \frac{6MW_H(n_{tb} - n_l)}{\eta \pi V_L \rho_H r_c^3} \tag{A.9}$$

where n_{tb} is the moles of gas dissolved at turbidity point and n_l is the moles of dissolved gas at the liquid immediately before the moment of gas hydrate formation. We have [18, 19],

$$n_{tb} - n_l = \frac{m_w Cp_w \Delta T}{\Delta H} \tag{A.10}$$

where m_w is the mass of liquid in the cell in kg, Cp_w is the heat capacity of liquid in J/kg.K, ΔT is the jump in the temperature at the moment of gas hydrate formation and ΔH is the gas hydrate formation enthalpy in J/mole which is defined by the following correlation [64].

$$\Delta H = -R[b + cT + \frac{d\left(1+\frac{T_0}{T}\right)\left(c+\frac{b}{T}\right)+d}{\left(1+\frac{T_0}{T}\right)^2} \times Exp\left(a+\frac{b}{T}+cLn\left(\frac{T_0}{T}\right)\right)] \quad \text{(A.11)}$$

where T_0=273.15 K, a=-3.679, b=1242.7, c=-27.903, and d=8.694. Plugging Eq. (A.10) to (A.9), we will get:

$$\mu_0^0 = \frac{6MW_H}{\eta\pi V_L \rho_H r_c^3}\frac{m_w Cp_w \Delta T}{\Delta H} \quad \text{(A.12)}$$

The parameters μ_1^0 and μ_2^0 could be defined according to the following equations:

$$\mu_1^0 = r_c \mu_0^0 \quad \text{(A.13)}$$

$$\mu_2^0 = r_c^2 \mu_0^0 \quad \text{(A.14)}$$

r_c is the critical diameter of gas hydrate nuclei, in m, at the onset of hydrate formation and is defined as:

$$r_c = \frac{-4\sigma}{\Delta g} \quad \text{(A.15)}$$

σ is the surface tension of water and gas hydrate in J/m^2 which is given by the following correlation[65]

$$\sigma = a + bT \quad \text{(A.16)}$$

where a=0.09946 J/m^2 and b=-0.23×10^{-3} J/m^{2}K and T is temperature in K. Also, Δg is in Gibbs free change per unit volume during hydrate formation process in J/m^3 and is given by the following formula.

$$\Delta g = \frac{RT}{v_H}\left[Ln\left(\frac{x^{H-L}}{x^{tb}}\right) + \eta_w Ln\left(\frac{1-x^{H-L}}{1-x^{tb}}\right)\right] \quad \text{(A.17)}$$

R is the universal gas constant equal to 8.31446 J/ K.mole, T is the experimental temperature in K, η_w is the moles of water per mole of gas hydrate, v_H is the molar volume of gas hydrate in m^3/mole, and x^{tb} is the mole fraction of gas in the solution immediately before hydrate formation onset. With the measurement of x^l, the molar fraction of dissolved after gas hydrate formation, one can calculate x^{tb} using Eq. (A.10). The last remaining parameter for the calculation of the second moment of particle distribution,$\mu_2(t)$, is G or the linear growth rate of gas hydrate particles in m/s and is defined by:

$$G = \frac{d(2r)}{dt} = 2\frac{\rho_w}{MW_w}\frac{MW_H}{\rho_H \eta}(x^l - x^{H-l})k_r \quad \text{(A.18)}$$

We introduce the dimensionless parameter of a, with the following definition:

$$a = 2\frac{\rho_w}{MW_w}\frac{MW_H}{\rho_H \eta}(x^l - x^{H-l}) \quad \text{(A.19)}$$

Substituting the Eq. (A.19) in Eq. (A.18), we will get:

$$G = ak_r \quad \text{(A.20)}$$

Substituting the Eq. (A.19), (A.18) and (A.20) in Eq. (A.8), we will get:

$$\mu_2(t) = \mu_0^0[(ak_r)^2 t^2 + 2r_c(ak_r)t + r_c^2] \quad \text{(A.21)}$$

Also, by substituting the Eq. (A.12) into (A.21), we have:

$$\mu_2(t) = \frac{6MW_w}{\eta\pi V_L \rho_H} \frac{m_w Cp_w \Delta T}{\Delta H} [\frac{(ak_r)^2}{r_c^3} t^2 + 2\frac{(ak_r)}{r_c^2} t + \frac{1}{r_c}] \quad (A.22)$$

Now, we substitute the Eq. (A.22) into the Eq. (A.7) and rearrange it to get:

$$\frac{dn}{dt} = 2\frac{\rho_w}{MW_w} \frac{MW_H}{\eta\rho_H} (x^l - x^{H-l}) \frac{3m_w Cp_w \Delta T}{\Delta H} [\frac{(ak_r)^2}{r_c^3} t^2 + 2\frac{(ak_r)}{r_c^2} t + \frac{1}{r_c}] k_r \quad (A.23)$$

or

$$\frac{dn}{dt} = \frac{3m_w Cp_w \Delta T (ak_r)}{\Delta H} [\frac{(ak_r)^2}{r_c^3} t^2 + 2\frac{(ak_r)}{r_c^2} t + \frac{1}{r_c}] \quad (A.24)$$

The final form of the kinetic equation is:

$$\frac{dn}{dt} = \frac{3m_w Cp_w \Delta T}{\Delta H} [(\frac{ak_r}{r_c})^3 t^2 + 2(\frac{ak_r}{r_c})^2 t + \frac{ak_r}{r_c}] \quad (A.25)$$

For having the moles of consumed gas, n, as a function of time, the Eq. (A.25) needs to be integrated.

$$\int_{n_0}^{n} dn = \int_0^t \frac{3m_w Cp_w \Delta T}{\Delta H} [(\frac{ak_r}{r_c})^3 t^2 + 2(\frac{ak_r}{r_c})^2 t + \frac{ak_r}{r_c}] dt \quad (A.26)$$

or

$$\mathrm{n(t)} = \frac{3m_w Cp_w \Delta T}{\Delta H} [\frac{1}{3}\left(\frac{ak_r}{r_c}\right)^3 t^3 + \left(\frac{ak_r}{r_c}\right)^2 t^2 + (\frac{ak_r}{r_c}) t] \quad (A.27)$$

The Eq. (A.27) is the final kinetic function that should be used to fit on the experimental data presented in chapter two. The goal of this curve fitting is finding the kinetics reaction constant. The parameter x^l should be measured experimentally and the parameter x^{H-l} is the equilibrium gas solubility in solution in the presence of the gas hydrate. The method for calculation of x^{H-l} is discussed in Appendix B.

APPENDIX B

THERMODYNAMICS OF GAS HYDRATES

For the first time, Van der Waals [66], 1955, derived a statistical-mechanical formulation to describe the thermodynamic equilibrium condition of *clatherate* compound formation between hydroquinol (benzene-1, 4-diol) and gases like H_2S which were structurally studied by Palin and Powel, 1948 [67]. Barrer and Stuart, 1957, extended Van der Waals' model for describing gas hydrate thermodynamics [68]. Latter, Van der Waals and Platteeuw, 1959, perfected their model in their classical review paper [69]. Holder *et al.,* 1980, [70], represent the thermodynamic formulation of gas hydrate in the formal way that is known today. Finally, Handa, 1990, [71], employed water activity instead of water mole fraction to the chemical potential of water in solution more accurately. This final formulation has been used as a standard thermodynamic method by many researchers for the calculation of equilibrium gas hydrate formation temperature and pressure, as well as equilibrium gas solubility in the solution in the presence of gas hydrate.

B.1. Basic Theory

In the equilibrium state, the chemical potential of all species are the same in all of the present phases. For either of gas-gas hydrate–liquid equilibrium or three-phase or gas hydrate –liquid two-phase equilibrium in the system, we could write [71]

$$\mu_w^H = \mu_w^L \tag{B.1}$$

where μ_w^H is the chemical potential of water in hydrate phase and μ_w^L is the chemical potential of water in liquid phase. Subtracting two sides of equation from μ_w^β which is the chemical potential of water in the hypothetical unoccupied hydrate phase, we will get

$$\mu_w^\beta - \mu_w^H = \mu_w^\beta - \mu_w^L \tag{B.2}$$

or

$$\Delta\mu_w^H = \Delta\mu_w^L \tag{B.3}$$

According to the statistical thermodynamic theory of Van der Waals and Platteeuw, 1959, [69], $\Delta\mu_w^H$ is:

$$\Delta\mu_w^H = -RT\sum_{i=1}^{n} \nu_i \times Ln(1-\theta_i) \tag{B.4}$$

where R is the universal gas constant which is equal to 8.31446 J/ K.mol, T is the absolute temperature in K and n is the number of different type of cages in the gas hydrate lattice. For example, for type I gas hydrate structure, there are two types of small 5^{12} and large $5^{12}6^2$ cavities and, therefore, n=2. ν_i is the number of type i cages in the gas hydrate lattice . For type I gas hydrate, ν_i is $\frac{1}{23}$ and $\frac{3}{23}$ [1] for small and large cavities respectively. θ_i is the fraction of occupied cages in each type. θ_i can be calculated by Langmuir's adsorption relationship.

$$\theta_i = \frac{C_i \times f_i}{1 + \sum_{i=1}^{n} C_i \times f_i} \tag{B.5}$$

C_i is the Langmuir's constant of guest molecule I in 1/bar. The following correlation [72] is used for calculation of the Langmuir constant.

$$C_i = 10^5 Exp(A + \frac{B}{T}) \quad \text{(B.6)}$$

where A and B are constants and for methane hydrate they are given in Table 6. Also, f_i is the fugacity of the gas molecule i gas hydrate phase in bar. In equilibrium, the fugacity of gas in all phases is equal and therefore, the fugacity of gas in the gas hydrate lattice is equal to the fugacity of the gas molecule in the gas phase. In the case of methane hydrate, the vapor pressure of water in the gas phase is very low and, therefore, it can be assumed that the fugacity of methane in the gas phase is equal to the fugacity of pure methane at the same pressure and temperature conditions [25, 73].

Table 6 The constants of equation (B.6) for the calculation of the Langmuir's constant [72]

Parameter	Small cage	Large Cage
A	-24.027993	-22.683049
B	3134.7529	3080.3857

The fugacity of pure methane is calculated by Duan's equation of state, Duan *et al.*, 1992 [26]. For the calculation of the fugacity, first the methane gas compressibility factor, z, is calculated by the Batzle and Wang correlation [28]. Then the molar volume of methane could be calculated according to the following relationship:

$$V = \frac{83.14472zT}{P} \quad \text{(B.7)}$$

where P is pressure in bar, T is temperature in K, and V is molar volume in m^3/mole. This molar volume is used in Duan's equation of state [26] to calculate gas fugacity. The difference between the chemical potential of water in the empty gas hydrate lattice and in the liquid phase, $\Delta\mu_w^L$, can be defined as [70, 71]

$$\frac{\Delta\mu_w^L}{R\,T} = \frac{\Delta\mu_w^0(T_0)}{R\,T_0} - \int_{T_0}^{T} \frac{\Delta h_w^{\beta-L}}{R\,T^2}\,dT + \int_0^P \frac{\Delta V_w^{\beta-L}}{R\,T}\,dT - Ln(a_w) \tag{B.8}$$

where R is the universal gas constant equal to 8.31446 J/K.mol, T is the absolute temperature in K, $\Delta\mu_w^0(T_0)$ is the difference between the chemical potential of water in the empty gas hydrate lattice and in the liquid phase at the reference pressure and temperature of T_0=273.15 K and P_0= 0 Pa. Also, $\Delta h_w^{\beta-L}$ and $\Delta V_w^{\beta-L}$ are the difference between the molar enthalpy and the molar volume of water in the empty gas hydrate cell and the liquid phase, respectively. $\Delta h_w^{\beta-L}$ can be defined by the following relationship [70]:

$$\Delta h_w^{\beta-L} = \Delta h_w^0 + \int_{T_0}^{T} \Delta C_P\,dT \tag{B.9}$$

ΔC_P is the difference between the water molar heat capacity in the empty gas hydrate cell and in the liquid phase. ΔC_P can be defined as:

$$\Delta C_P = \Delta C_P^0 + b(T - T_0) \tag{B.10}$$

The constants in formulas (B.9) and (B.10) are given in Table 7:

Table 7 The parameters of Eq. (B.9) and (B.10) [74]

Parameter	Value	Reference
$\Delta\mu_w^0(T_0)$, J/mole	1256	74
Δh_w^0, J/mole	-4822	74
ΔC_P^0, J/kg.K.mole	-38.18	70
B	0.141	70

Finally, a_w is the activity of water in the solution. Calculation of water activity is discussed in the following section.

B.2. Calculation of Water Activity

For pure water-pure methane gas system, the solubility of methane in the water is low. Therefore, the activity of water could be considered equal to the water mole fraction or

$$a_w = X_w = 1 - X_g \quad \text{(B.11)}$$

X_g is the mole fraction of dissolved methane in water. For the brine-methane system, the water activity is [75]:

$$Ln(a_w) = -\frac{M_w \emptyset}{1000} \sum_{i=1}^{n} m_i \quad \text{(B.12)}$$

M_w is water molecular weight, m_i is the molality of solute including anions, cations and natural molecules of gases in the solution and $\emptyset$ is the osmotic coefficient. The following

formula, which was proposed by Pitzer [75, 76] and later rearranged by Harvie *et al.* [77], is used for the calculation of osmotic coefficient.

$$(1-\emptyset)\sum_{i=1}^{n} m_i = -\frac{2\,A_\emptyset I^{1.5}}{1+1.2I^{0.5}} + \sum_{c=1}^{n_C}\sum_{a=1}^{n_a} m_c\,m_a\left(B_{ca}^{\emptyset} + ZC_{ca}\right)$$

$$+\sum_{c=1}^{n_C}\sum_{c'=1\&c'\neq c}^{n_{c'}} m_c\,m_{c'}\left(\Phi_{cc'}^{\emptyset} + \sum_{a=1}^{n_a} m_a\ \phi_{acc'}\right)$$

$$+\sum_{a=1}^{n_a}\sum_{a'=1\&a'\neq a}^{n_{a'}} m_a\,m_{a'}\left(\Phi_{aa'}^{\emptyset} + \sum_{c=1}^{n_c} m_c\ \phi_{caa'}\right)$$

$$+\sum_{c=1}^{n_C}\sum_{n=1}^{n_n} m_c\,m_n\lambda_{nc} + \sum_{a=1}^{n_a}\sum_{n=1}^{n_n} m_a\,m_n\lambda_{na}$$

$$+\sum_{a=1}^{n_a}\sum_{c=1}^{n_c}\sum_{n=1}^{n_n} m_a\,m_c\,m_n\zeta_{acn} \qquad \text{(B. 13)}$$

where m is the molality of solutes and subscripts, a, c and n indicate anions, cations and natural solutes. I is the ionic strength which is defined by the following formula.

$$I = \sum_{i=1}^{n} m_i\,z_i^2 \qquad \text{(B. 14)}$$

z_i, is the charge of ions. Also Z is:

$$Z = \sum_{i=1}^{n} m_i|z_i| \qquad \text{(B. 15)}$$

$A_\emptyset$ is the Debye–Hückel constant, which is the function of temperature, T, and is given in the following formula. [78]

$$A_{\emptyset} = 86.684 + 0.085\mathrm{T} - 0.0001\mathrm{T}^2 + 4.88 \times 10^{-8}\mathrm{T}^3 - \frac{1327.32}{\mathrm{T}} - 17.65\ln(\mathrm{T}) \quad \text{(B.16)}$$

where T is temperature in K. $B_{ca}^{\emptyset}$ is the second virial coefficient for the interaction between ions with dissimilar charges and is defined as [75, 76]:

$$B_{ca}^{\emptyset} = B_{ca}^{0} + B_{ca}^{1} e^{-\alpha_{ca}\sqrt{I}} + B_{ca}^{2} e^{-12\sqrt{I}} \quad \text{(B.17)}$$

α_{ca} is constant, where $\alpha_{ca} = 2$ when both anion and cation are monovalent and $\alpha_{ca} = 1.4$ for ions with higher valances. B_{ca}^{0} and B_{ca}^{1} are functions of temperature and $B_{ca}^{2} = 0$.

C_{ca} is the third virial coefficient for the interaction between ions with dissimilar charges and is defined as

$$C_{ca} = \frac{C_{ca}^{\emptyset}}{2\sqrt{|z_a z_c|}} \quad \text{(B.18)}$$

Parameters B_{ca}^{0} , B_{ca}^{1} and $C_{ca}^{\emptyset}$ are functions of temperature that have the following general form:

$$f(T) = a_1 + a_2 T + a_3 T^2 + a_4 T^3 + \frac{a_5}{T} + a_6\, ln(T) \quad \text{(B.18)}$$

The constants a_1 to a_6 for different compounds are given in Table 9.

Table 8 The constants in the of Eq. (B.17), (B.18) and (B.19)

Pitzer's parameter	Equation parameter						Ref.
	a_1	a_2	a_3	a_4	a_5	a_6	
$B^{(0)}_{Na,Cl}$	7.87239712	-8.386×10^{-3}	1.4414×10^{-5}	-8.78×10^{-9}	−496.920671	−0.821	78
$B^{(1)}_{Na,Cl}$	866.915291	0.606166931	-4.805×10^{-4}	1.8850×10^{-7}	−17046.0145	−167.171	78
$C^{\emptyset}_{Na,Cl}$	1.70761824	2.3297×10^{-3}	-2.4667×10^{-6}	1.215×10^{-9}	−1.35583596	−0.388	78
$B^{(0)}_{K,Cl}$	26.5718766	9.9272×10^{-3}	-3.623233×10^{-6}	-6.2843×10^{-11}	-755.70722	-4.673	78
$B^{(1)}_{K,Cl}$	1697.42977	1.22270943	-9.99×10^{-4}	4.0473×10^{-7}	-32868.4422	-328.814	78
$C^{\emptyset}_{K,Cl}$	-3.2757168	-1.27×10^{-3}	4.7137×10^{-7}	1.1162×10^{-11}	90.7747666	0.5805	78
$B^{(0)}_{Ca,Cl}$	-56.2764702	-3.00772×10^{-2}	1.056304×10^{-5}	3.3332×10^{-9}	1117.30349	10.66	78
$B^{(1)}_{Ca,Cl}$	3.4787	-1.5417×10^{-2}	3.1791×10^{-5}	0	0	0	78
$C^{\emptyset}_{Ca,Cl}$	26.4231655	2.46923×10^{-2}	-2.483×10^{-5}	1.224×10^{-8}	-418.098427	-5.3535	78
$B^{(0)}_{Mg,Cl}$	313.852913	0.261769099	-2.46267×10^{-4}	1.15765×10^{-7}	-5531.33381	-62.1617	78
$B^{(1)}_{Mg,Cl}$	-31843.2525	-28.6710358	2.78893×10^{-2}	-1.32798×10^{-5}	524032.958	6407.704	78
$C^{\emptyset}_{Mg,Cl}$	5.9532×10^{-4}	-2.49949×10^{-4}	2.41831×10^{-7}	0	0	0	78
$B^{(0)}_{K,Br}$	0.4798961	-4.17397×10^{-4}	0	0	-90.5196847	0	79
$B^{(1)}_{K,Br}$	-4.13092017	6.8531×10^{-3}	0	0	704.957954	0	79
$C^{\emptyset}_{K,Br}$	-5.932267×10^{-2}	6.33899×10^{-5}	0	0	11.7934031	0	79
$B^{(0)}_{Na,Br}$	0.711600256	-7.5199×10^{-4}	0	0	−109.266366	0	80
$B^{(1)}_{Na,Br}$	-4.97335195	8.5779×10^{-3}	0	0	738.610135	0	80
$C^{\emptyset}_{Na,Br}$	-7.34173×10^{-2}	8.7145×10^{-5}	0	0	13.3019597	0	80
$B^{(0)}_{Na,HCO_3}$	−37.2624193	-1.4459×10^{-2}	0	0	682.885977	6.8995857	81
$B^{(1)}_{Na,HCO_3}$	−61.4635193	-2.4467×10^{-2}	0	0	1129.389146	11.41086	81
$C^{\emptyset}_{Na,HCO_3}$	0	0	0	0	0	0	81
$B^{(0)}_{Na,SO_4}$	-3324.8633	-2.9297353	2.8024367×10^{-3}	-1.3169×10^{-6}	55395.8527	666.6604	78
$B^{(1)}_{Na,SO_4}$	-3574.0616	-3.00l1206	2.7366095×10^{-3}	-1.2192×10^{-6}	60971.6482	711.61312	78
$C^{\emptyset}_{Na,SO_4}$	368.520478	0.316243995	-2.9537×10^{-4}	1.35491×10^{-7}	-6226.07913	-73.584	78

Table 9 The constants of Eq. (B.13) for secondary cation-cation and ternary cation-cation-anion interaction parameters

Pitzer's parameter	Equation parameter						Ref.
	a_1	a_2	a_3	a_4	a_5	a_6	
$\theta_{Na,K}$	−18.2267	-3.6904×10^{-3}	0	0	612.415	3.02995	81
$\psi_{Na,K,Cl}$	6.48108127	1.46803×10^{-3}	0	0	−204.354	−1.0945	81
ψ_{Na,K,SO_4}	-5.63×10^{-2}	1.4146×10^{-3}	2.3×10^{-8}	-2.1088×10^{-8}	−256.61	0.18538	81
ψ_{Na,K,HNO_3}	−0.0079	0	0	0	0	0	81
$\theta_{Na,Mg}$	0.070	0	0	0	0	0	81
$\psi_{Na,Mg,Cl}$	-3.109×10^{-2}	5.4465×10^{-5}	0	0	1.994	0	81
ψ_{Na,Mg,SO_4}	−0.1207	5.235×10^{-4}	-5.39×10^{-7}	-4.39×10^{-10}	−17.23	1.265×10^{-2}	81
$\theta_{Na,Ca}$	0.03	-1.9×10^{-5}	0	9.5×10^{-10}	-2.5	0.0013	81
$\psi_{Na,Ca,Cl}$	−7.6398	-1.299×10^{-2}	1.106×10^{-5}	0	0	1.8475	81
ψ_{Na,Ca,SO_4}	−0.0808	4.6565×10^{-3}	5.546×10^{-6}	-1.4107×10^{-7}	−1091.5	0.96985	81
$\theta_{K,Mg}$	0.1167	0	0	0	0	0	81
$\psi_{K,Mg,Cl}$	5.036×10^{-2}	-8.751×10^{-6}	0	0	−28.99	0	81
ψ_{K,Mg,SO_4}	−0.118	-4.78×10^{-5}	-3.27×10^{-7}	-9.37×10^{-10}	33.44	-8.84×10^{-3}	81
$\theta_{K,Ca}$	2.36571	−0.00454	0	0	−284.94	0	81
$\psi_{K,Ca,Cl}$	−0.0593	2.5428×10^{-4}	0	0	−13.439	0	81
$\theta_{Mg,Ca}$	5.31274136	-6.3424×10^{-3}	0	0	−983.114	0	81
$\psi_{Mg,Ca,Cl}$	41.579022	1.3038×10^{-2}	0	0	−981.66	−7.4062	81
ψ_{Mg,Ca,SO_4}	0.024	0	0	0	0	0	81

$\Phi^{\emptyset}_{aa'}$ and $\Phi^{\emptyset}_{cc'}$ are the second virial coefficients for the interaction between similar ions and are defined as [76, 77]

$$\Phi_{ij}^{\emptyset} = \theta_{ij} + {}^{E}\theta_{ij}(I) + {}^{E}\theta'_{ij}(I) \times I \quad \text{(B.20)}$$

Parameters ${}^{E}\theta_{ij}(I)$ and ${}^{E}\theta'_{ij}(I)$ account for electrostatic unsymmetrical mixing effects which depend on ionic strength as well as electrolyte pair type. These parameters usually are considered to be zero by different researchers [78, 81]. Therefore,

$$\Phi_{ij}^{\emptyset} = \theta_{ij} \quad \text{(B.21)}$$

θ_{ij} is the function of temperature with the general form given in formula (B.19). $\phi_{caa'}$ and $\phi_{acc'}$ are the ternary ion interaction parameters between a pair of similar ions and an ion with dissimilar charge.

Table 10 The constants of Eq. (B.13) for the secondary anion-anion and ternary anion-anion-cation interaction parameters.

Pitzer's parameter	Equation parameter						Ref.
	a_1	a_2	a_3	a_4	a_5	a_6	
θ_{Cl,SO_4}	0.07	0	0	0	0	0	81
$\psi_{Cl,SO_4,Na}$	0.0255	-6.12×10^{-5}	-9×10^{-9}	3.04×10^{-10}	-0.89	-2.28×10^{-3}	81
$\psi_{Cl,SO_4,K}$	0.0608	-1.82×10^{-4}	-2.15×10^{-8}	-3.28×10^{-10}	5.22	-3.01×10^{-3}	81
$\psi_{Cl,SO_4,Mg}$	0.059	-8.97×10^{-5}	4.7×10^{-8}	6.5×10^{-11}	-24.13	4.345×10^{-3}	81
$\psi_{Cl,SO_4,Ca}$	−0.026	-9.46×10^{-5}	-3.13×10^{-7}	-1.28×10^{-9}	29.44	-6.49×10^{-3}	81
θ_{Cl,HNO_3}	0.03	0	0	0	0	0	81
$\psi_{Cl,HNO_3,Na}$	-0.004	-3.25×10^{-5}	-6.6×10^{-8}	-2.74×10^{-10}	5.83	-9.85×10^{-4}	81
$\psi_{Cl,HNO_3,Mg}$	-0.096	0	0	0	0	0	81

Likeθ_{ij}, ternary interaction parameters are the function of temperature and have a general form of Eq. (B.19). The constants a_1 to a_6 for these parameters are given in Tables 8 and 9. Also, the constants of Eq. (B.19) for anion-anion and anion-anion-cation interaction parameters are given in the Tables 10 and 11. All the data are taken from the book published by Marion [81]. Finally, the λ_{nc}, λ_{na} and ζ_{acn} are the secondary gas-cation and gas-anion and the ternary gas-anion-cation parameters.

Table 11 The constants of Eq. (B.13) for the secondary and the ternary ion-gas interaction parameters.

Pitzer's parameter	Equation parameter						Ref.
	a_1	a_2	a_3	a_4	a_5	a_6	
$\lambda_{CH_4,Na}$	0.0992	2.5791×10^{-5}	0	0	0	0	20
$\lambda_{CH_4,K}$	0.13909	0	0	0	0	0	20
$\lambda_{CH_4,Mg}$	0.24678	0	0	0	0	0	20
$\lambda_{CH_4,Ca}$	−5.64279	8.51393	0	0	1000.578	0	20
$\lambda_{CH_4,Cl}$	0	0	0	0	0	0	20
λ_{CH_4,SO_4}	0.03041	0	0	0	0	0	20
λ_{CH_4,HNO_3}	0.00669	0	0	0	0	0	20
$\xi_{CH_4,Na,Cl}$	−0.00624	0	0	0	0	0	20
$\xi_{CH_4,K,Cl}$	−0.00382	0	0	0	0	0	20
$\xi_{CH_4,Mg,Cl}$	−0.01323	0	0	0	0	0	20
$\xi_{CH_4,Ca,Cl}$	−0.00468	0	0	0	0	0	20

These gas-ion interaction coefficients are functions of temperature and have a general form of Eq. (B.13). The constants a_1 to a_6 for these parameters are given in Table 11.

B.3. Calculation of Gas Solubility in the Solution

The equilibrium methane solubility in two or three phase equilibrium can be calculated using Eq. (B.4) and (B.8). The flow chart for the calculation of methane solubility under methane hydrate formation conditions is shown in Fig. 40. First, the value of methane mole fraction or molality in solution should be guessed and then we calculate $\Delta\mu_w^L$ and $\Delta\mu_w^H$ using Eq. (B.4) and (B.8). Then, we calculate the difference between $\Delta\mu_w^L$ and $\Delta\mu_w^H$ and if it is less than a limit, for example 0.01 [82], the guessed value of methane molality or mole fraction is the answer. If the above condition is not satisfied, we change our guess and repeat the above steps again until the condition for the exit of the loop is satisfied.

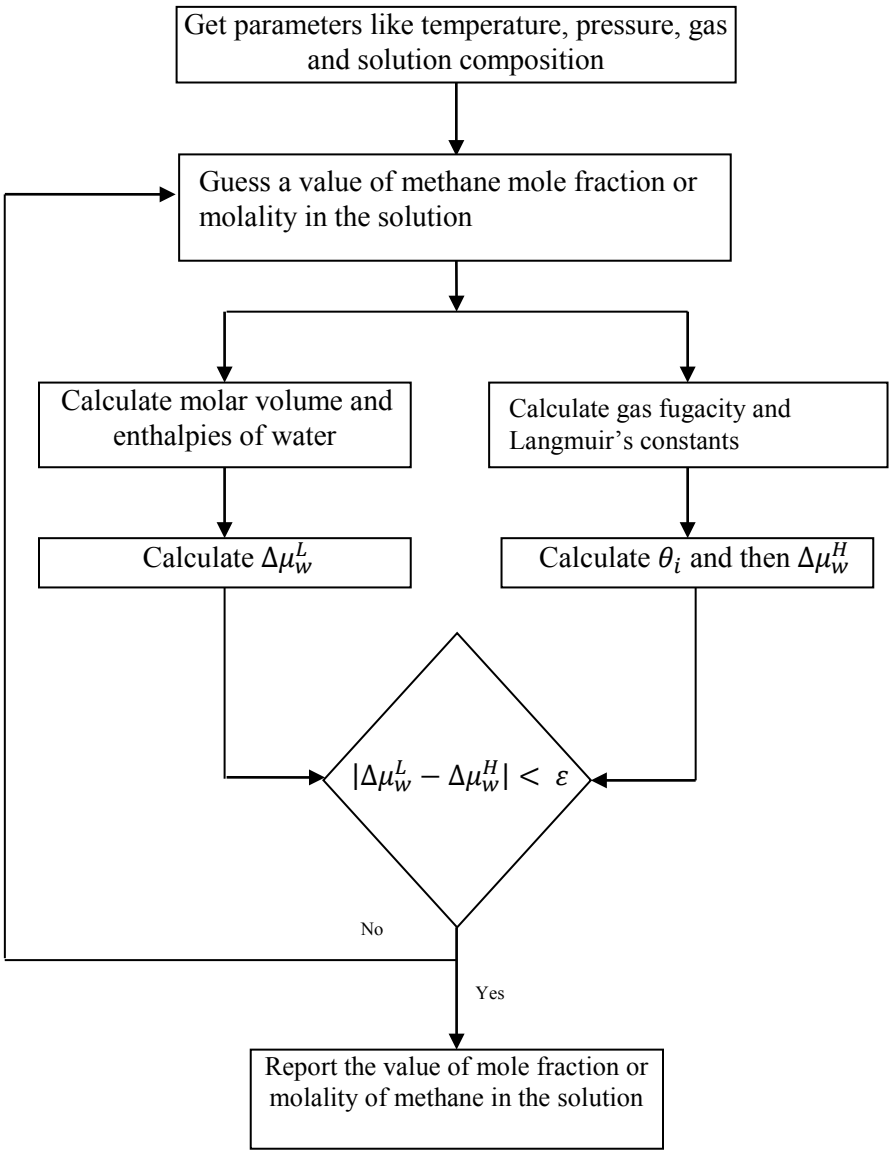

Fig.41 Flow chart for the calculation of equilibrium gas solubility in liquid in the presence of gas hydrates.

VITA

Name: Sadegh Badakhshan Raz

Address: Department of Petroleum Engineering, 3116 TAMU- 507 Richardson Building, College Station, TX 77843

Email Address: sbadakhshan@yahoo.com

Education:

- B.S., Materials Engineering, Sahand University of Technology, Tabriz, Iran, 1999
- M.S., Materials Engineering, Sharif University of Technology, Tehran, Iran, 2002
- M.S., Petroleum Engineering, Texas A&M University, College Station, TX, USA, 2012